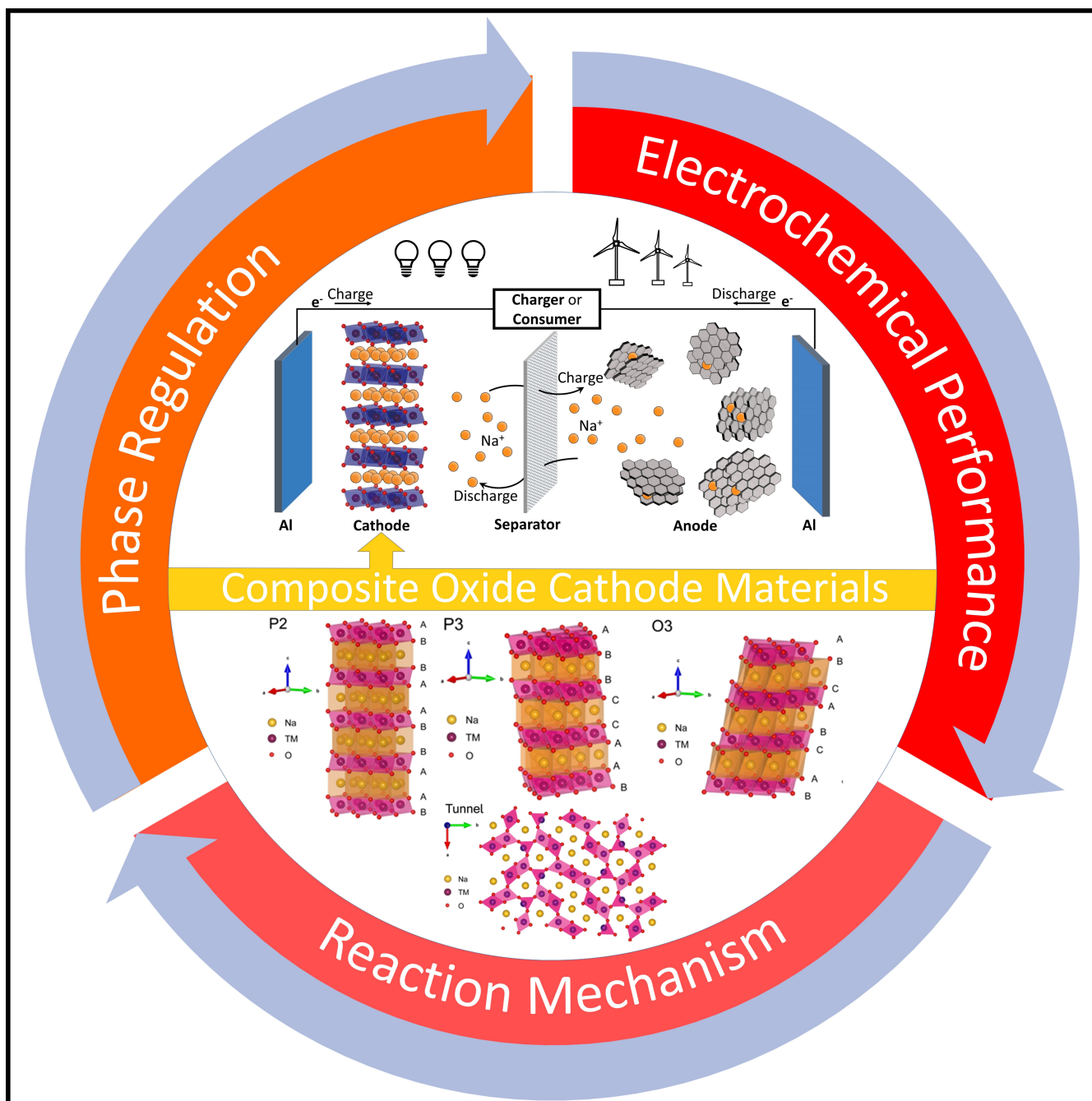


Sodium Composite Oxide Cathode Materials: Phase Regulation, Electrochemical Performance and Reaction Mechanism

Xu Zhu⁺^[a] Shao-Wen Xu⁺^[a] Xian-Zuo Wang,^[a] Mengting Liu,*^[a] Yonghong Cheng,^[a] and Peng-Fei Wang^{*[a]}



The abundance of sodium resources provides the basis for the large-scale application of sodium-ion batteries (SIBs) in the field of energy storage. Among the cathode candidates for SIBs, oxide materials stand out because of their ease of synthesis, environmental friendliness and high capacity. According to the crystal structure, oxide cathode materials can be mainly classified as P2, P3, O3 and tunnel phases. Benefiting from the combined advantages of different phases, composite oxide

cathode materials have been widely studied due to the enhanced both cycling and rate performance. In this review, we analyzed the three key issues of phase regulation, electrochemical performance and reaction mechanism based on the recent progress for composite oxide cathode materials. The composite oxide cathode materials will be one of the most competitive and attractive cathodes for SIBs.

1. Introduction

With the gradual deterioration of the environment, climate and the depletion of fossil fuels, renewable and clean energy sources (wind, solar, wave, and geothermal) are urgently needed to replace traditional fossil fuels that cause serious environmental pollution.^[1–3] However, these renewable energy sources are characterized by intermittent and erratic generation. Therefore, in order to integrate them into the grid, large-scale energy storage systems are necessary for peaking operations.^[4] Secondary batteries stand out from the numerous energy storage devices by virtue of their safety, low cost and high energy density, offering a promising approach to large-scale energy storage.^[5,6] Secondary batteries include lithium batteries, sodium batteries, NiMH batteries, NiCd batteries, and so on, among which lithium-ion batteries (LIBs) are the most widely used and the most rapidly developing as power batteries.^[7] Because of the huge demand for lithium, the price of battery-grade Li₂CO₃ is increasing year on year even as preparation processes continue to improve and new mine sources of Li are discovered. Furthermore, this upward trend is exacerbated by the scarcity and uneven distribution of lithium resources within the earth's crust. The high manufacturing costs of LIBs limit the application of Li resources for large-scale energy storage.^[8] In contrast to the scarcity of Li resources, sodium as the fourth most abundant element on earth, has nearly unlimited reserves, which provides a compelling case for developing sodium ion batteries (SIBs) as an alternative to LIBs in the energy storage field.^[9–11] As a matter of fact, SIBs have been investigated together with LIBs since the 1970s and 1980s because of their similar "rocking-chair" storage mechanism and physicochemical properties. However, many reasons hinder the development of SIBs. The first is that the energy density of LIBs is believed to be higher than that of SIBs. Both in terms of operating voltage and theoretical specific capacity, Li systems perform better than Na systems, so Li systems become a priority for development. On the other hand, research on SIBs

has been stagnant due to the lack of suitable anode materials and advanced techniques such as glove boxes to handle the chemically active sodium.^[3,12] In recent years, investigations on SIBs have sprung up based on the mature LIBs technology, and SIBs have the potential to be applied to large-scale energy storage.^[13–15]

As one of the cores of SIBs, the cathode material determines the energy density and lifetime of the batteries.^[16] The cathodes for SIBs can be mainly classified as oxides, Prussian blue analogues, polyanionic frameworks and organic compounds.^[17–29] Among these, oxide cathodes stand out for their facile synthesis, high specific capacity and high safety.^[30,31] The oxide cathodes for SIBs can be denoted by the general formula Na_xTMO₂. Sodium oxide cathodes have more diverse properties than lithium-ion oxide cathodes because transition metals (TM) such as Ti, V, Cr, Mn, Fe, Co, Ni and Cu can provide electrochemical activity without being limited to ternary layered material of Ni, Co and Mn.^[32–37] Sodium based oxide cathodes include layered oxides and tunnel oxides. The different structures of them result in distinct electrochemical properties. The distinctive characteristic of layered oxides is the TMO₂ layers, which typically consists of edge-sharing TMO₆ octahedra. When repeated layers are stacked in different positions along the c-axis, different oxygen stacking and electrochemical environments for Na⁺ emerge. The electrochemical environment of Na⁺ can be divided into O- and P-type, corresponding to the octahedral and prismatic sodium sites, respectively, while the numbers 2 or 3 represent the number of TMO₂ layers with different oxygen stacking in a single cell unit.^[38,39]

The structure, Na sites and diffusion pathways of O3, P2, P3 and tunnel are shown in Figure 1. O3-type layered oxide cathodes consist of cubic closely packed (ccp) arrays of oxygen in which the sodium and 3d TM ions with different ionic radii are located in different octahedral sites. Completely edge-shared NaO₆ and TMO₆ octahedra are arranged in alternating layers perpendicular to crystal direction [111], forming NaO₂ and TMO₂ layers, respectively. With a layered structure, O3-type NaTMO₂ is described crystallographically as a unit cell by three distinct TMO₂ layers (AB, CA and BC layers), with sodium ions accommodated in the octahedral sites between the TMO₂ layers. This kind of structure is also classified as a 3R phase with a space group of R̄3m. P2-type layered oxide cathodes consists of two kinds of TMO₂ layers (AB and BA layers), with Na⁺ located in trigonal prismatic sites. There are two types of prismatic sites, Na_f (Na₁) and Na_e (Na₂), which share faces and edges with the TMO₆ octahedra, respectively. Of these, the

[a] X. Zhu,⁺ S.-W. Xu,⁺ X.-Z. Wang, Dr. M. Liu, Prof. Y. Cheng, Prof. P.-F. Wang
 Center of Nanomaterials for Renewable Energy
 State Key Laboratory of Electrical Insulation and Power Equipment
 School of Electrical Engineering
 Xi'an Jiaotong University
 Xi'an, 710049 (China)
 E-mail: liumt39@outlook.com
 pfwang@xjtu.edu.cn

[+] These authors contribute equally to this work.

edge-shared prismatic sites are preferentially occupied by Na^+ , but the close proximity of the Na_f and Na_e sites causes Coulomb repulsion to be so strong that they cannot be occupied by Na^+ at the same time. The P2-type Na_xTMO_2 belongs to the 2H phase, $P6_3/mmc$ space group. In addition, when the structure is slightly distorted, a prime symbol ('') is added to the structure symbol in order to distinguish it from the original structure, as in the case of the monoclinic lattice of O'3 NaMnO_2 (space group $C2/m$)^[40,41] and the orthorhombic lattice of P'2 Na_xMnO_2 (space group $Cmcm$).^[42-44]

P3-type phase appears more often in the form of a transition phase during the charging and discharging process of O3-type cathodes, except for direct crystallization,^[45] though it is a thermodynamically stable structure. The (de)intercalation of Na^+ leads to changes in the electrostatic repulsion of the adjacent oxygen stackings, which is the main cause of the phase transition.^[46] In the O3-type phase, Na^+ are located in the octahedral sites sharing edge with the TMO_6 octahedra, while when they extract form Na layers, the original octahedra are distorted into triangular prisms due to the sliding of the TMO_2 layer. Meanwhile, the order of oxygen stackings changes from the original ABCABC to ABBCCA, which belongs to P3-type phase.^[47] In contrast, O2-type phase is thermodynamically unstable and usually appears in the high voltage region of P2-type phase. The sliding leads to the transition of triangular prisms to the octahedra and the unique oxygen stackings order (ABAC) of O2-type phase.^[48] The O2-type phase is similar to O3-type phase with octahedral Na^+ sites and closely packed

oxygen arrays, but differs in the local existence of hexagonal closely packed (*hcp*) oxygen arrays (ABA- and ACA-type oxygen stackings). Therefore, the O2-type can be considered as an intergeneric structure between the *ccp* and *hcp* arrays.^[12]

The different structures of the O- and P-type phases differentiate their Na^+ diffusion pathways. In the O-type structure, Na^+ can only diffuse through the tetrahedral vacancies between two octahedral sites. In contrast, Na^+ can diffuse directly through adjacent prismatic sites in the P-type phase, providing a lower transfer barrier and thus a higher Na^+ diffusion coefficient.^[12,49] Furthermore, P2-type structure exhibits better Na^+ transport properties than the P3-type structure, even though both have prismatic sodium sites.^[50,51] Under the multi-vacancies (Na-deficiency) condition of the P2-type phase, the electrostatic repulsion between the TM layers raises the energy of Na_f sites, making the energy barrier to Na^+ migration lower than in the P3 phase structure. Tunnel oxide cathode materials also have great Na^+ diffusion coefficient by virtue of their special tunneling structure. Taking $\text{Na}_{0.44}\text{MnO}_2$ as an example, there are five Mn sites and three Na sites, with Mn_1 and Mn_2 occupied by Mn^{3+} and Mn_3 , Mn_4 and Mn_5 occupied by Mn^{4+} .^[52] The whole structural framework consists of MnO_6 octahedra and MnO_5 square pyramids, forming two Na^+ diffusion pathways: hexagonal tunnels occupied by Na_1 ions and S-shaped tunnels occupied by Na_2 and Na_3 ions. Due to unique S-shaped Na^+ diffusion pathways and stable structure framework, the tunnel phase cathodes exhibit excellent rate performance and cycling stability.^[53-55]



Xu Zhu received his bachelor's degree in both Engineering and Economics in Xi'an Jiaotong University from 2018 to 2022. He is currently a Ph.D. student at School of Electrical Engineering in Xi'an Jiaotong University, supervised by Prof. Peng-Fei Wang. His research focuses on layered cathode materials for sodium-ion batteries.



Shaowen Xu received his Bachelor degree in Electrical Engineering at Southwest Jiaotong University (2021). Now he is a master's candidate at School of Electrical Engineering in Xi'an Jiaotong University and focus on layered oxide cathodes for sodium-ion batteries.



Dr. Mengting Liu is an assistant professor at School of Electrical Engineering in Xi'an Jiaotong University. She received her Ph.D. in Condensed Matter Physics at Lanzhou University, China in 2021. She worked at Georgia Institute of Technology as a visiting scholar from 2018 to 2020. Her ongoing research interests embrace materials design as well as interface reaction related to Li/Na-ion batteries, Li-S batteries and waste battery recycling.



Prof. Yonghong Cheng is a full professor at School of Electrical Engineering, Xi'an Jiaotong University. He received his Ph.D. degrees in Electrical Engineering from Xi'an Jiaotong University (1999). He was awarded the Chang Jiang Scholar Professor in 2009. He is currently the Director of Integrated Energy Systems and Energy Storage Research Department, State Key Laboratory of Electrical Insulation and Power Equipment. His team focuses on the research and application of new energy storage materials and energy conversion technologies.



Prof. Peng-Fei Wang is a full professor at School of Electrical Engineering in Xi'an Jiaotong University. He received his Ph.D. degree in Physical Chemistry from Institute of Chemistry, Chinese Academy of Sciences (2018). He was a postdoctoral fellow at University of Maryland at College Park from 2018 to 2020. His research interests focus on high-energy and low-cost cathode materials for Li/Na/K/Zn-ion batteries and waste battery recycling.

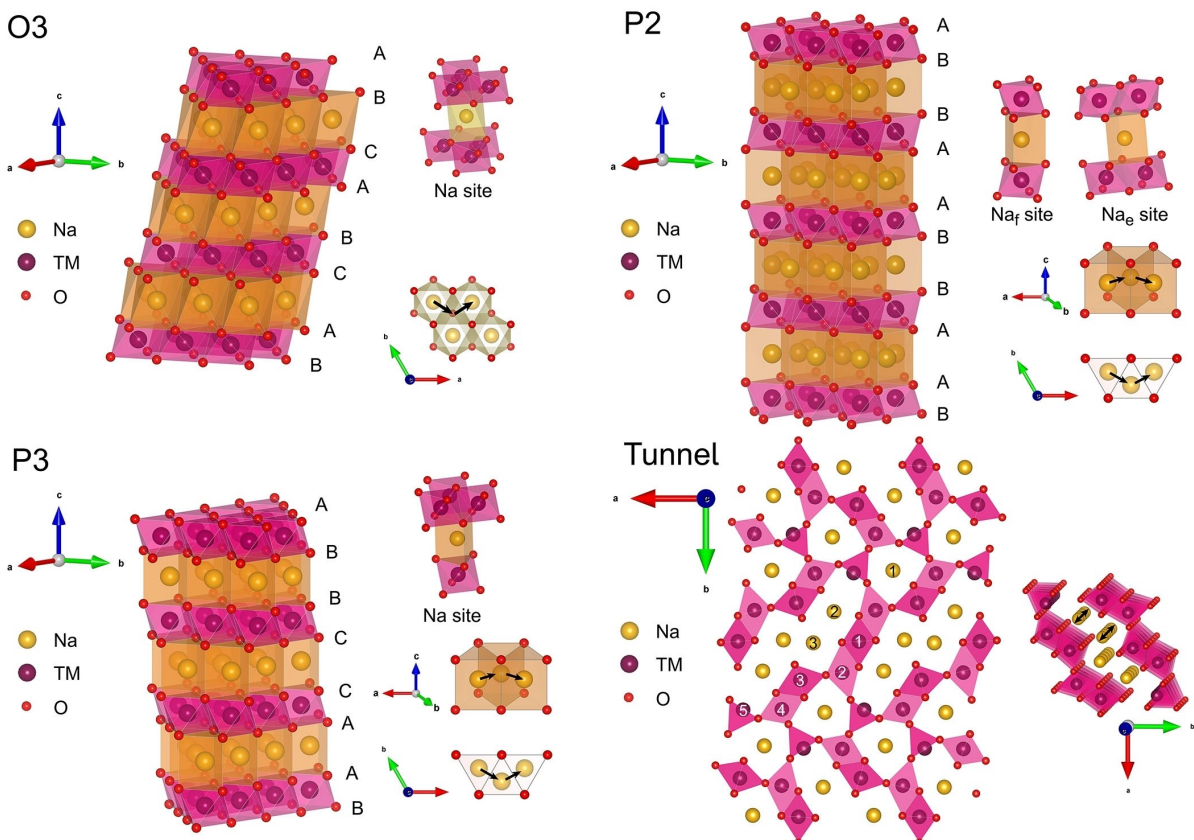


Figure 1. The schematic diagram of structure, Na site and diffusion path of O3, P2, P3 and tunnel.

However, single-phase cathode materials often have inherent deficiencies. In P-type and tunnel-type phase cathodes, the special structures enable the fast ion diffusion and good structure stability, but low sodium content ($x < 0.7$ in Na_xTMO_2) results in low initial specific capacity. While in O3-phase materials, the sufficient Na content ($0.8 < x \leq 1$ in Na_xTMO_2) contributes to higher initial specific capacity, but complex phase transitions (such as O3-P3-P'3-O'3) cause poor stability.^[40] Hence, it is difficult for single-phase cathodes to achieve a comprehensive combination of the remission of phase transition, satisfactory electrochemical and reaction kinetics. In order to compensate for the deficiencies of single-phase structures and achieve a comprehension improvement, it is a promising strategy to prepare composite oxide cathode materials by elemental substitution, adjustment of sodium content and calcination temperature.

Although composite cathode materials have excellent performance, there is a lack of instructional design methods, systematic generalization of performance and exploration of performance enhancement mechanisms. In this review, we summarize and analyze recent researches on composite oxide cathode materials in the order of regulation-performance-mechanism. The phase regulation is summarized from three perspectives: elemental substitution, sodium content and calcination temperature. The review then summarizes the excellent electrochemical performance of typical composite oxide cathode materials and the performance enhancement

mechanism that have been explored. Finally, we conclude with an outlook for the future development of sodium composite oxide cathode materials, with the aim of grasping insight into subsequent researches on composite oxide cathode materials.

2. Phase Regulation

The ratio of different phases in a composite structure can seriously affect the properties of the material, so the method of regulating the structure becomes essential. In this review, we summarize the strategy of phase regulation as elemental substitution, adjustment of the sodium content, and control of the calcination temperature. Numerous studies have explored the design methods and formation mechanisms of composite structures around these three regulation methods. In particular, based on the concept of cationic potential, we conclude that materials with cationic potential close to the dividing line tend to form P2/O3 composite structure.

2.1. Elemental substitution

Transition metal elements play a dominant role in oxide cathodes, and by the new elements occupying the pristine TM sites, the structure and properties of cathodes can be regulated.

2.1.1. P2/O3 composite structure

The P2/O3 composite structures, with their high Na content and stable structure, become the most studied composite oxide cathode materials.

$\text{P2-Na}_{2/3}\text{Ni}_{1/3}\text{Mn}_{2/3}\text{O}_2$ is a classical layered material with great electrochemical performance and low cost, which is considered as one of the most promising cathode candidates.^[65,66] As a platform material, there is great potential for elemental substitution to tune the structure and properties of $\text{P2-Na}_{2/3}\text{Ni}_{1/3}\text{Mn}_{2/3}\text{O}_2$. The element Sn is often present as a positive tetravalent ion and by occupying the Mn^{4+} sites in the TM layers, structural regulation can be achieved.^[56,57] When the amount of Sn substitution is between 0 and 0.4, the O3 phase becomes progressively more abundant as the amount of Sn increases. The anomaly of the P2/O3 composite structure at

low sodium content may be related to $\text{Ni}^{2+}/\text{Sn}^{4+}$ cationic disordering caused by the same ionic radius of Ni^{2+} (0.69 Å) and Sn^{4+} (0.69 Å).^[67] Sn^{4+} occupying the site of Mn^{4+} (0.53 Å) would lead to an increased disordering of Ni/Mn in the TM layer, thus altering the structure of the material. As Sn replaces more Mn, the O3-type structure takes up a greater ratio in the composite structure (Figure 2a).^[56] Besides, when the amount of Sn substitution is at 0.1, the percentage of P2 and O3 is almost the same. Similarly, the study of Rong *et al.* showed the same trend of evolution.^[57] As x (x in $\text{Na}_{2/3}\text{Ni}_{1/3}\text{Mn}_{2/3-x}\text{Sn}_x\text{O}_2$) increases, crystal structure changes from a pure P2 phase ($x=0$) to a composite structure of P2 and O3 phases ($x=0.10, 0.20, 0.30$) and eventually to a pure O3 phase ($x=0.33$) (Figure 2b). Interestingly, unlike the $\text{O3-Na}_{0.67}\text{Ni}_{0.33}\text{Mn}_{0.33}\text{Sn}_{0.33}\text{O}_2$ synthesized by Rong *et al.*,^[57] the $\text{Na}_{2/3}\text{Ni}_{1/3}\text{Mn}_{1/3}\text{Sn}_{1/3}\text{O}_2$ synthesized by Xiao *et al.* turned out to be P2/O3-type structure^[68], which may be

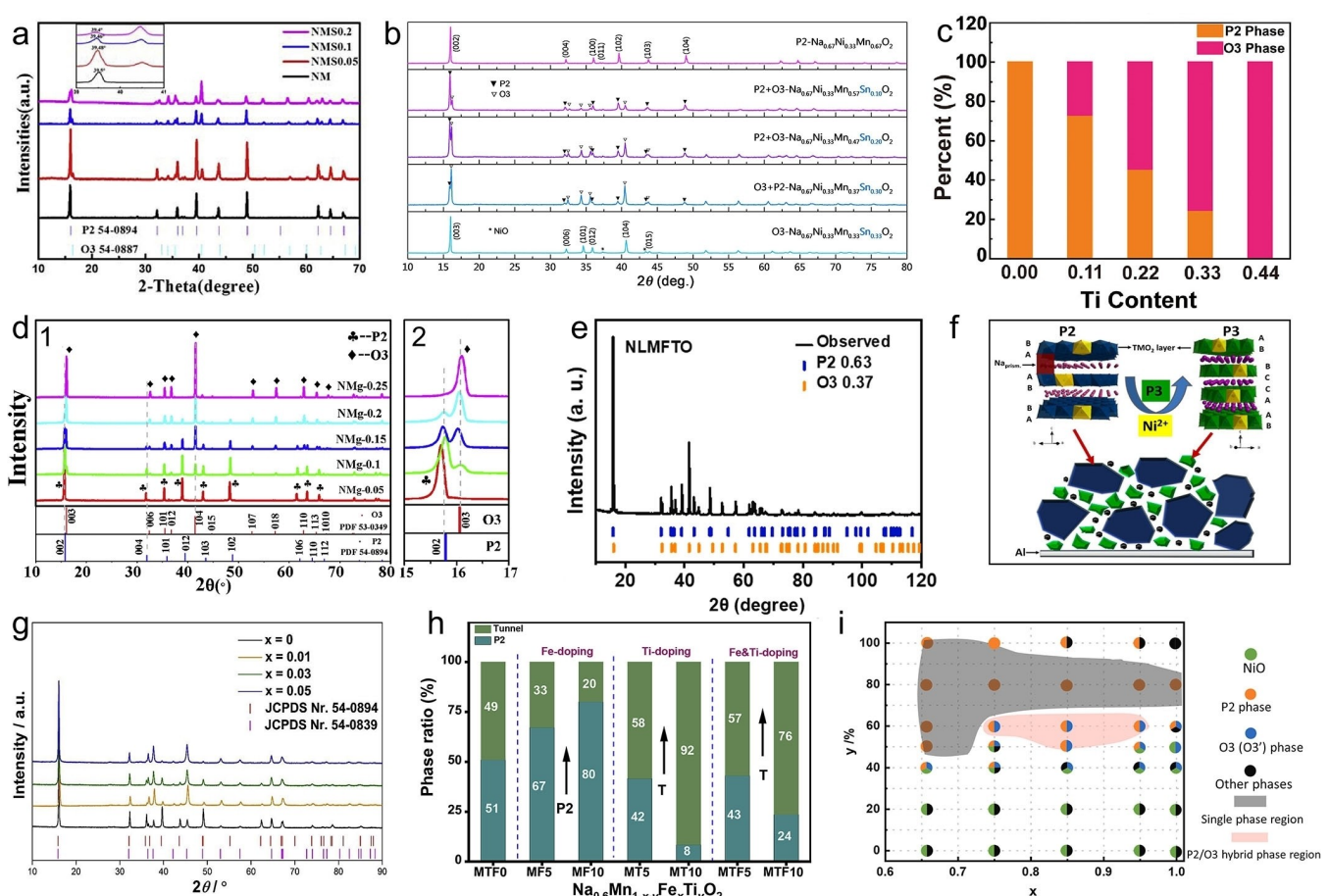


Figure 2. a) XRD patterns of Sn-substituted Ni/Mn-based $\text{Na}_{0.67}\text{Ni}_{0.33}\text{Mn}_{0.67-x}\text{Sn}_x\text{O}_2$ ($x = 0, 0.05, 0.1, 0.2$). Inset: the magnification of 39°–41°. Reproduced with permission from Ref. [56]. Copyright (2019) Elsevier. b) XRD patterns of Sn-substituted Ni/Mn-based $\text{Na}_{0.67}\text{Ni}_{0.33}\text{Mn}_{0.67-x}\text{Sn}_x\text{O}_2$ ($x = 0, 0.10, 0.20, 0.30, 0.33$). Reproduced with permission from Ref. [57]. Copyright (2019) Elsevier. c) Schematic diagram showing phase proportion of materials with varying Ti content. Reproduced with permission from Ref. [58]. Copyright (2022) Elsevier. d) XRD patterns of Mg-substituted Fe/Mn-based $\text{Na}_{0.67}(\text{Fe}_{0.5}\text{Mn}_{0.5})_{1-x}\text{Mg}_x\text{O}_2$ ($x = 0.05, 0.1, 0.15, 0.2, 0.25$), the magnification of 15°–17° is shown in the right. Reproduced with permission from Ref. [59]. Copyright (2019) Elsevier. e) XRD patterns of Li/Ti co-substituted $\text{Na}_{0.67}\text{Li}_{0.11}\text{Fe}_{0.36}\text{Mn}_{0.36}\text{Ti}_{0.17}\text{O}_2$. Reproduced with permission from Ref. [60]. Copyright (2021) Elsevier. f) Schematic illustrations of the P2/P3 crystal structures and optimization design strategy with particles in different sizes for high tap density cathode materials. Reproduced with permission from Ref. [61]. Copyright (2019) Wiley-VCH. g) XRD patterns of $\text{Na}_{0.67}\text{Ni}_{0.33}\text{Mn}_{0.67}\text{O}_2$ (black), $\text{Na}_{0.67}\text{Ni}_{0.33}\text{Mn}_{0.66}\text{Sn}_{0.01}\text{O}_2$ (yellow), $\text{Na}_{0.67}\text{Ni}_{0.33}\text{Mn}_{0.64}\text{Sn}_{0.03}\text{O}_2$ (green) and $\text{Na}_{0.67}\text{Ni}_{0.33}\text{Mn}_{0.62}\text{Sn}_{0.05}\text{O}_2$ (blue). Reproduced with permission from Ref. [62]. Copyright (2019) Elsevier. h) XRD Rietveld refinements ratio of P2 layer/tunnel phase of MFT0 ($\text{Na}_{0.60}\text{Mn}_{0.40}\text{O}_2$), MF5 ($\text{Na}_{0.60}\text{Mn}_{0.95}\text{Fe}_{0.05}\text{O}_2$), MF10 ($\text{Na}_{0.60}\text{Mn}_{0.90}\text{Fe}_{0.1}\text{O}_2$), MT5 ($\text{Na}_{0.60}\text{Mn}_{0.95}\text{Ti}_{0.05}\text{O}_2$), MT10 ($\text{Na}_{0.60}\text{Mn}_{0.90}\text{Ti}_{0.1}\text{O}_2$), MFT5 ($\text{Na}_{0.60}\text{Mn}_{0.90}\text{Fe}_{0.05}\text{Ti}_{0.05}\text{O}_2$) and MFT10 ($\text{Na}_{0.60}\text{Mn}_{0.80}\text{Fe}_{0.10}\text{Ti}_{0.10}\text{O}_2$). Reproduced with permission from Ref. [63]. Copyright (2020) from Elsevier. i) Synthesis phase diagram of $\text{Na}_x\text{Mn}_y\text{Ni}_{1-y}\text{O}_2$ (0.66 ≤ x ≤ 1 and 0 ≤ y ≤ 100%) with the sintering temperature of 900 °C. Reproduced with permission from Ref. [64]. Copyright (2021) Elsevier.

attributed to subtle differences in synthesis methods (precursor, calcination temperature and cooling method). This needs to be explored and confirmed even further. Based on P2-Na_{2/3}Ni_{1/3}Mn_{2/3}O₂, Sb-substituted Na_{0.62}Ni_{0.33}Mn_{0.62}Sb_{0.05}O₂ consists of 68.78% P2 phase and 31.22% O3 phase, indicating the substitution of Sb⁵⁺ can also lead to P2/O3 composite structure.^[69] Another Ni/Mn based example is P2-Na_{0.85}Ni_{0.34}Mn_{0.66}O₂.^[58] As mentioned before, the substitution of Ti for Mn can facilitate the formation of O3-type structure because Mn⁴⁺ has a greater ionic potential than Ti⁴⁺, which is consistent with the evolution of crystal structure of Ti-substituted Na_{0.85}Ni_{0.34}Mn_{0.66-x}Ti_xO₂ (Figure 2c). When the substitution content of Ti is low ($x=0.11, 0.22$ and 0.33), the crystal structure is P2/O3 composite structure. However, as the substitution content of Ti increases further, the crystal structure of P2-Na_{0.85}Ni_{0.34}Mn_{0.22}Ti_{0.44}O₂ transforms into a pure O3 phase.

For the Fe/Mn based P2-Na_{0.67}Fe_{0.5}Mn_{0.5}O₂, elemental substitution is also effective in forming P2/O3 composite structure. The fact that crystal structure of Mg-substituted Na_{0.67}(Fe_{0.5}Mn_{0.5})_{1-x}Mg_xO₂ changes from a pure P2 phase ($x=0, 0.05$) to P2/O3 composite structure ($x=0.1, 0.15$ and 0.2) and eventually to a pure O3 phase ($x=0.25$) suggests the substitution of Mg facilitates the formation of O3-type structure (Figure 2d).^[59] Li/Ti co-substituted Na_{0.67}Li_{0.11}Fe_{0.36}Mn_{0.36}Ti_{0.17}O₂ also exhibits P2/O3 composite structure (Figure 2e).^[60]

In addition to Na-P2/Na-O3 composite structure, Li-substitution enables the introduction of Li into alkali layers, leading to the formation of Na-P2/Li-O3.^[67-74] Li-substitution is relatively special because most of the introduced Li will occupy the transition metal layer, while a certain amount will also occupy the Na layer, and the Li occupying the Na layer will cause a P2-O3 phase evolution. Further studies reveal that Li will completely occupy this part of the alkali layer, forming a special Li-O3 phase.^[70-77] In addition, this special structure can inhibit the phase transition of the pristine P2 structure and thus enhance the electrochemical performance. As for Fe/Mn based materials, the introduction of Li will cause the valence states of Fe and Mn to rise, and since the ionic radii of Mn⁴⁺ is different from that of Fe³⁺ and Li⁺, if Li is introduced in the certain amount it will lead to an ordering of the arrangement of Li and Fe.^[72-74,76,78] This ordering in TM layer is also known as superstructure and is common in Li-containing materials.

2.1.2. P2/P3 composite structure

Elemental substitution also has an effect on the P2/P3 composite structure, although the effect of calcination temperature is more dominant, as will be summarized later. P2/P3 composite structures mostly use Mn-based and Ni/Mn-based materials as platform materials. When Mn is replaced by Ni, the structure of Na_{0.6}Ni_xMn_{1-x}O₂ gradually changes from P2 to P3 as the amount of Ni increases, with the original large particles of P2 structure gradually breaking into smaller particles of P3 structure (Figure 2f).^[61] Under lower calcination temperatures, the substitution of Sn⁴⁺ for Mn⁴⁺ also leads to the formation of a P2/P3 composite structure, rather than the P2/O3 composite

structure mentioned above.^[62] The P3-type structure in the Na_{0.67}Ni_{0.33}Mn_{0.67-x}Sn_xO₂ ($x=0, 0.01, 0.03, 0.05$) gradually increased as the Sn substitution increased from 0 to 0.05 (Figure 2g). Since the precursors are obtained by co-precipitation, the pH value and annealing temperature have a strong influence on the material.^[79,80] On the one hand, lowering the temperature made it more favorable to obtain the P2/P3 composite structure,^[81] and on the other hand, more P3 structures were generated due to the partial hydrolysis of Sn⁴⁺ during the precipitation process, which lowered the pH value of the mixture solution. In addition to the pH value of the co-precipitated solution, ionic rearrangements in the cell unit can also explain the reason for the change in structure.^[82] The introduction of Co, for example, leads to changes in the Na environment and structural distortions that result in the rearrangement of ions to form composite structures. Additionally, a novel synthetic approach, dealloying-annealing strategy, was used in the preparation of the P2/P3-Na_{0.67}Mn_{0.64}Co_{0.30}Al_{0.06}O₂ cathode.^[83] Compared to Co doping by co-precipitation, sol-gel and solid-phase methods, dealloying is more controllable, which is more favorable for P2/P3 composite cathodes that rely on tuning the synthesis conditions for preparation.^[84-86]

2.1.3. Layered-tunnel composite structure

Layered structure cathodes have the potential to become the cathode material for sodium-ion batteries with their stable structure. Because the tunnel phase cathodes have a relatively low Na content, it is suitable for composite with low-sodium P2-type structures, which can be designed with an initial Na content above 0.44 (pure tunnel phase) and less than 0.67 (pure P2 phase). Based on the summary of recent studies, the Na content of layered-tunnel composite phase cathodes is suitable at 0.6. On the other hand, the properties of the composite structural material can be tuned by the transition metal elements occupying the Mn sites in the tunnel framework. According to the above two principles, the chemical formula of the layered-tunnel (L-T) composite phase can be obtained as Na_{0.6}Mn_xTM_{1-x}O₂.

When a small amount of Ni is substituted for Mn, the layered structure in the material increases.^[87] Interestingly, depending on the amount of Ni substitution, Na_{0.6}Ni_xMn_{1-x}O₂ can also be a P2/P3 composite structure.^[61] When the substitution $x<0.1$, the material tends to be a composite of the P2 and tunnel phases; when the substitution $x>0.1$, the material is a P2/P3 composite phase. We attribute this phenomenon to the ambiguous Na content, which we will explain in more detail in the next section regarding Na content and composite structure. Cu substitution for Mn is also an effective way to regulate the L-T structure. When the amount of Cu substitution increases, the proportion of the layered structure increases.^[88] It is possible that Cu occupies the Mn₅ position and disrupts the tunnel structural framework. When elemental substitutions are made using alkali metal ions instead of transition metal elements, occupancy sites need to

be designed. For example, when the Mg ion occupies the Mn site, it increases the layered structure in the composite, while when it occupies the Na site, the material tends more towards the tunnel phase.^[89] If multi-element substitution is involved, it is necessary to determine the role of the different ions, e.g., when Fe/Ti co-substitutes for Mn, Fe adds to the P2-type structure, while Ti adds to the tunnel structure.^[63] However, Ti plays a dominant role and when both Fe and Ti occupy the Mn sites and have the same amount of substitution, the material is more inclined to tunnel structure (Figure 2h).

In conclusion, elemental substitution such as Li⁺, Mg²⁺, Ni²⁺, Cu²⁺, Fe³⁺, Ti⁴⁺, Sn⁴⁺ and Sb⁵⁺ etc. can have an important effect on the crystal structure, thus regulating the ratio of different phases in a composite structure and improving the electrochemical properties. This strategy is widely used and investigated because it is effective in many different composite types, such as P2/O3, P2/P3, and layered-tunnel composite structures. However, the mechanism of the change in the ratio of different phases in a composite structure caused by elemental substitution needs to be further investigated.

Most of the above studies have focused on qualitative studies, while quantitative studies, i.e., the cationic potential, will be described later in this chapter.

2.2. Sodium content

The sodium content is also a key factor in the crystal structure of sodium composite oxide cathode materials. When the sodium content is less than 0.5 (0.44 or 0.4), the oxide cathodes tend to form tunnel structure.^[90,91] P2-type structure is usually formed at relatively low sodium content ($0.6 < x < 0.7$), whereas O3-type structure is usually formed at high sodium content ($0.8 < x \leq 1$).^[92-94] Several of these structures are relatively sensitive to changes in sodium content and can be compounded by regulating the sodium content.

Composite structures of tunnel and P2-type structures are often found at low sodium content condition, so the layered-tunnel composite phase is commonly optimized with Na_{0.6}MnO₂ as a platform material.^[91] Since most L-T composite cathodes are prepared by co-precipitation followed by solid state method, the dissimilar thermal decomposition behavior of Na sources can lead to differences in the properties of the cathode materials.^[95,96] Among them, Na_{0.6}MnO₂ using Na₂C₂O₄ and CH₃COONa as sodium sources have relatively good performance, which is related to the appropriate ratio and the synergistic effects of layered and tunnel structures in the material. In addition, L-T composite phases with lower sodium content also exist, such as Na_{0.44}Co_{0.1}Mn_{0.9}O₂^[97,98] and Na_{0.44}MnO_{1.93}F_{0.07},^[99] which transform the tunnel structure into P2-type layered structure through elemental doping and substitution.

At high sodium content, the P2/O3 composite structure is more sensitive to changes in Na content. Figure 2(i) is the diagram summarizing the phases of the Na_xMn_yNi_{1-y}O₂ materials with various Na contents ($0.66 \leq x \leq 1$) and Ni/Mn ratios ($0 \leq y \leq 1$).^[64] The results show that P2 phase is readily formed in

sodium-deficient Mn-rich environments and meanwhile, the increasing sodium content ($0.75 < x < 0.95$) leads to the appearance of P2/O3 composite phases at appropriate Ni/Mn ratios such as Na_xNi_{0.4}Mn_{0.6}O₂. According to XRD refinement, the proportion of O3-type phase in the composite structures raises as the sodium content increases. This is because the increase in Na ions enhance the electrostatic shielding between adjacent oxygen layers and reduces the electrostatic repulsion, resulting in shorter Na layer spacing and thus obtaining the O3-type phase; conversely, if the electrostatic repulsion plays a major role, the P2-type phase is formed.^[102]

2.3. Calcination temperature

The synthesis of layered oxide cathodes tends to involve solid-state reaction, and the relationship between the thermodynamic properties of the cathodes and their structures is complex. The cationic potential provides some guidance in predicting P2 or O3 type stacking. However, there are many limitations in the use of cationic potential and the formation of the P3 phase is not considered. When changing temperature, the kinetics and thermodynamics of the materials are intricate and cannot be predicted using the cationic potential. However, the sensitivity of the layered structure to the calcination temperature has led to relevant studies that can qualitatively summarize the effect of calcination temperature on the composite structure. Gerbrand Ceder and co-workers investigated the effect of temperature on the structure of Na_{0.7}CoO₂ by *in situ* characterization techniques (Figure 3a and b).^[100] For P2-Na_{0.7}CoO₂, the P3 structure appeared at calcination temperatures up to 850°C and the P2 structure was obtained at temperatures up to 950°C. Whereas for different Na contents, the materials show different sensitivity to temperature. This is because cathodes with different sodium contents have different thermodynamic stability, such as NaCoO₂ which has a thermodynamic preference to form O3 structures, while Na_{0.67}CoO₂ prefers to form P2 structures. This further explains the effect of the sodium content on the composite structure in terms of thermodynamics. When the sodium content is appropriate, the formation energy of P2, P3 and O3-type structures is similar, leading to the formation of composite phases.

Wang and co-workers have experimentally verified that sodium content and temperature have a correlative effect on the composite structure.^[49] By controlling the sodium content by varying it from 0.67 to 1 [(100-x)% P2-Na_{2/3}Ni_{1/3}Mn_{0.57}Ti_{0.1}O₂ + x% O3-NaNi_{1/3}Fe_{1/3}Mn_{1/3}O₂] and at different calcination temperatures, the authors synthesized 77 sets of layered cathodes and analyzed the phase structure (Figure 3c). P3-type structure is formed under sodium deficient state ($x=0, 10$ and 20) and low calcination temperature (around 700°C). When the calcination temperature is 800°C and the sodium content is in the middle ($10 \leq x \leq 60$), P2/O3 composite structure is formed. However, as the calcination temperature increases, the crystal structure of some samples ($x=10, 50$ and 60) become single phase, which is consistent with the relationship between crystal structure and thermodynamic driving force studied by Ji *et al.*^[103] As for

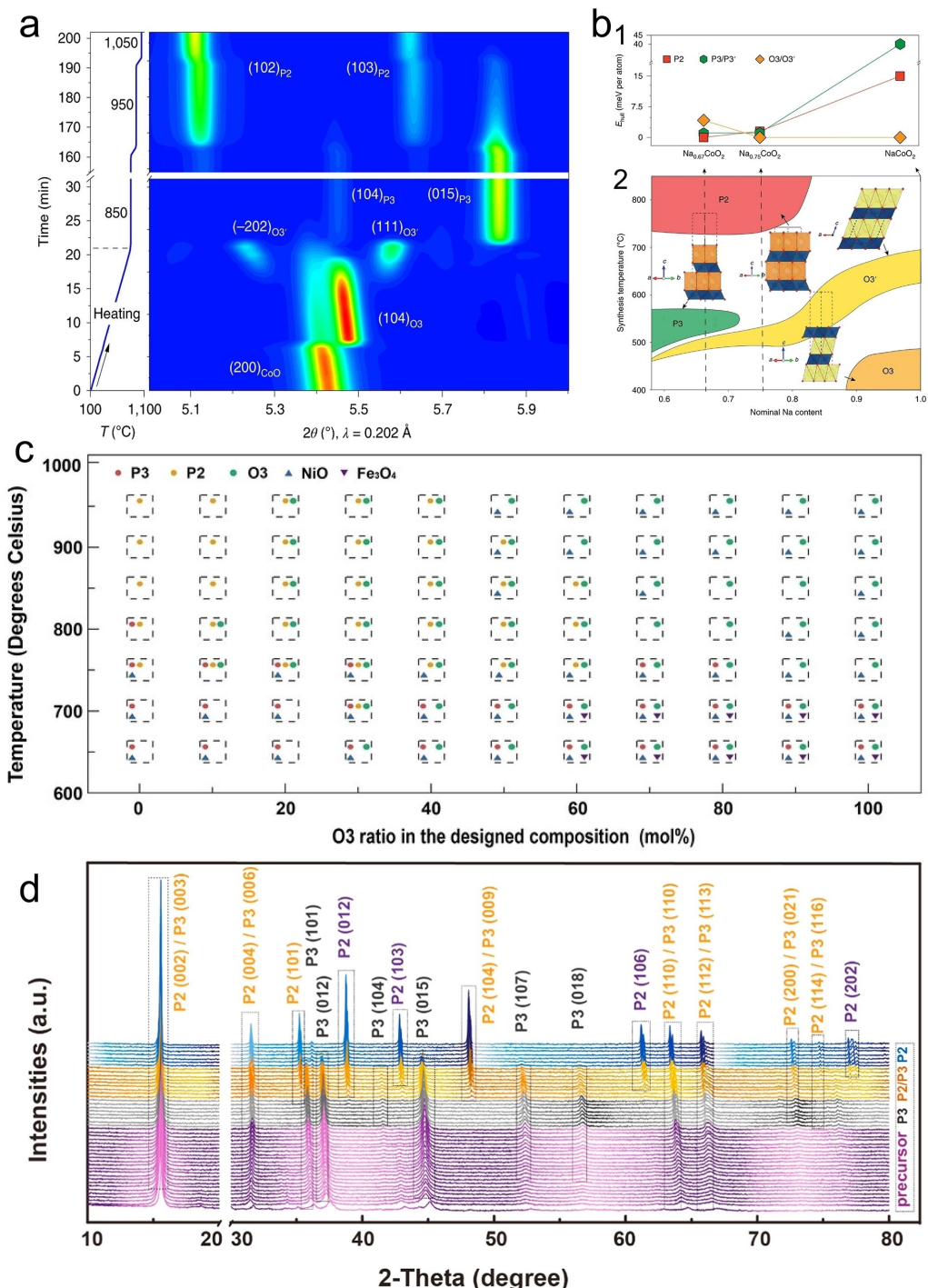


Figure 3. a) Contour plot highlighting the evolution of the Bragg peaks. The material undergoes a phase transition of O_3 - O_3' - $\text{P}3$ - $\text{P}2$ during the heating process. b₁) Energy above the convex hull (E_{hull}) of the various polytypes of Na_xCoO_2 in their lowest-energy Na/vacancy configuration at $x = 0.67, 0.75$ and 1 , calculated with the DFT-SCAN meta-GGA functional. b₂) Structural phase diagram of NaCoO_2 at different calcination temperatures and sodium contents under air atmosphere. Reproduced with permission from Ref. [100]. Copyright (2020) Springer Nature. c) Structural phase diagram of the material at different calcination temperatures and O_3 ratios in the design composition. Reproduced with permission from Ref. [49]. Copyright (2022) Wiley-VCH. d) High temperature XRD patterns of the calcination process for the synthesis of $\text{P}2/\text{P}3\text{-Na}_{0.7}\text{Li}_{0.06}\text{Mg}_{0.06}\text{Ni}_{0.22}\text{Mn}_{0.67}\text{O}_2$. The precursor undergoes a $\text{P}3\text{-P}2/\text{P}3\text{-P}3$ phase transition during the heating process. Reproduced with permission from Ref. [101]. Copyright (2018) Elsevier.

other samples ($x = 20, 30$ and 40), their cationic potential is close to the boundary of $\text{P}2$ and $\text{O}3$ phase, resulting in a still $\text{P}2/\text{O}3$ composite structure even at high calcination temperature. In other words, an appropriate reduction in calcination

temperature can increase the inhomogeneity of cationic potential, thus forming a $\text{P}2/\text{O}3$ composite structure. The above shows that sodium content and calcination temperature are two factors that cannot be considered separately for the

composite oxide cathode materials. The P2/P3 composite is more sensitive to changes in calcination temperature.^[79,101,104] For example, Guo and co-workers used high-temperature *in situ* XRD (Figure 3d) to study the structural evolution in P2/P3-Na_{0.7}Li_{0.06}Mg_{0.06}Ni_{0.22}Mn_{0.67}O₂ material ranging from 450 °C to 900 °C.^[101] Note that the P3 and P2 phases are synthesized below 750 °C and above 830 °C respectively, while the P2/P3 composite phase is obtained at around 850 °C. From a review of the literature, 800–850 °C is the suitable calcination temperature for most P2/P3 composite cathode.

2.4. Cationic potential

As discussed in Section 2.2, sodium content is one of the key factors affecting the formation of P2- and O3-type layered oxides from a qualitative perspective. However, the “cationic potential” is a quantitative method to predict P2 or O3 type stacking, which takes into account both sodium content (x in Na_xTMO₂) and the composition of the transition metal (TM in Na_xTMO₂).^[102] The cationic potential Φ_{cation} and average Na ionic potential $\overline{\Phi}_{\text{Na}}$ can reflect the competition between P2- and O3-type structures. The higher the value of $\overline{\Phi}_{\text{Na}}$, the stronger shielding effect of the electrostatic repulsion between adjacent TM layers, which can lead to O3-type stacking. Conversely, materials with high Φ_{cation} tend to form P2-type structure. Furthermore, a summary of the Φ_{cation} and $\overline{\Phi}_{\text{Na}}$ for P2- and O3-type layered oxides shows that $\overline{\Phi}_{\text{Na}} = 0.4065 \times \Phi_{\text{cation}} + 1.572$

is the dividing line separating the P2- and O3-type phases. The detailed method for calculating the cationic potential of Na_x[A^{n_a}_{ω_a}B^{n_b}_{ω_b} · · · · ·]O₂ ($\sum \omega_i = 1$) is as follows.

$$\overline{\Phi}_{\text{Na}} = \frac{x}{R_{\text{Na}}} \quad (1)$$

$$\overline{\Phi}_{\text{TM}} = \sum \frac{\omega_i n_i}{R_i} \quad (2)$$

$$\Phi_{\text{cation}} = \frac{\overline{\Phi}_{\text{Na}} \bullet \overline{\Phi}_{\text{TM}}}{\overline{\Phi}_{\text{anion}}} \quad (3)$$

This review calculates the cationic potential of P2/O3 composite structure materials. In addition, we also calculate the distance (d) from the (Φ_{cation} , $\overline{\Phi}_{\text{Na}}$) point to the dividing line $\overline{\Phi}_{\text{Na}} = 0.4065 \times \Phi_{\text{cation}} + 1.572$.

$$d = \frac{|0.4065 \times \Phi_{\text{cation}} + 1.572 - \overline{\Phi}_{\text{Na}}|}{\sqrt{0.4065^2 + 1^2}} \quad (4)$$

The Φ_{cation} , $\overline{\Phi}_{\text{Na}}$ and d of P2/O3 composite structure materials and some typical P2 or O3 phase materials are summarized in the Table 1. The comparison reveals the trend that composite structure materials have smaller d compared to single phase materials. Besides, the d of most P2/O3 composite structure materials is less than 0.4. Figure 4 reflects this trend more clearly.

Table 1. A summary of the Φ_{cation} , $\overline{\Phi}_{\text{Na}}$ and d of P2/O3 composite structure materials and some typical P2 or O3 phase materials.

Material	$\frac{\Phi_{\text{Na}} + \Phi_{\text{TM}}}{\Phi_{\text{anion}}}$	$\overline{\Phi}_{\text{Na}}$	$\overline{\Phi}_{\text{TM}}$	d
P2/O3-Na _{0.74} Ni _{0.20} Fe _{0.40} Mn _{0.40} O ₂ ^[105]	14.2363	7.2549	56.0656	0.0965
P2/O3-Na _{0.76} Ni _{0.20} Fe _{0.40} Mn _{0.40} O ₂ ^[105]	14.4928	7.4510	55.5739	0.0114
P2/O3-Na _{0.78} Ni _{0.20} Fe _{0.40} Mn _{0.40} O ₂ ^[105]	14.7426	7.6471	55.0822	0.0762
P2/O3-Na _{0.88} Ni _{0.45} Mn _{0.55} O ₂ ^[106]	16.6213	8.62745	55.0446	0.2769
P2/O3-Na _{0.85} Ni _{0.34} Mn _{0.33} Ti _{0.33} O ₂ ^[58]	15.0656	8.3333	51.6557	0.5902
P2/O3-Na _{0.8} Mn _{0.55} Ni _{0.25} Fe _{0.1} Ti _{0.1} O ₂ ^[107]	14.8856	7.8431	54.2265	0.2039
P2/O3-Na _{0.67} Ni _{0.33} Mn _{0.57} Sn _{0.1} O ₂ ^[57]	13.4219	6.5686	58.3812	0.4256
P2/O3-Na _{0.67} Ni _{0.33} Mn _{0.47} Sn _{0.2} O ₂ ^[57]	13.0195	6.5686	56.6311	0.2740
P2/O3-Na _{0.67} Ni _{0.33} Mn _{0.37} Sn _{0.3} O ₂ ^[57]	12.6838	6.5686	55.1709	0.1476
P2/O3-Na _{0.67} Fe _{0.45} Mn _{0.45} Mg _{0.10} O ₂ ^[59]	13.1253	6.5686	57.0911	0.3139
P2/O3-Na _{0.67} Fe _{0.425} Mn _{0.425} Mg _{0.15} O ₂ ^[59]	13.1531	6.5686	57.2121	0.3244
P2/O3-Na _{0.67} Fe _{0.40} Mn _{0.40} Mg _{0.20} O ₂ ^[59]	13.1483	6.5686	57.1913	0.3226
P2/O3-Na _{0.67} Li _{0.11} Fe _{0.36} Mn _{0.36} Ti _{0.17} O ₂ ^[60]	13.1132	6.5686	57.0383	0.3093
P2/O3-Na _{0.78} Ni _{0.2} Fe _{0.38} Mn _{0.42} O ₂ ^[108]	14.7661	7.6471	55.1696	0.0673
P2/O3-Na _{0.76} Ni _{0.2} Fe _{0.36} Mn _{0.44} O ₂ ^[108]	14.5385	7.4510	55.7488	0.0286
P2/O3-Na _{0.76} Ni _{0.33} Mn _{0.5} Fe _{0.1} Ti _{0.07} O ₂ ^[49]	14.8717	7.5098	56.5803	0.0996
P2/O3-Na _{0.85} Mn _{0.6} Ni _{0.4} O ₂ ^[64]	16.1662	8.3333	55.4292	0.1758
P2/O3-Na _{0.85} Mn _{0.5} Ni _{0.4} Cu _{0.1} O ₂ ^[64]	16.2627	8.3333	55.7577	0.1394
P2/O3-Na _{0.85} Mn _{0.5} Ni _{0.4} Fe _{0.1} O ₂ ^[64]	16.1031	8.3333	55.2105	0.1995
P2/O3-Na _{0.8} Li _{0.2} Fe _{0.2} Mn _{0.6} O ₂ ^[109]	15.7065	7.8431	57.2169	0.1052
P2-Na _{2/3} Ni _{1/3} Mn _{2/3} O ₂ ^[110]	13.7623	6.5392	60.1312	0.5810
P2-Na _{2/3} Ni _{1/3} Mn _{1/3} Ti _{1/3} O ₂ ^[111]	13.0131	6.5392	56.8576	0.2989
P2-Na _{0.6} (Ti _{0.2} Mn _{0.2} Co _{0.2} Ni _{0.2} Ru _{0.2})O ₂ ^[112]	11.9468	5.8824	58.0270	0.5058
P2-Na _{0.72} Li _{0.24} Mn _{0.76} O ₂ ^[113]	14.9511	7.0588	60.5163	0.5473
P2-Na _{2/3} Mg _{0.28} Mn _{0.72} O ₂ ^[114]	13.5099	6.5392	59.0282	0.4860
P2-Na _{0.7} Li _{0.03} Mg _{0.05} Ni _{0.27} Mn _{0.6} Ti _{0.07} O ₂ ^[115]	14.1631	6.8627	58.9653	0.4323
O3-NaMn _{1/3} Fe _{1/3} Ni _{1/3} O ₂ ^[116]	17.0950	9.8039	49.8197	1.1884
O3-Na _{0.90} Cu _{0.22} Fe _{0.30} Mn _{0.48} O ₂ ^[117]	15.9271	8.8235	51.5736	0.7199
O3-Na _{0.7} Ni _{0.3} Sn _{0.6} O ₂ ^[67]	11.4876	6.8627	47.8260	0.5753
O3-Na _{0.85} RhO ₂ ^[118]	14.1008	8.3333	48.3458	0.9536
O3-NaNi _{1/2} Mn _{1/2} O ₂ ^[119]	17.9215	9.8039	52.2286	0.8771
O3-NaCu _{0.1} Ni _{0.3} Fe _{0.2} Mn _{0.2} Ti _{0.2} O ₂ ^[120]	16.8326	9.8039	49.0552	1.2872

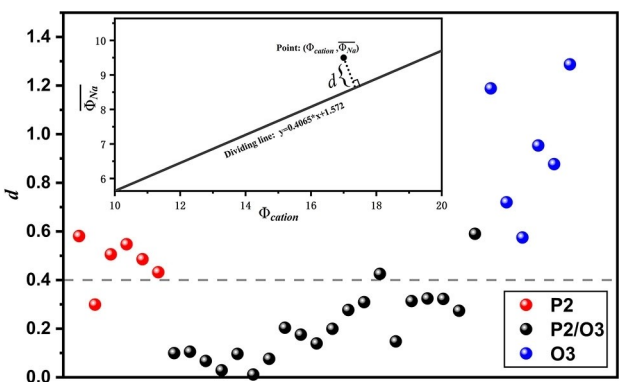


Figure 4. The distance (d) from the $(\Phi_{cation}, \Phi_{Na})$ point to the dividing line of P2 (red balls), P2/O3 (black balls) and O3 phase (blue balls) materials with the inset schematic showing the calculation method for d .

Therefore, the materials with small d (cationic potential close to the dividing line) tend to form P2/O3 composite structure, which provides an idea for the design and phase regulation of P2/O3 composite materials. Furthermore, a recent study also confirms the view.^[103] The study of Ji *et al.* reveals that the formation of P2/O3 composite structure is attributed to the inhomogeneity of cationic potential caused by uneven distribution of elements at the micron scale. For the materials with a cationic potential close to the dividing line, the uneven elements distribution can easily lead to the cationic potential of particles located on both sides of the dividing line, resulting in the formation of P2/O3 composite structure.

However, this trend is not entirely accurate and the d is much larger than 0.4 for some materials, such as P2/O3-Na_{0.85}Ni_{0.34}Mn_{0.33}Ti_{0.33}O₂. This deviation may be due to different synthesis methods. It is important to emphasize that the effect of the synthesis method should be fully considered. Factors such as precursor, method, calcinating temperature and atmosphere can all have a significant impact on the crystal structure. The regulation of calcination temperature and calcination time can generate inhomogeneity and consequently form P2/O3 composite structure.^[103] Another example is that three different crystal structure materials can be prepared by only changing the calcinating temperature and atmosphere. P3/P2/O3-, P3/P2- and P2/O3-type structures are formed under 1000 °C in air, 900 °C in air and 900 °C in oxygen, respectively.^[121] This method of classifying P2/O3 composite structure may also be influenced by other factors. For ion-substituted Na_{0.85}Mn_{0.5}Ni_{0.4}M_{0.1}O₂ (M for one or more transition metal elements), Na_{0.85}Mn_{0.5}Ni_{0.4}Cu_{0.1}O₂ ($d=0.1983$) and Na_{0.85}Mn_{0.5}Ni_{0.4}Fe_{0.1}O₂ ($d=0.2192$) are P2/O3 composite structure while Na_{0.85}Mn_{0.5}Ni_{0.4}Fe_{0.025}Cu_{0.075}O₂ ($d=0.2087$) and Na_{0.85}Mn_{0.5}Ni_{0.4}Fe_{0.05}Cu_{0.05}O₂ ($d=0.2035$) with the same total dopant amount display O3-type structure, which may be attributed to the synergistic effect between the dopants.^[64]

In short, elemental substitution, adjustment of the sodium content and control of the calcination temperature are all key factors in the design and regulation of the composite phase structure. Specifically, for P2/O3 composite structure, this review concludes that cathodes with small d tend to form P2/

O3 composite structure, which provides ideas for the design of P2/O3 composites. However, the effect of temperature on composites lacks clear guidance and can only be predicted in range by drawing on experience. Furthermore, there is a lack of research into the complex relationship between the three factors, and a limited study of one or two of them is inadequate.

3. Electrochemical Performance

3.1. Composite structure of layered oxides

3.1.1. P2/O3 composite structure

The P2/O3 composite structure materials have been widely studied because of the ease of synthesis and excellent properties. Specifically, introduction of Li into alkali layers, regulation of sodium content and TM composition are three common strategies.

Changing the sodium content has a significant effect on the crystal structure.^[105,106] As the sodium content increases, the crystal structure of Na_xNi_{0.20}Fe_{0.40}Mn_{0.40}O₂ changes from a pure P2 phase ($x=0.60$) to a composite structure of P2 and O3 phases ($x=0.74, 0.76$ and 0.78) and eventually becomes a pure O3 phase ($x=0.84$) (Figure 5a).^[105] The results of HRPD and NDP determine that Na_{0.76}Ni_{0.20}Fe_{0.40}Mn_{0.40}O₂ is composed of 18.37 wt % P2-Na_{0.6}[Ni_{0.20}Fe_{0.40}Mn_{0.40}]O₂ and 81.63 wt% O3-Na_{0.84}[Ni_{0.20}Fe_{0.40}Mn_{0.40}]O₂, indicating that the vacancy concentration of the Na ions is not uniform. P2/O3-Na_{0.76}Ni_{0.20}Fe_{0.40}Mn_{0.40}O₂ exhibits an initial discharge capacity of 171.5 mAh g⁻¹ and the capacity retention of 64% after 100 cycles between 1.5–4.5 V at 0.1 C on the basis of Ni²⁺/Ni⁴⁺ and Fe³⁺/Fe⁴⁺ redox couples (Figure 5b), compared to 118.5 mAh g⁻¹ and 78% between 2.0–4.2 V. A series of Na_{0.9-x}Ni_{0.45}Mn_{0.55}O₂ ($x=0.02, 0.04$ and 0.08) with different sodium content were synthesized using the sol-gel method.^[106] Compared to Na_{0.9}Ni_{0.45}Mn_{0.55}O₂ with pure O3 phase, XRD Rietveld refinement result of Na_{0.88}Ni_{0.45}Mn_{0.55}O₂ suggests that the ratio of O3 and P2 phase is 88.4%: 11.6% in the intergrowth structure. Moreover, HRTEM result shows Na_{0.88}Ni_{0.45}Mn_{0.55}O₂ as an intergrowth of the P2 and O3 phases at atomic scale. Compared to O3-Na_{0.9}Ni_{0.45}Mn_{0.55}O₂, O3/P2-Na_{0.88}Ni_{0.45}Mn_{0.55}O₂ delivers a less initial reversible discharge specific capacity (137.2 mAh g⁻¹ vs. 127.7 mAh g⁻¹ between 2–4 V at 7.5 mA g⁻¹). However, O3/P2-Na_{0.88}Ni_{0.45}Mn_{0.55}O₂ exhibits a good capacity retention of 71.1% after 250 cycles at 1 C, which is much better than 38.3% of O3-Na_{0.9}Ni_{0.45}Mn_{0.55}O₂ (Figure 5c). The HRTEM image and FFTs results after 250 cycles show O3/P2-Na_{0.88}Ni_{0.45}Mn_{0.55}O₂ also exhibits a better structural stability.

As for the regulation of TM composition, ion-substitution (such as Ti⁴⁺,^[58] Ni²⁺,^[107] Sn⁴⁺,^[56,57,68] Sb⁵⁺,^[69] Mg²⁺,^[59] Li⁺,^[109,122,123] and Li⁺/Ti⁴⁺,^[60]) is an effective strategy to form P2/O3 composite structure. A series of Ti-substituted Na_{0.85}Ni_{0.34}Mn_{0.66-x}Ti_xO₂ ($x=0, 0.11, 0.22, 0.33, 0.44$) were investigated to illustrate the synergistic effect of biphases.^[58] Among them, composite P2/O3-Na_{0.85}Ni_{0.34}Mn_{0.33}Ti_{0.33}O₂ (the ratio of P2 and O3 phase is

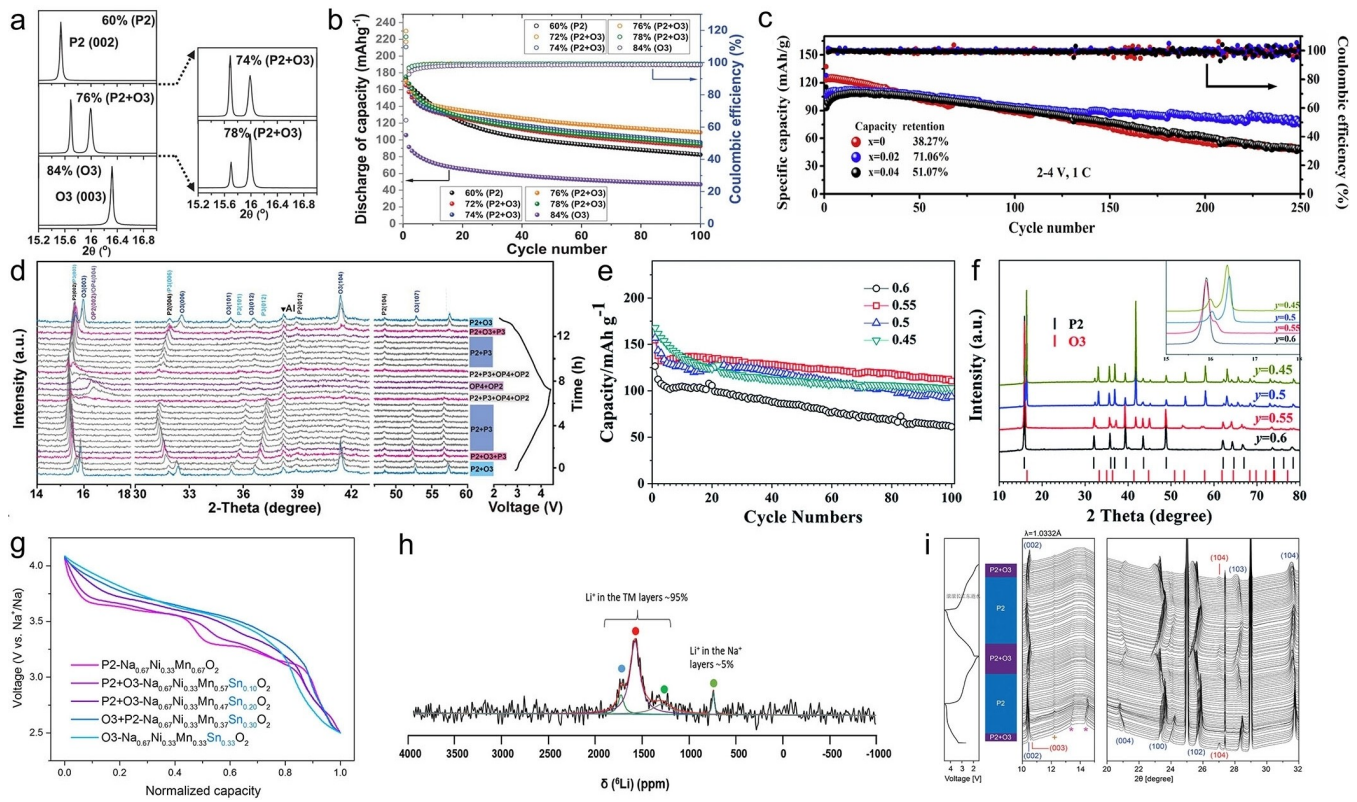


Figure 5. a) HRPD patterns and b) Cycling performance of $\text{Na}_x\text{Ni}_{0.20}\text{Fe}_{0.40}\text{Mn}_{0.40}\text{O}_2$ ($x = 0.6, 0.74, 0.76, 0.78$, and 0.84) materials. a and b) Reproduced with permission from Ref. [105]. Copyright (2022) Wiley-VCH. c) Cycling performance of $\text{Na}_{0.9-x}\text{Ni}_{0.45}\text{Mn}_{0.55}\text{O}_2$ ($x = 0, 0.02$ and 0.04) cycled at 1 C. Reproduced with permission from Ref. [106]. Copyright (2018) Elsevier. d) Operando XRD patterns of $\text{P2}/\text{O3}-\text{Na}_{0.85}\text{Ni}_{0.34}\text{Mn}_{0.33}\text{Ti}_{0.33}\text{O}_2$ at 0.1 C between 2.2 and 4.4 V. Reproduced with permission from Ref. [58]. Copyright (2022) Elsevier. e) Cycling performance of $\text{Na}_{0.8}\text{Mn}_x\text{Ni}_{0.8-x}\text{Fe}_{0.1}\text{Ti}_{0.1}\text{O}_2$ ($y = 0.6, 0.55, 0.5, 0.45$). f) XRD patterns of $\text{Na}_{0.8}\text{Mn}_x\text{Ni}_{0.8-y}\text{Fe}_{0.1}\text{Ti}_{0.1}\text{O}_2$ ($y = 0.6, 0.55, 0.5, 0.45$). Inset: the magnification of 15°–18° representing P2 and O3 phases. e and f) Reproduced with permission from Ref. [107]. Copyright (2021) Royal Society of Chemistry. g) Comparison of normalized discharge profiles of Sn-substituted $\text{Na}_{0.67}\text{Ni}_{0.33}\text{Mn}_{0.67-x}\text{Sn}_x\text{O}_2$ ($x = 0, 0.10, 0.20, 0.30, 0.33$). Reproduced with permission from Ref. [57]. Copyright (2019) Elsevier. h) MAS solid state NMR spectra of ${}^6\text{Li}$ for $\text{Na}_{0.8}\text{Li}_{0.2}\text{Fe}_{0.2}\text{Mn}_{0.6}\text{O}_2$. Reproduced with permission from Ref. [109]. Copyright (2020) Wiley-VCH. i) In situ XRD results and structural evolution of $\text{P2}/\text{O3}-\text{Na}_{0.67}\text{Li}_{0.2}\text{Fe}_{0.2}\text{Mn}_{0.6}\text{O}_2$. Reproduced with permission from Ref. [122]. Copyright (2021) Wiley-VCH.

24.8%: 75.2%) exhibits the best electrochemical properties with a high discharge capacity of 126.6 mAh g^{-1} at 0.1 C and 82.4 mAh g^{-1} at 10 C as well as good capacity retention of 80.6% after 200 cycles at 0.1 C. When assembling full cell with hard carbon, the good electrochemical properties demonstrate its application prospect. $\text{P2}/\text{O3}-\text{Na}_{0.85}\text{Ni}_{0.34}\text{Mn}_{0.33}\text{Ti}_{0.33}\text{O}_2$ undergoes a more complex phase transformation of P2/O3-P2/P3-OP4/OP2 during cycling (Figure 5d) but exhibits better electrochemical properties. The specific reason for this will be discussed in detail in a later chapter. A series of P2/O3 composite structure materials $\text{Na}_{0.8}\text{Mn}_x\text{Ni}_{0.8-x}\text{Fe}_{0.1}\text{Ti}_{0.1}\text{O}_2$ ($x = 0.45, 0.5, 0.55$) were prepared through a solid-state method, where $\text{Na}_{0.8}\text{Mn}_{0.55}\text{Ni}_{0.25}\text{Fe}_{0.1}\text{Ti}_{0.1}\text{O}_2$ displayed the best electrochemical properties (Figure 5e).^[107] Changing x , i.e., the composition of TM is an effective way to change the ratio of P2/O3 (Figure 5f). $\text{P2}-\text{Na}_{0.67}\text{Mn}_{0.55}\text{Ni}_{0.25}\text{Fe}_{0.1}\text{Ti}_{0.1}\text{O}_2$ and $\text{O3}-\text{NaMn}_{0.55}\text{Ni}_{0.25}\text{Fe}_{0.1}\text{Ti}_{0.1}\text{O}_2$ were obtained by varying the sodium content based on $\text{Na}_{0.8}\text{Mn}_{0.55}\text{Ni}_{0.25}\text{Fe}_{0.1}\text{Ti}_{0.1}\text{O}_2$, which also confirms sodium content is one of the essential factors determining the crystal structure. The results of STEM-EELS and EDX spectrum imaging show sodium content in the P2 phase is lower than that in O3 phase causing a difference in sodium

content between the two sides of the interface, which leads to the different transition metal distribution on both sides of the interface to maintain charge conservation. Compared to single-phase $\text{P2}-\text{Na}_{0.67}\text{Mn}_{0.55}\text{Ni}_{0.25}\text{Fe}_{0.1}\text{Ti}_{0.1}\text{O}_2$ and $\text{O3}-\text{NaMn}_{0.55}\text{Ni}_{0.25}\text{Fe}_{0.1}\text{Ti}_{0.1}\text{O}_2$, $\text{P2}/\text{O3}-\text{Na}_{0.8}\text{Mn}_{0.55}\text{Ni}_{0.25}\text{Fe}_{0.1}\text{Ti}_{0.1}\text{O}_2$ achieves a good balance between capacity (153 mAh g^{-1}) and cycling performance (a capacity retention of 80.2% after 100 cycles) at 0.1 C in the voltage range of 1.5–4.3 V (vs. Na/Na⁺). By replacing Mn with Sn in the model material $\text{P2}-\text{Na}_{2/3}\text{Ni}_{1/3}\text{Mn}_{2/3}\text{O}_2$, a P2/O3 composite structure can be obtained.^[56,57,68] From the perspective of cationic potential, Sn⁴⁺ has a larger ionic radius (0.69 Å) compared to Mn⁴⁺ (0.645 Å). Thus, the Sn substitution causes the decrease of cationic potential, favoring the O3-type structure.^[102] Sn-substituted P2/O3-Na_{2/3}Ni_{1/3}Mn_{2/3-x}Sn_xO₂ ($x = 0.05, 0.1, 0.2$) materials exhibit better electrochemical performance than $\text{P2}-\text{Na}_{0.67}\text{Ni}_{0.33}\text{Mn}_{0.67}\text{O}_2$. Among Sn-substituted materials, $\text{P2}/\text{O3}-\text{Na}_{0.67}\text{Ni}_{0.33}\text{Mn}_{0.57}\text{Sn}_{0.1}\text{O}_2$ shows the best performance, where the ratio of P2 and O3 phase is about 1:1 (49.14%:50.86%). $\text{P2}/\text{O3}-\text{Na}_{0.67}\text{Ni}_{0.33}\text{Mn}_{0.57}\text{Sn}_{0.1}\text{O}_2$ exhibits a high discharge capacity of 155.2 mAh g^{-1} at 0.1 C and 99.7 mAh g^{-1} at 1 C, which is perhaps due to the fact that P2/O3 composite structure

favoring the diffusion of sodium ions. The Sn-substitution can smooth the voltage profile (Figure 5g). In addition, the Sn-substitution increases Ni–O bond ionicity^[67,124] and thus increases the working voltage.

Li/Fe/Mn based $\text{Na}_{0.8}\text{Li}_{0.2}\text{Fe}_{0.2}\text{Mn}_{0.6}\text{O}_2$ consists of 34 wt% of the P2 phase and 60% wt% of the O3 phase.^[109] Unlike some other Li-substituted P2/O3 biphasic materials,^[71–76] the O3 phase in P2/O3- $\text{Na}_{0.8}\text{Li}_{0.2}\text{Fe}_{0.2}\text{Mn}_{0.6}\text{O}_2$ is not mainly occupied by Li due to the differences in chemical formula, which can be demonstrated by XRD and NMR. ${}^6\text{Li}$ ssNMR result shows an estimated 95% of total Li content in the TM layers whereas it is only 5% for Li in the alkali layers (Figure 5h). Besides, when charged to 4.6 V, Li^+ at the TM layers has migrated to the alkali layers to compensate for the extraction of Na^+ . However, the spectra discharged to 2.0 V after the first and tenth cycle show the migration of Li from the TM layers to the alkali layers is not reversible. *Ex situ* XRD result shows all peaks can be observed even after 30 cycles, indicating a good reversibility of the phase transition. P2/O3- $\text{Na}_{0.8}\text{Li}_{0.2}\text{Fe}_{0.2}\text{Mn}_{0.6}\text{O}_2$ exhibits an initial capacity of 174 mAh g^{-1} and a capacity retention of 82% at 0.1 C after 100 cycles between 2.0–4.6 V. Similarly, Li/Fe/Mn based P2- $\text{Na}_{0.67}\text{Li}_{0.1}\text{Fe}_{0.225}\text{Mn}_{0.675}\text{O}_2$ and P2/O3- $\text{Na}_{0.67}\text{Li}_{0.2}\text{Fe}_{0.2}\text{Mn}_{0.6}\text{O}_2$ was obtained through Li substitution based on P2-type

$\text{Na}_{0.67}\text{Fe}_{0.25}\text{Mn}_{0.75}\text{O}_2$.^[122] *In situ* XRD result shows that, unlike P2- $\text{Na}_{0.67}\text{Fe}_{0.25}\text{Mn}_{0.75}\text{O}_2$ undergoing the phase transformation of P2-Z at high voltage and P2-P'2 at low voltage, there is no indication of phase transition of P2 phase throughout the charging/discharging process in the P2/O3- $\text{Na}_{0.67}\text{Li}_{0.2}\text{Fe}_{0.2}\text{Mn}_{0.6}\text{O}_2$, indicating good structural reversibility of the biphasic structure (Figure 5i). Excellent structural reversibility and biphasic structure leading to good electrochemical properties, with P2/O3- $\text{Na}_{0.67}\text{Li}_{0.2}\text{Fe}_{0.2}\text{Mn}_{0.6}\text{O}_2$ exhibiting a high discharge capacity of 227 mAh g^{-1} at 10 mA g^{-1} and 73 mAh g^{-1} at 600 mA g^{-1} as well as a remaining capacity of 158.7 mAh g^{-1} after 60 cycles at 10 mA g^{-1} , which is superior to single-phase P2- $\text{Na}_{0.67}\text{Fe}_{0.25}\text{Mn}_{0.75}\text{O}_2$ and P2- $\text{Na}_{0.67}\text{Li}_{0.1}\text{Fe}_{0.225}\text{Mn}_{0.675}\text{O}_2$.

Based on the model material $\text{Na}_{0.67}\text{Fe}_{0.5}\text{Mn}_{0.5}\text{O}_2$, ion-substitution can lead to P2/O3 composite structure. Mg-substitution strategy was used to enhance the electrochemical performance of $\text{Na}_{0.67}\text{Fe}_{0.5}\text{Mn}_{0.5}\text{O}_2$, obtaining $\text{Na}_{0.67}(\text{Fe}_{0.5}\text{Mn}_{0.5})_{1-x}\text{Mg}_x\text{O}_2$ ($x = 0.05, 0.1, 0.15, 0.2, 0.25$).^[59] Among Mg-substituted materials, P2/O3- $\text{Na}_{0.67}\text{Fe}_{0.425}\text{Mn}_{0.425}\text{Mg}_{0.15}\text{O}_2$ exhibits the best electrochemical properties of a discharge capacity of 98.1 mAh g^{-1} at 1 C and a good capacity retention of 87.7% after 100 cycles at 1 C in the voltage range of 1.5–4.2 V (Figure 6a). P2/O3- $\text{Na}_{0.67}\text{Fe}_{0.45}\text{Mn}_{0.45}\text{Mg}_{0.10}\text{O}_2$ has a higher sodium ions diffusion

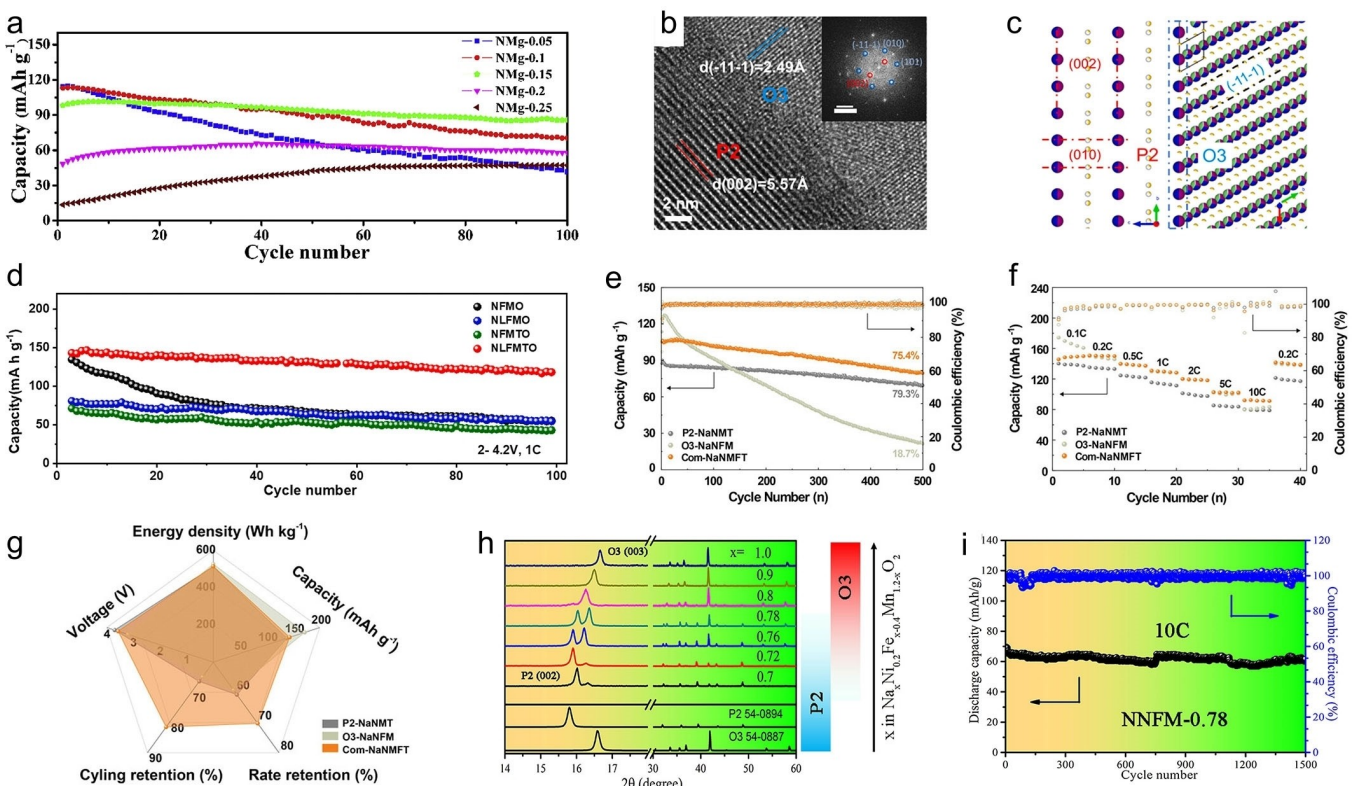


Figure 6. a) Cycling performance of Mg-substituted Fe/Mn-based $\text{Na}_{0.67}(\text{Fe}_{0.5}\text{Mn}_{0.5})_{1-x}\text{Mg}_x\text{O}_2$ ($x = 0.05, 0.1, 0.15, 0.2$). Reproduced with permission from Ref. [59]. Copyright (2019) Elsevier. b) HRTEM image at the phase boundary of $\text{Na}_{0.67}\text{Li}_{0.11}\text{Fe}_{0.36}\text{Mn}_{0.36}\text{Ti}_{0.17}\text{O}_2$. Inset: the corresponding FFT map (scale bar is 5 1/nm). Red and blue circles represent the reflection spots for P2 and O3 phases, respectively. c) Schematic diagram of the unique intersected complex mode in $\text{Na}_{0.67}\text{Li}_{0.11}\text{Fe}_{0.36}\text{Mn}_{0.36}\text{Ti}_{0.17}\text{O}_2$. d) Cycling performance of original $\text{Na}_{0.67}\text{Fe}_{0.5}\text{Mn}_{0.5}\text{O}_2$, Li-substituted, Ti-substituted and Li/Ti co-substituted materials between 2.0 and 4.2 V at 1 C. Reproduced with permission from Ref. [60]. Copyright (2021) Elsevier. e) Cycling performance at 5 C, f) rate performance and g) comparison of electrochemical properties of P2- $\text{Na}_{2/3}\text{Ni}_{1/3}\text{Mn}_{0.57}\text{Ti}_{0.1}\text{O}_2$, O3- $\text{Na}_{1/3}\text{Fe}_{1/3}\text{Mn}_{1/3}\text{O}_2$ and P2/O3- $\text{Na}_{0.766}\text{Ni}_{0.33}\text{Mn}_{0.5}\text{Fe}_{0.1}\text{Ti}_{0.07}\text{O}_2$. Reproduced with permission from Ref. [49]. Copyright (2022) Wiley-VCH. h) XRD patterns of $\text{Na}_x\text{Ni}_{0.2}\text{Fe}_{x-0.4}\text{Mn}_{1.2-x}\text{O}_2$ with different Na contents (0.7–1.0), the phase evolution is shown in the right. i) Cycling performance of $\text{Na}_{0.78}\text{Ni}_{0.2}\text{Fe}_{0.38}\text{Mn}_{0.42}\text{O}_2$ at 10 C. Reproduced with permission from Ref. [108]. Copyright (2017) American Chemical Society.

coefficient than P2-Na_{0.67}Fe_{0.475}Mn_{0.475}Mg_{0.05}O₂, which may be attributed to the interaction of different phases. Through Li/Ti co-substitution, P2/O3-Na_{0.67}Li_{0.11}Fe_{0.36}Mn_{0.36}Ti_{0.17}O₂ exhibits promising electrochemical properties.^[60] HRTEM image result confirms Na_{0.67}Li_{0.11}Fe_{0.36}Mn_{0.36}Ti_{0.17}O₂ as a P2/O3 composite structure (Figure 6b). Interestingly, (002) plane of P2 phase intersects with (−11−1) plane of O3 phase at an angle, forming a special P2/O3 intergrowth mode (Figure 6c). Due to oxygen redox reaction, Li/Ti co-substituted material shows extremely high initial capacity of 235 mAh g^{−1} at 0.1 C and 172 mAh g^{−1} at 1 C in the voltage range of 1.5–4.2 V, which is much higher than P2-Na_{0.67}Fe_{0.5}Mn_{0.5}O₂ (183 mAh g^{−1} at 0.1 C and 140 mAh g^{−1} at 1 C). When cycled in 2.0–4.2 V at 1 C, P2/O3-Na_{0.67}Li_{0.11}Fe_{0.36}Mn_{0.36}Ti_{0.17}O₂ exhibits an initial discharge capacity of ~150 mAh g^{−1} as well as good capacity retention of 85.4% after 100 cycles (Figure 6d), much better than 40.9% of P2-Na_{0.67}Fe_{0.5}Mn_{0.5}O₂. Moreover, *ex situ* XRD results illustrate the phase transition of P2-OP4 is partly restrained in Li/Ti co-substituted material. By using HRTEM, massive intragranular micro-cracks can be observed in P2-Na_{0.67}Fe_{0.5}Mn_{0.5}O₂ after 100 cycles, which are not observed in P2/O3-Na_{0.67}Li_{0.11}Fe_{0.36}Mn_{0.36}Ti_{0.17}O₂. The results of X-ray fluorescence (XRF) indicate the dissolution of Mn is severe in P2-Na_{0.67}Fe_{0.5}Mn_{0.5}O₂ after 100 cycles, but is alleviated in P2/O3-Na_{0.67}Li_{0.11}Fe_{0.36}Mn_{0.36}Ti_{0.17}O₂. All of the results illustrate the interaction of P2 and O3 phases, which enhances the reversibility of the phase transformation and cycling stability. The electrochemical properties of the original material Na_{2/3}Fe_{1/2}Mn_{1/2}O₂ and ion-substituted P2/O3 composite materials are summarized in the Table 2. The comparison shows that P2/O3-Na_{0.67}Fe_{0.425}Mn_{0.425}Mg_{0.15}O₂ and P2/O3-Na_{0.67}Li_{0.11}Fe_{0.36}Mn_{0.36}Ti_{0.17}O₂ display better performance compared to Na_{2/3}Fe_{1/2}Mn_{1/2}O₂, which presents a viable strategy for the practical application of Fe/Mn based layered oxides.

Some studies used both strategies, varying sodium content and TM composition.^[49,64,108] Based on P2-Na_{2/3}Ni_{1/3}Mn_{0.57}Ti_{0.1}O₂ and O3-NaNi_{1/3}Fe_{1/3}Mn_{1/3}O₂, a rational biphasic tailoring strategy was proposed for the design of P2/O3 composite structure.^[49] 77 compounds were synthesized by changing sodium content (x in (100− x)% P2-Na_{2/3}Ni_{1/3}Mn_{0.57}Ti_{0.1}O₂+ x % O3-NaNi_{1/3}Fe_{1/3}Mn_{1/3}O₂) and calcination temperature. The ratio of P2 phase and O3 phase in the Na_{0.766}Ni_{0.33}Mn_{0.5}Fe_{0.1}Ti_{0.07}O₂ prepared at 950 °C is

58.91 wt% : 41.09 wt%. P2/O3-Na_{0.766}Ni_{0.33}Mn_{0.5}Fe_{0.1}Ti_{0.07}O₂ exhibits a high discharge capacity of 144 mAh g^{−1} at 0.2 C (achieving an energy density of 514 Wh kg^{−1}) and 92 mAh g^{−1} at 10 C as well as good capacity retention after 500 cycles at 5 C (Figure 6e and f). As summarized in Figure 6(g), compared to single-phase P2-Na_{2/3}Ni_{1/3}Mn_{0.57}Ti_{0.1}O₂ and O3-NaNi_{1/3}Fe_{1/3}Mn_{1/3}O₂, P2/O3-Na_{0.766}Ni_{0.33}Mn_{0.5}Fe_{0.1}Ti_{0.07}O₂ demonstrates superior overall electrochemical properties. The results of *in situ* XRD indicate that P2/O3-Na_{0.766}Ni_{0.33}Mn_{0.5}Fe_{0.1}Ti_{0.07}O₂ undergoes the complex phase transformation of P2/O3-P2/P3-Z/O3'−P2/P3-P2/O3 during the charge and discharge process. A biphasic clamping reaction mechanism was proposed to explain why composite structure exhibits better cycling performance, which will be discussed in more detail in a later chapter. The crystal structures of Na_xMn_yNi_{1−y}O₂ (0.66 ≤ x ≤ 1, 0 ≤ y ≤ 1) with different sodium content and TM composition were studied.^[64] P2/O3 composite structure appears in the case of Na_xMn_{0.6}Ni_{0.4}O₂ (0.75 < x < 0.95) and Na_{0.85}Mn_{0.5}Ni_{0.5}O₂. Based on the model material P2/O3-Na_{0.85}Mn_{0.6}Ni_{0.4}O₂, Na_{0.85}Mn_{0.5}Ni_{0.4}M_{0.1}O₂ was obtained by replacing Mn with M (M=Ni, Fe, Ti, Cu, Co, etc.). The substitution of M for Mn results in a change in the ratio of P2:O3, which means P2/O3 composite structure can be regulated by changing the composition of the transition metals. Compared to model material P2/O3-Na_{0.85}Mn_{0.6}Ni_{0.4}O₂, Na_{0.85}Mn_{0.5}Ni_{0.4}M_{0.1}O₂ (M=Fe, Ti, Cu) shows better reversibility and better rate capability. Ni/Fe/Mn based Na_x[Ni_{0.2}Fe_{x−0.4}Mn_{1.2−x}]O₂ (0.7 ≤ x ≤ 1.0) were synthesized through solid-state reaction,^[108] which can be seen as a combination of (100− y)% mainly P2-Na_{0.7}Ni_{0.2}Fe_{0.3}Mn_{0.5}O₂+ y % O3-NaNi_{0.2}Fe_{0.6}Mn_{0.2}O₂. Similarly, a P2/O3 composite phase is formed when the sodium content is in the middle (0.7 ≤ x ≤ 0.8) (Figure 6h). Na_{0.78}Ni_{0.2}Fe_{0.38}Mn_{0.42}O₂ displays a capacity of 86 mAh g^{−1} at 0.1 C and 57 mAh g^{−1} at 10 C as well as excellent capacity retention of 90% after 1500 cycles at 10 C between 2.5–4.0 V (Figure 6i). *In situ* XRD indicates that P2/O3-Na_{0.78}Ni_{0.2}Fe_{0.38}Mn_{0.42}O₂ undergoes a more severe phase transformation when the cut-off voltage is increased from 4.0 V to 4.3 V, indicating that 2.5–4.0 V is more suitable for cycling.

The introduction of Li into alkali layers leading to the Li−O₃ or Li−O'3 phases is another effective method to obtain P2/O3 composite structure materials.^[70–77] It should be noted that the added Li ions are located at both TM layers and alkali layers

Table 2. A summary of the electrochemical properties of original material Na_{2/3}Fe_{1/2}Mn_{1/2}O₂ and ion-substituted P2/O3 composite materials.

Material	Phase	Specific capacity [mAh g ^{−1}]	Rate performance [mAh g ^{−1}]	Capacity retention
Na _{2/3} Fe _{1/2} Mn _{1/2} O ₂ ^[125]	P2	114 (0.1 C 2.0–4.0 V)	~70 (1 C 2.0–4.0 V)	82.02% (2.0–4.0 V at 0.1 C, 25 cycles)
Na _{2/3} Fe _{1/2} Mn _{1/2} O ₂ ^[125]	O3	126 (0.1 C 2.0–4.0 V)	~70 (1 C 2.0–4.0 V)	84.74% (2.0–4.0 V at 0.1 C, 25 cycles)
Na _{2/3} Fe _{1/2} Mn _{1/2} O ₂ ^[126]	P2	~175 (0.1 C 1.5–4.2 V)	~130 (1 C 1.5–4.2 V)	~79% (1.5–4.2 V at 0.1 C, 30 cycles)
Na _{2/3} Fe _{1/2} Mn _{1/2} O ₂ ^[127]	P2	~195 (0.1 C 1.5–4.2 V)	~140 (1 C 1.5–4.2 V)	86.4% (1.5–4.2 V at 0.1 C, 80 cycles)
Na _{0.67} Fe _{0.5} Mn _{0.5} O ₂ ^[60]	P2	183 (0.1 C 1.5–4.2 V)	140 (1 C 1.5–4.2 V)	40.9% (2.0–4.2 V at 1 C, 100 cycles)
Na _{0.67} Fe _{0.475} Mn _{0.475} Mg _{0.05} O ₂ ^[59]	P2	169.7 (0.1 C 1.5–4.2 V)	114.4 (1 C 1.5–4.2 V)	36.7% (1.5–4.2 V at 1 C, 100 cycles)
Na _{0.67} Fe _{0.45} Mn _{0.45} Mg _{0.10} O ₂ ^[59]	P2/O3	168.4 (0.1 C 1.5–4.2 V)	113.1 (1 C 1.5–4.2 V)	62.4% (1.5–4.2 V at 1 C, 100 cycles)
Na _{0.67} Fe _{0.425} Mn _{0.425} Mg _{0.15} O ₂ ^[59]	P2/O3	146.6 (0.1 C 1.5–4.2 V)	98.1 (1 C 1.5–4.2 V)	87.7% (1.5–4.2 V at 1 C, 100 cycles)
Na _{0.67} Fe _{0.4} Mn _{0.4} Mg _{0.20} O ₂ ^[59]	P2/O3	125.8 (0.1 C 1.5–4.2 V)	48.3 (1 C 1.5–4.2 V)	–
Na _{0.67} Fe _{0.375} Mn _{0.375} Mg _{0.25} O ₂ ^[59]	O3	113.7 (0.1 C 1.5–4.2 V)	13.5 (1 C 1.5–4.2 V)	–
Na _{0.67} Li _{0.11} Fe _{0.36} Mn _{0.36} Ti _{0.17} O ₂ ^[60]	P2/O3	235 (0.1 C 1.5–4.2 V)	172 (1 C 1.5–4.2 V)	85.4% (2.0–4.2 V at 1 C, 100 cycles)
Na _{0.67} Li _{0.11} Fe _{0.445} Mn _{0.445} O ₂ ^[60]	mainly O3	136 (0.1 C 1.5–4.2 V)	–	71% (2.0–4.2 V at 1 C, 100 cycles)
Na _{0.67} Fe _{0.415} Mn _{0.415} Ti _{0.17} O ₂	mainly P2	125 (0.1 C 1.5–4.2 V)	–	63.4% (2.0–4.2 V at 1 C, 100 cycles)

forming $\text{Na}_x\text{Li}_{y-z}[\text{Li}_z\text{TM}]O_{2+\delta}$. When the Li content is relatively high, the distribution of Li in the alkali or TM layers is not exact. In Li-substituted $\text{Na}_{1-x}\text{Li}_x\text{Ni}_{0.5}\text{Mn}_{0.5}\text{O}_{2+\delta}$, the proportions of Na–O₃, Na–P₂, and Li–O₃ phases vary with increasing lithium content. (Figure 7a).^[70] Similarly, an Li-supersaturating strategy was applied for P2-Na_{0.67}Ni_{0.33}Mn_{0.67}O₂ and successfully inhibited Na⁺/vacancy ordering and P2–O₂ phase transition.^[76] The results of HAADF-STEM, EDS and EELS demonstrate the intergrowth of the P2 and O₃ phases. In addition, the Na element disappears in the region of the O₃ phase, where most of the Li element is mainly distributed. This indicates that the distribution of elements in P2 and O₃ phases is uneven. EXAFS result shows the intensity of Mn-TM and Ni-TM peaks in P2/O₃-Na_{0.67}Li_{0.16}Mn_{0.67}Ni_{0.33}O_{2+\delta} is lower than that in P2-Na_{0.67}Ni_{0.33}Mn_{0.67}O₂ (Figure 7b and c), indicating that part of the Li is located at the TM layers, which may lead to Na⁺/vacancy disordering. P2/O₃-Na_{0.67}Li_{0.16}Mn_{0.67}Ni_{0.33}O_{2+\delta} exhibits a high discharge capacity of 145 mAh g⁻¹ at 0.1 C between 2.0–4.5 V. Li-substituted material also displays a good rate performance (104 mAh g⁻¹ at 5 C) and cycling performance (70.2% capacity retention after 200 cycles at 0.5 C). Unlike P2/O₃-Na_{0.66}Li_{0.18}Mn_{0.71}Ni_{0.21}Co_{0.08}O_{2+\delta} investigated by Zhou *et al.*^[71] and other Li-substituted P2/O₃ biphasic materials^[70,76] (O₃ represents space group: R₃m), Wei *et al.* prepared Na–P2/Li–O₃ Na_xLi_{0.18}Mn_{0.66}Ni_{0.17}Co_{0.17}O_{2+\delta} with different sodium content ($x=0.54$, 0.66, 0.78, and 0.90), where the O₃ represents space group: C₂/m.^[73] The results of HAADF-STEM image and EDS mapping show Mn elements are located in both the bright regions of Na–P2 and the dark regions of Li–O₃ while Na, Ni, and Co are primarily located in the bright regions. Among the materials with different sodium content, Na_{0.66}Li_{0.18}Mn_{0.66}Ni_{0.17}Co_{0.17}O_{2+\delta} exhibits the best electrochemical properties of a discharge capacity of 187.1 mAh g⁻¹ at 0.1 C and

114 mAh g⁻¹ at 5 C between 1.5 and 4.5 V. After 60 cycles at 0.2 C, Na_{0.66}Li_{0.18}Mn_{0.66}Ni_{0.17}Co_{0.17}O_{2+\delta} still has a high discharge capacity of 186.2 mAh g⁻¹. Wei *et al.* put forward a hypothesis that the increased thickness favors the preferential growth of (102) and (104) facets, causing better electrochemical performance. However, as the sodium content increases, clean and smooth side surfaces ($x=0.66$) gradually become uneven and ravine-like ($x=0.78, 0.90$), which is detrimental to rate performance (Figure 7d). A detailed study of P2/O₃-Na_{2/3}Li_{0.18}Mn_{0.8}Fe_{0.2}O₂ was carried out by Teófilo Rojo and co-workers.^[72,74] ⁷Li solid-state NMR analysis shows two narrow peaks at 750 and 1500 ppm and a broader one at about 1800 ppm, which present Li⁺ at P2 alkali layers, Li⁺ at O₃ alkali layers, Li⁺ at the TM layers, respectively (Figure 7e).^[72] Neutron diffraction result indicates that the alkali metal site of O₃ phase is completely occupied by Li while that of P2 phase consists of both Na and Li.^[74] The above results illustrate that Li occupies both the P2 and O₃ phases. P2/O₃-Na_{2/3}Li_{0.18}Mn_{0.8}Fe_{0.2}O₂ exhibits an initial discharge capacity of 125 mAh g⁻¹ at 0.1 C and 105 mAh g⁻¹ at 1 C between 1.5 and 4.2 V. After 100 cycles at 0.1 C, P2/O₃-Na_{2/3}Li_{0.18}Mn_{0.8}Fe_{0.2}O₂ has a capacity retention of 69.6%.

Special attention needs to be paid to the formation of the Li–O₃ phase. Wei *et al.* studied the Li–O₃/O₃ phase in Li-substituted P2/O₃-Na_{0.67}Li_{0.16}Mn_{0.67}Ni_{0.33}O_{2+\delta}^[76] (Figure 7f), P2/O₃-Na_{0.78}Li_{0.18}Mn_{0.66}Co_{0.17}Ni_{0.17}O_{2+\delta}^[73] (Figure 7g) and P3/O₃-Na_{0.57}Li_{0.17}Mn_{0.67}Ni_{0.16}Co_{0.17}O₂^[78] (Figure 7h). The results of HAADF-STEM demonstrate the intergrowth of the P2 and O₃ phases. The composite structure exhibits alternatively arranged bright regions of Na–P2 phase and the dark regions of Li–O₃ (or Li–O₃). Moreover, the results of EDS maps show the Na element disappears in the dark region. The results of EELS show the difference at 60 eV of Li K-edge peak, which

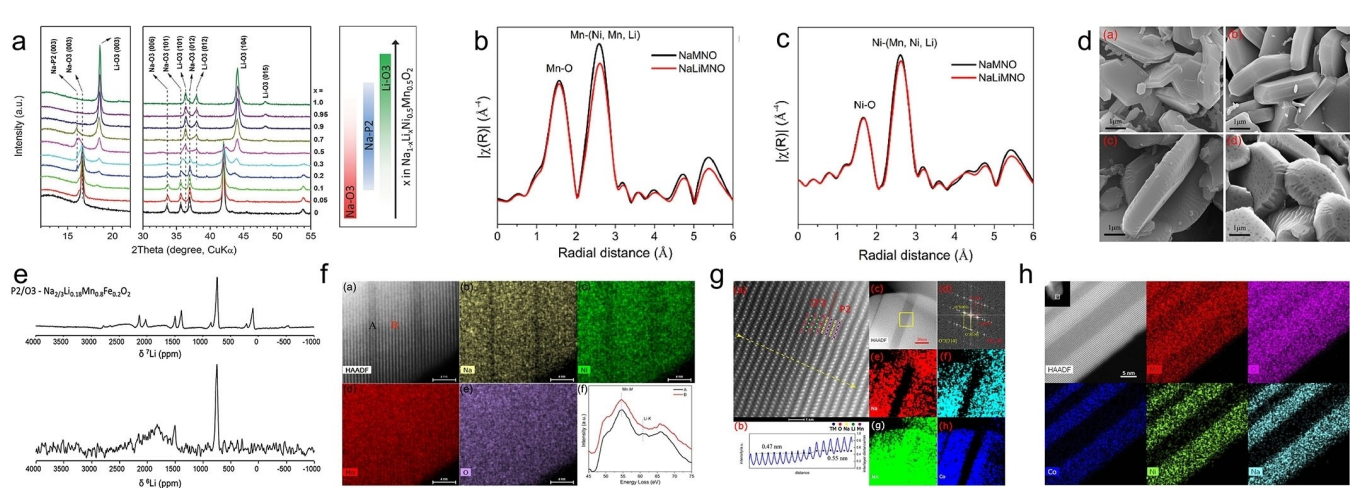


Figure 7. a) XRD patterns of $\text{Na}_{1-x}\text{Li}_x\text{Ni}_{0.5}\text{Mn}_{0.5}\text{O}_{2+\delta}$ with different Li content x ($0 \leq x \leq 1$), the major phases evolution is shown in the right. Reproduced with permission from Ref. [70]. Copyright (2014) Wiley-VCH. Fourier transformation of EXAFS spectra of two different samples at the b) Mn K-edge and c) Ni K-edge. Reproduced with permission from Ref. [76]. Copyright (2021) Elsevier. d) SEM images of $\text{Na}_x\text{Li}_{0.18}\text{Mn}_{0.66}\text{Co}_{0.17}\text{Ni}_{0.17}\text{O}_{2+\delta}$ with different Na content ($x=0.54$: upper left, 0.66: upper right, 0.78: lower left and 0.90: lower right). Reproduced with permission from Ref. [73]. Copyright (2020) American Chemical Society. e) ⁶Li and ⁷Li NMR spectra of the SS sample. Reproduced with permission from Ref. [72]. Copyright (2018) Royal Society of Chemistry. HAADF-STEM image, FFT pattern, EDS mapping and EELS result of f) P2/O₃-Na_{0.67}Li_{0.16}Mn_{0.67}Ni_{0.33}O_{2+\delta}, g) P2/O₃-Na_{0.78}Li_{0.18}Mn_{0.66}Co_{0.17}Ni_{0.17}O_{2+\delta} and h) P3/O₃-Na_{0.57}Li_{0.17}Mn_{0.67}Ni_{0.16}Co_{0.17}O₂. Reproduced with permission from Ref. [76]. Copyright (2021) Elsevier. Reproduced with permission from Ref. [73]. Copyright (2020) American Chemical Society. Reproduced with permission from Ref. [78]. Copyright (2017) Elsevier.

represents that most of the Li element is mainly distributed in the bright region. The studies of Teófilo Rojo and coworkers also indicate the alkali metal site of O₃ phase is fully occupied by Li.^[72,74] Therefore, the distribution of elements in P2 and O₃ phases is uneven and the alkali layers of O₃ or O'3 phase is occupied by Li.

3.1.2. P2/P3 composite structure

As reported, the interaction between P2 and P3 structure can provide a clamping force for the composite phase structure in the opposite direction to the phase transition. Therefore, a great deal of research has been devoted to the exploration of the P2/P3 composite phase to try to combine the advantages and compensate disadvantages of P2 and P3 single phases. In general, P3 phase can be obtained by lowering the calcination temperature and transition metal substitution of P2 materials,^[132] which are also the main strategies to synthesis P2/P3 composite phase.

Passerini and co-workers presented that the P2/P3-Na_{0.46}Ni_{0.22}Co_{0.11}Mn_{0.66}O₂ could be obtained by adjusting the calcination temperature for the first time.^[81] As the calcination temperature increases, the crystal structure of Na_{0.46}Ni_{0.22}Co_{0.11}Mn_{0.66}O₂ changes from P3-type structure (700 °C) to P2/P3 composite structure (750 °C) and eventually to P2-type structure (800–900 °C). Although the electrochemical properties of the P2/P3 composite phase materials obtained in this work are not as good as those of the pure P2 phase materials obtained by calcining at 800 °C and 900 °C, it does provide a strategy for obtaining P2/P3 composite phase materials by controlling the calcination temperature around 750 °C. Since a water treatment was implemented on the material to dissolve the inactive Na₂CO₃ impurities from the surface of the material during the preparation process, the water sensitivity of the P2/P3 composite phase material was further investigated by XRD and found that the effect of water on the material was related to the Na content in the material.^[79] In subsequent work, when exploring the effect of calcination temperature on the structure of the material, P2/P3-Na_{0.6}Ni_{0.22}Fe_{0.11}Mn_{0.66}O₂ was prepared at an calcination temperature of 850 °C.^[104] Na_{0.6}Ni_{0.22}Fe_{0.11}Mn_{0.66}O₂ was prepared at the calcination temperatures of 900 °C (pure P2), 850 °C (P2/P3 composite), and 800 °C (pure P3), respectively. It was indicated that the temperature at which the P2/P3 composite phase is generated is material dependent, with different binding energies of the material leading to different temperatures for the formation of the composite phase, but it is certain that the temperatures at which the P2/P3 composite phase is generated is between that of the pure P2 and pure P3 phases. P2/P3-Na_{0.6}Ni_{0.22}Fe_{0.11}Mn_{0.66}O₂ cathode delivers a specific capacity of 216 mAh g⁻¹ at 15 mA g⁻¹ within the 1.5–4.6 V voltage range and a capacity retention of 60% after 30 cycles (Figure 8a), which is not comparable to the pure P2 and pure P3 materials of the same composition. Moreover, there was more obvious manganese dissolution in combination with the NaPF₆ electrolyte than with the pure P2 and pure P3 materials,^[133] indicating that the right material and the right

electrolyte must be developed to obtain the performance advantage of the P2/P3 composite phase material. Another example is P2/P3-Na_{0.66}Co_{0.5}Mn_{0.5}O₂ prepared by a sol-gel method and subsequent calcination at 800 °C,^[134] with 23.95 wt % of the P2 phase structure and 76.05 wt% of the P3 phase structure. Similarly, P3-type Na_{0.66}Co_{0.5}Mn_{0.5}O₂ was prepared at a lower calcination temperature of 700 °C, reflecting the important role of temperature on the formation of P2/P3 composite structure. By *ex situ* XRD analysis of the Na⁺ insertion/extraction processes, it was found that the diffraction peaks of the P2/P3-Na_{0.66}Co_{0.5}Mn_{0.5}O₂ cathode only slightly shifted a little angle and reversibly returned to their original positions, indicating that the cathode material is structurally stable during the charging and discharging process. Taking advantage of the excellent structural stability of the material, the Na_{0.66}Co_{0.5}Mn_{0.5}O₂ electrode delivers the discharge capacity of 156.1 mAh g⁻¹ at 1 C between 1.5 and 4.3 V, and displays good rate and cycling performance (78.9 mAh g⁻¹ at 10 C and 91% after 100 cycles at 10 C). In particular, the electrochemical performance of the P2/P3-Na_{0.66}Co_{0.5}Mn_{0.5}O₂ was greatly improved compared to pure P3-Na_{0.66}Co_{0.5}Mn_{0.5}O₂, in contrast to the work done by Passerini.^[104] Guo and co-workers presented a P2/P3-Na_{0.7}Li_{0.06}Mg_{0.06}Ni_{0.22}Mn_{0.67}O₂ (P2/P3-NLMNM) biphasic cathode,^[101] which delivers a specific capacity of 119 mAh g⁻¹, an operating voltage of 3.53 V, great cycling performance (82.2% after 50 cycles) as well as remarkable rate performance (85.5% at 5 C compared to 0.2 C). When P2/P3-NLMNM is matched to hard carbon, the energy density of the full cell is 218 Wh kg⁻¹, making it a promising cathode for commercial sodium ion batteries. Through *in situ* XRD of the charge/discharge process of P2/P3-NLMNM (Figure 8b), the reason for the high structural stability of the material can be obtained. The P3 structure remains generally stable during the charge/discharge process and provides a clamping effect on the P2 structure, which is susceptible to P2-O₂ and P2-OP4 phase transitions, making complex phase transitions in the P2 phase less likely to be realized, thus offering the ability to stabilize the structure and improve cycling performance.

In addition to changing the calcination temperature, ion substitution is also an effective strategy to adjust the proportion of phases in the P2/P3 composite structural materials. Using Sn⁴⁺ substitution for Mn⁴⁺ in P2-Na_{0.6}Ni_{0.33}Mn_{0.67}O₂ increases the proportion of the P3 phase in the material at a controlled calcination temperature of 800 °C.^[62] The best performance of P2/P3-Na_{0.67}Ni_{0.33}Mn_{0.66}Sn_xO₂ was obtained when x=0.01 (Figure 8c), which has a ratio of P2:P3 of 0.257:0.743 and delivers an initial charge capacity of 166 mAh g⁻¹ and a high discharge capacity of 245 mAh g⁻¹. It was indicated that the cycling performance of P2/P3-Na_{0.67}Ni_{0.33}Mn_{0.66}Sn_{0.01}O₂ was slightly weaker than that of P2-Na_{0.6}Ni_{0.33}Mn_{0.67}O₂, probably due to the enhanced oxygen redox activity, which has a lower reversibility and slower kinetic performance.^[135,136] In addition to Sn substitution, the effect of Co substitution on crystal structure was also investigated. P2/P3-Na_{0.67}Mn_{0.64}Co_{0.30}Al_{0.06}O₂ delivers an outstanding rate performance (83 mAh g⁻¹ at a 1700 mA g⁻¹) and a remarkable cycling performance after 200 cycles at 1000 mA g⁻¹ (Fig-

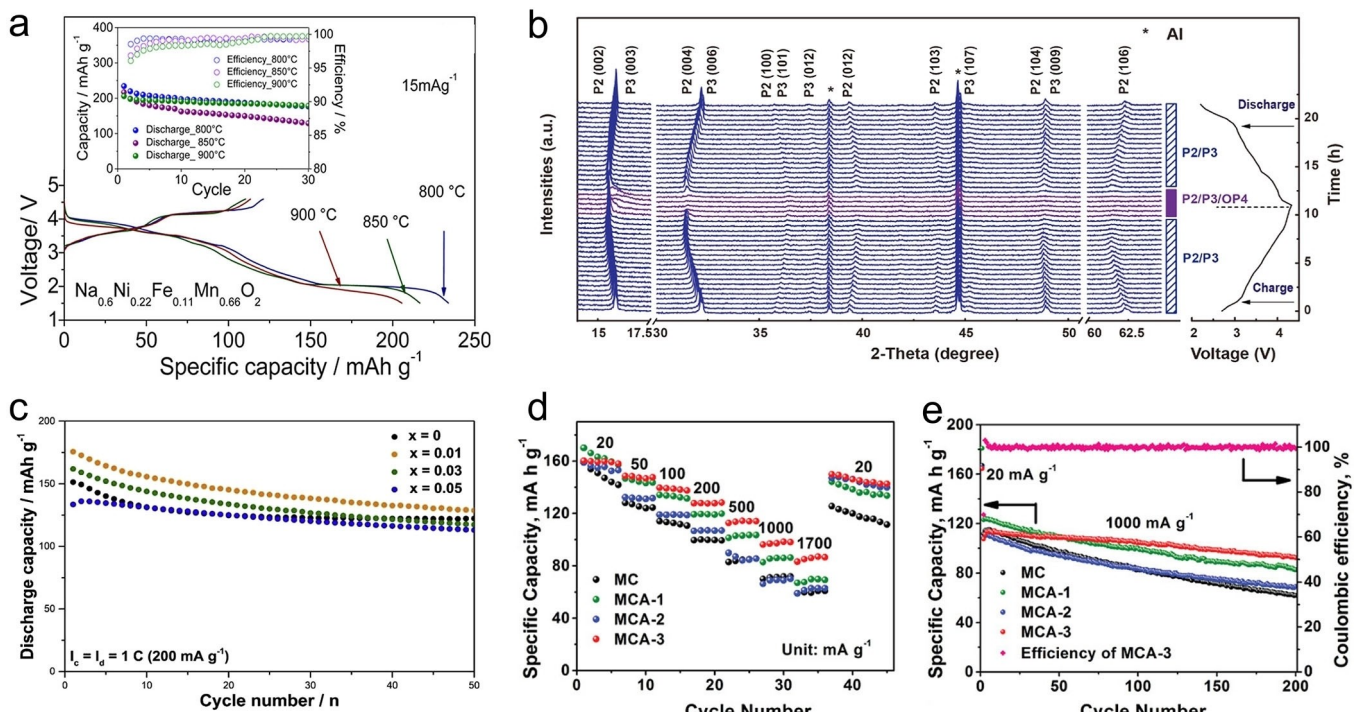


Figure 8. a) Comparison of the first charge/discharge curve of $\text{Na}_{0.6}\text{Ni}_{0.22}\text{Fe}_{0.11}\text{Mn}_{0.66}\text{O}_2$ material prepared at 900, 850, and 800 °C. Inset: comparison of cycling performance. Reproduced with permission from Ref. [104]. Copyright (2015) American Chemical Society. b) *In situ* XRD patterns collected during the 1st cycle of P2/P3- $\text{Na}_0.7\text{Li}_{0.06}\text{Mg}_{0.22}\text{Mn}_{0.67}\text{O}_2$ at 0.1 C with sampling interval of 30 min. Reproduced with permission from Ref. [101]. Copyright (2018) Elsevier. c) Cycling performance of $\text{Na}_{0.67}\text{Ni}_{0.33}\text{Mn}_{0.67-x}\text{Sn}_x\text{O}_2$ ($x = 0, 0.01, 0.03, 0.05$) between 1.5 and 4.5 V. Reproduced with permission from Ref. [62]. Copyright (2019) Elsevier. d) Rate performance of $\text{Na}_{0.67}\text{Mn}_{0.69}\text{Co}_{0.31}\text{O}_2$ (MC), P2- $\text{Na}_{0.67}\text{Mn}_{0.84}\text{Co}_{0.10}\text{Al}_{0.06}\text{O}_2$ (MCA-1), P2/P3- $\text{Na}_{0.67}\text{Mn}_{0.72}\text{Co}_{0.20}\text{Al}_{0.08}\text{O}_2$ (MCA-2), and P2/P3- $\text{Na}_{0.67}\text{Mn}_{0.64}\text{Co}_{0.30}\text{Al}_{0.06}\text{O}_2$ (MCA-3) at various current densities. e) Cycling performance of MC, MCA-1, MCA-2, and MCA-3 over 200 cycles at 1000 mAh g⁻¹ between 1.5 and 4 V. The activation at 20 mA g⁻¹ for the first cycle was applied before the cyclic measurement. Reproduced with permission from Ref. [83]. Copyright (2021) Wiley-VCH.

ure 8d,e).^[83] The results of operando XRD shows that the P2-P2' phase transition is greatly restrained, indicating enhanced cyclic stability of the material.

3.1.3. P3/O3 Composite Structure

Unlike the P2/O3 and P2/P3 composite structure, the P3/O3 composite structure is less well studied. However, the introduction of Li into alkali layers and elemental substitution are still effective methods. Ti-substituted materials $\text{Na}_{2/3}\text{Ni}_{1/3}\text{Mn}_{2/3-x}\text{Ti}_x\text{O}_2$ ($x = 0, 1/6, 1/3, 2/3$) were prepared by using a sol-gel method.^[128] As Ti substitution increases, the crystal structure of $\text{Na}_{2/3}\text{Ni}_{1/3}\text{Mn}_{2/3-x}\text{Ti}_x\text{O}_2$ changes from P3-type structure ($x = 0, 1/6$) to P3/O3 composite structure ($x = 1/3$) and eventually to O3-type structure ($x = 2/3$) (Figure 9a). The Rietveld refinement result shows $\text{Na}_{2/3}\text{Ni}_{1/3}\text{Mn}_{1/3}\text{Ti}_{1/3}\text{O}_2$ is composed of 70.93% P3 phase and 29.07% O3 phase. The DFT calculation result confirms that the thermodynamic energy of O3-type $\text{Na}_{2/3}\text{Ni}_{1/3}\text{Mn}_{1/3}\text{Ti}_{1/3}\text{O}_2$ is similar to that of P3-type $\text{Na}_{2/3}\text{Ni}_{1/3}\text{Mn}_{1/3}\text{Ti}_{1/3}\text{O}_2$, leading to P3/O3 composite structure in $\text{Na}_{2/3}\text{Ni}_{1/3}\text{Mn}_{1/3}\text{Ti}_{1/3}\text{O}_2$. P3/O3- $\text{Na}_{2/3}\text{Ni}_{1/3}\text{Mn}_{1/3}\text{Ti}_{1/3}\text{O}_2$ exhibits a high rate capability up to 88.7% of the capacity at 0.1 C, better than those of single-phase materials P3- $\text{Na}_{2/3}\text{Ni}_{1/3}\text{Mn}_{2/3}\text{O}_2$ (80%) and P3- $\text{Na}_{2/3}\text{Ni}_{1/3}\text{Mn}_{1/2}\text{Ti}_{1/6}\text{O}_2$ (86%). As for cycling performance, P3/O3- $\text{Na}_{2/3}\text{Ni}_{1/3}\text{Mn}_{1/3}\text{Ti}_{1/3}\text{O}_2$

exhibits a capacity retention of 78% after 1000 cycles at 1 C between 2.5 V–4.15 V, which is much better than P3- $\text{Na}_{2/3}\text{Ni}_{1/3}\text{Mn}_{2/3}\text{O}_2$ and O3- $\text{Na}_{2/3}\text{Ni}_{1/3}\text{Ti}_{2/3}\text{O}_2$ (Figure 9b). As mentioned before^[73], Li-substitution can lead to Li-O'3 phase. Differently, the calcination temperature for the synthesis of $\text{Na}_{0.57}\text{Li}_x\text{Mn}_{0.67}\text{Ni}_{0.16}\text{Co}_{0.17}\text{O}_2$ is a relatively low 700 °C, leading to the formation of the P3/O3 composite structure.^[78] Similarly, the distribution of elements in different phases of the composite structure is uneven. However, evident sodium signal appears in the O'3 phase after one cycle, indicating the possibility of Li extraction from and Na insertion into the Li-O'3 phase. The HAADF-STEM images show the cracking and surface corrosion in the P3- $\text{Na}_{0.57}\text{Mn}_{0.67}\text{Ni}_{0.16}\text{Co}_{0.17}\text{O}_2$ after 50 cycles while the structure of P3/O'3- $\text{Na}_{0.57}\text{Li}_{0.17}\text{Mn}_{0.67}\text{Ni}_{0.16}\text{Co}_{0.17}\text{O}_2$ is well retained. P3/O'3- $\text{Na}_{0.57}\text{Li}_{0.17}\text{Mn}_{0.67}\text{Ni}_{0.16}\text{Co}_{0.17}\text{O}_2$ also exhibits better rate capacity and cycle stability than single-phase material P3- $\text{Na}_{0.57}\text{Mn}_{0.67}\text{Ni}_{0.16}\text{Co}_{0.17}\text{O}_2$ (Figure 9c and d). In addition, the preparation of P3/O3- $\text{Na}_{0.9}\text{Cu}_{0.2}\text{Fe}_{0.28}\text{Mn}_{0.52}\text{O}_2$ shows the regulation of the co-precipitation process can also affect the crystal structure.^[139] The synthesis method of CFM-Cu is as follows. Fe and Mn were first precipitated together followed by the precipitation of Cu, leading to Cu coated on the mixed hydroxide of the other two. Similarly, to obtain CFM-Mn, Fe and Cu were first precipitated together followed by the precipitation of Mn. However, CFM-Cu is P3/O3 composite structure while CFM-Mn is mostly O3 structure.

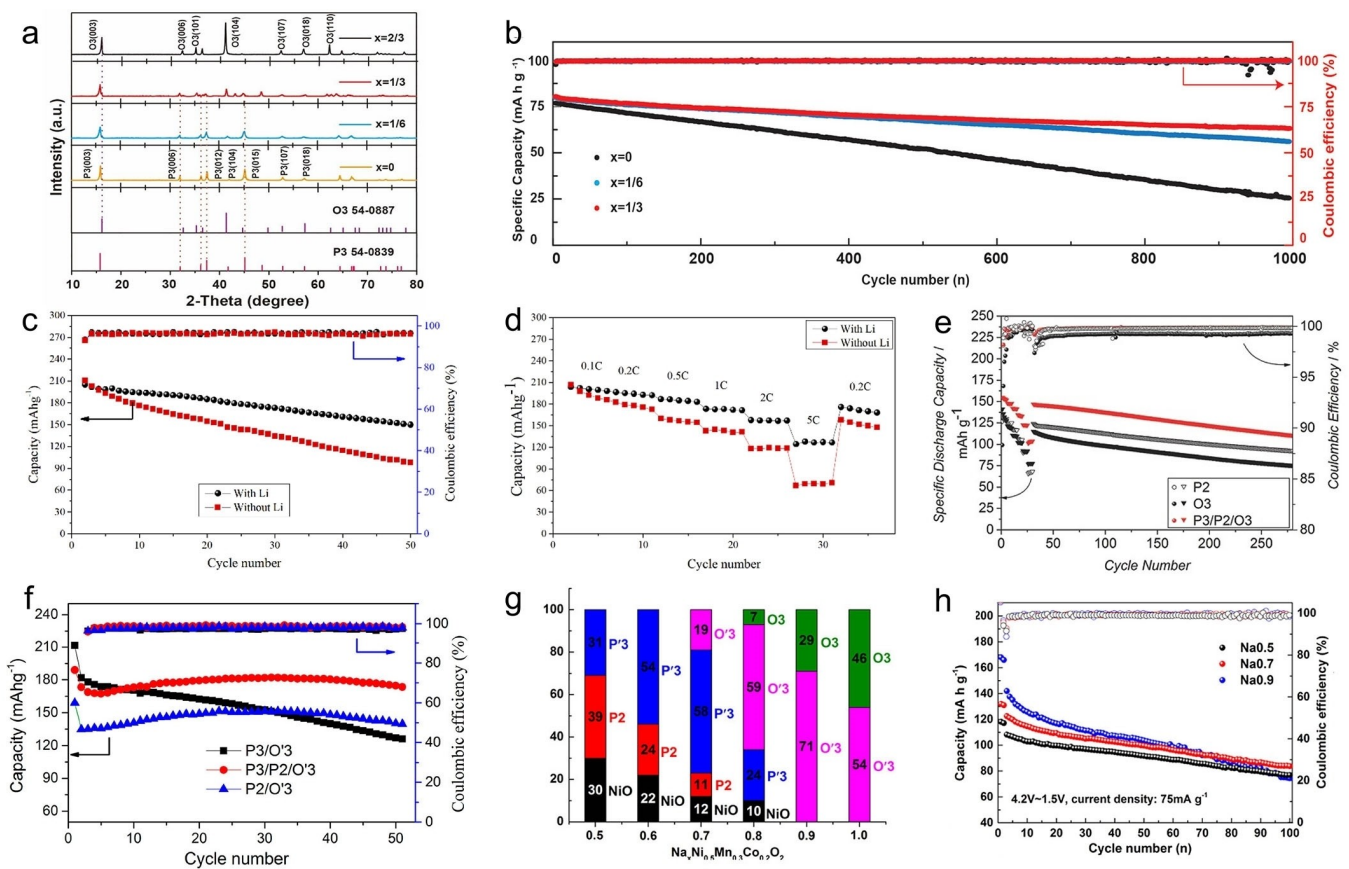


Figure 9. a) Powder XRD patterns and b) Cycling performance at 1 C of Ti-substituted $\text{Na}_{2/3}\text{Ni}_{1/3}\text{Mn}_{2/3-x}\text{Ti}_x\text{O}_2$ ($x = 0, 1/6, 1/3, 2/3$) materials. Reproduced with permission from Ref. [131]. Copyright (2021) Wiley-VCH. c) Cycling performance at 0.1 C and d) rate performance ($1 \text{ C} = 200 \text{ mA g}^{-1}$) of $\text{Na}_{0.57}\text{Li}_{0.17}\text{Mn}_{0.67}\text{Ni}_{0.16}\text{Co}_{0.1}\text{O}_2$ and $\text{Na}_{0.57}\text{Mn}_{0.67}\text{Ni}_{0.16}\text{Co}_{0.1}\text{O}_2$. Reproduced with permission from Ref. [78]. Copyright (2017) Elsevier. e) Rate performance of P3/P2/O3-Na_{0.76}Mn_{0.5}Ni_{0.3}Fe_{0.1}Mg_{0.1}O₂ and O3-NaMn_{0.5}Ni_{0.3}Fe_{0.1}Mg_{0.1}O₂. Reproduced with permission from Ref. [132]. Copyright (2015) Wiley-VCH. f) Cycling performance of P2/P3/O3-Na_{0.70}Li_{0.18}Mn_{0.66}Ni_{0.17}Co_{0.17}O₂ and P2/O3-Na_{0.80}Li_{0.18}Mn_{0.66}Ni_{0.17}Co_{0.17}O₂ at 0.2 C. Reproduced with permission from Ref. [133]. Copyright (2018) American Chemical Society. g) Phase evolution and h) cycling performance of $\text{Na}_x\text{Ni}_{0.5}\text{Mn}_{0.5}\text{Co}_{0.2}\text{O}_2$ materials at C/2 (75 mA g^{-1}). Reproduced with permission from Ref. [134]. Copyright (2018) American Chemical Society.

3.1.4. Multi-composite structure

As previously mentioned, the biphasic materials exhibit enhanced electrochemical properties. In addition to biphasic materials, some studies have investigated multi-composite structure materials^[121,129–131,140–142], especially P3/P2/O3 composite structure.

A series of $\text{Na}_x\text{Mn}_y\text{Ni}_{0.8-y}\text{Fe}_{0.1}\text{Mg}_{0.1}\text{O}_2$ ($0.67 \leq x \leq 1.0$ and $0.5 \leq y \leq 0.7$) were prepared by solid-state reaction,^[129] where P3/P2/O3-Na_{0.76}Mn_{0.5}Ni_{0.3}Fe_{0.1}Mg_{0.1}O₂ is composed of multi-composite phases. Compared to single-phase P2-Na_{2/3}Mn_{0.7}Ni_{0.1}Fe_{0.1}Mg_{0.1}O₂ and O3-NaMn_{0.5}Ni_{0.3}Fe_{0.1}Mg_{0.1}O₂, this multi-composite structure material reveals superior performance in cycle stability and rate capacity (Figure 9e). Stefano Passerini *et al.* carried out further research on P2/P3/O3-Na_xMn_{0.5}Ni_{0.3}Fe_{0.1}Mg_{0.1}O₂.^[140] The results of *ex situ* XANES, *ex situ* EXAFS and *in situ* XANES show the $\text{Ni}^{2+}/\text{Ni}^{4+}$ and $\text{Fe}^{3+}/\text{Fe}^{4+}$ redox couples in P2/P3/O3-Na_xMn_{0.5}Ni_{0.3}Fe_{0.1}Mg_{0.1}O₂ and O3-Na_xMn_{0.5}Ni_{0.3}Fe_{0.1}Mg_{0.1}O₂. However, the main difference is the redox behavior of manganese. There is a significant redox activity of $\text{Mn}^{3+}/\text{Mn}^{4+}$ in O3-Na_xMn_{0.5}Ni_{0.3}Fe_{0.1}Mg_{0.1}O₂ while there is almost no $\text{Mn}^{3+}/\text{Mn}^{4+}$ redox couple in P2/P3/O3-

$\text{Na}_x\text{Mn}_{0.5}\text{Ni}_{0.3}\text{Fe}_{0.1}\text{Mg}_{0.1}\text{O}_2$. The results indicate that manganese is essentially not redox active between 2.5 V and 4.3 V in P2/P3/O3-Na_xMn_{0.5}Ni_{0.3}Fe_{0.1}Mg_{0.1}O₂, which may be due to the presence of P2 phase. Therefore, the stable presence of Mn⁴⁺ during the charge and discharge process results in enhanced cycling and rate performance. Wei *et al.* prepared a series of $\text{Na}_x\text{Li}_{0.18}\text{Mn}_{0.66}\text{Ni}_{0.17}\text{Co}_{0.17}\text{O}_2$ ($0.50 \leq x \leq 0.80$) with varying Na content.^[130] The x , i.e., sodium content largely influences the crystal structure. As the sodium content increases, the proportion of the P2 phase gradually increases and just the reverse for P3. In addition, the substitution of Li leads to the O'3 phase. The results of HAADF-STEM image and EDS maps show enrichment of Na, Ni, and Co in the bright areas, while Mn is less abundant. However, in the darker areas there are higher concentration of Mn and lower levels of Na, Ni and Co, which is consistent with the fact that the distribution of elements in P2 and O'3 phases is uneven.^[73] Among $\text{Na}_x\text{Li}_{0.18}\text{Mn}_{0.66}\text{Ni}_{0.17}\text{Co}_{0.17}\text{O}_2$ ($0.50 \leq x \leq 0.80$), P2/P3/O3-Na_{0.70}Li_{0.18}Mn_{0.66}Ni_{0.17}Co_{0.17}O₂ shows better electrochemical properties than P3/O3-Na_{0.50}Li_{0.18}Mn_{0.66}Ni_{0.17}Co_{0.17}O₂ and P2/O3-Na_{0.80}Li_{0.18}Mn_{0.66}Ni_{0.17}Co_{0.17}O₂ (Figure 9f), which is attributed to the interaction of Na-P3/Na-P2/Li-O'3 in the P2/P3/O3-

$\text{Na}_{0.70}\text{Li}_{0.18}\text{Mn}_{0.66}\text{Ni}_{0.17}\text{Co}_{0.17}\text{O}_2$. *Ex situ* XRD results show the main diffraction peaks of Na–P3 and Na–P2 phases are maintained during the charge/discharge process between 1.5–4.5 V, indicating the phase transitions of P3–P3'' and P2–P2'' are suppressed due to the interlocking effect between the P2/P3 intergrown structure. Similarly, a series of $\text{Na}_x\text{Ni}_{0.5}\text{Mn}_{0.3}\text{Co}_{0.2}\text{O}_2$ with different sodium content ($x=0.5, 0.6, 0.7, 0.8, 0.9$, and 1.0) were prepared via coprecipitation method.^[131] Sodium content can largely influence the crystal structure of $\text{Na}_x\text{Ni}_{0.5}\text{Mn}_{0.3}\text{Co}_{0.2}\text{O}_2$ (Figure 9g). As for electrochemical properties, P2/P3/O'3- $\text{Na}_{0.7}\text{Ni}_{0.5}\text{Mn}_{0.3}\text{Co}_{0.2}\text{O}_2$ exhibits a capacity of $\sim 130 \text{ mAh g}^{-1}$ at 15 mA g^{-1} and more than 90 mAh g^{-1} at 375 mA g^{-1} as well as a capacity retention of 68.4% at 75 mA g^{-1} after 100 cycles in the voltage range of 1.5–4.2 V (Figure 9h), which achieves a good balance among capacity, cycling performance and rate performance.

3.2. Layered-tunnel composite oxide cathode materials

The direct sodium ion diffusion pathways in the tunnel phase structures provide them with excellent structural stability. However, due to the initial sodium content of 0.44, a typical $\text{Na}_{0.44}\text{MnO}_2$ cathode has 0.22 Na^+ extracted and 0.44 Na^+ inserted during charging and discharging between 2 and 3.8 V, corresponding to a charge specific capacity of $\sim 60 \text{ mAh g}^{-1}$ and a discharge specific capacity of $\sim 120 \text{ mAh g}^{-1}$, respectively.^[143] Such a low specific capacity is not sufficient for applications of tunnel phase cathodes in large-scale energy storage. In order to compensate for the specific capacity deficiencies, a strategy to composite P2-type layered structures with tunnel structures has been investigated. The introduction of the P2 layered structure constructs layered-tunnel phase interfaces, both to increase the Na content and to mitigate the severe phase transition in the P2-type structure.^[91,137]

For Na_xMnO_2 , the material is in pure tunnel phase at $x=0.44$. At $x>0.44$, the material gradually shifts to the P2 phase and at $x=0.7$, the material is pure P2 phase and no tunneling phase structure exists.^[91,96] Wu and coworkers presented the P2-Tunnel composite material $\text{Na}_{0.6}\text{MnO}_2$ synthesized by coprecipitation with a high specific capacity and excellent rate and cycling performance,^[144] which displays the initial capacity of 193.6 mAh g^{-1} at 1 C and 83.3 mAh g^{-1} even after 700 cycles at 10 C. A comparison with the pure P2 phase $\text{Na}_{0.7}\text{MnO}_2$ reveals the superior performance of the layered-tunnel composite cathode. The biphasic synergistic effect may increase the Na^+ diffusion coefficient and activate the $\text{Mn}^{3+}/\text{Mn}^{4+}$ redox process to break through the cyclic and capacity limits. Guo *et al.* synthesized $\text{Na}_{0.6}\text{MnO}_2$ using a thermal polymerization method combined with solid-state reaction and investigated in more detail the structural evolution of this layered-tunnel phase composite during charge/discharge process and the reasons for the superior performance of the material.^[96] $\text{Na}_{0.6}\text{MnO}_2$ exhibits extremely high specific capacity of 207.7 mAh g^{-1} at 0.1 C under a voltage range of 1.5–4.2 V. Besides, this cathode can maintain a reversible specific capacity of 140.2 mAh g^{-1} at a high rate of 1 C with little voltage

polarization and has a great cycling performance ($\sim 85\%$ after 100 cycles). *In situ* XRD patterns of the structural evolution of the cathode between 1.5 and 4.3 V (Figure 10a) revealed that the phase transition from the P2 phase to the OP4 phase occurs at charging to high voltage and discharging to low voltage. The OP4 phase exists as an intermediate structure between P2 and O2 phases.^[145,146] The crystal structure exhibits remarkable reversibility during the charge/discharge process, resulting in the impressive cycling stability discussed above.

Elemental substitution can improve the performance of layered-tunnel composite cathodes in many ways. For example, substituting Mn with Co can generate the layered-tunnel composite phase $\text{Na}_{0.44}\text{Co}_{0.1}\text{Mn}_{0.9}\text{O}_2$, which displays a remarkable reversible capacity of 173.2 mAh g^{-1} at 0.2 C, great cycling stability and rate performance.^[98] Analysis of the *in situ* XANES (Figure 10b) spectra showed that the involvement of Co increased the overall valence of Mn, thereby suppressing the Jahn-Teller distortion of Mn^{3+} and improving the cyclic stability of the material.^[147] The Jahn-Teller effect of the tunnel phase can also be suppressed by the substitution of Cu for Mn to obtain $\text{Na}_{0.6}\text{Mn}_{0.9}\text{Cu}_{0.1}\text{O}_2$, which has the enhanced electrochemical performance retaining 96 mAh g^{-1} after 250 cycles at 4 C rate.^[88] Although the Jahn-Teller effect of Mn^{3+} leads to a decrease in structural stability, the increased Mn^{3+} provide a higher specific capacity.^[148] Zhang *et al.* designed the layered-tunnel cathode $\text{Na}_{0.44}\text{MnO}_{1.93}\text{F}_{0.07}$ by anion-doping, which found a balance between specific capacity and structural stability.^[99] The introduction of F^- lowers the valence state of Mn, aggravates the Jahn-Teller distortion of Mn^{3+} and thus forms P2-type layered structure, which in turn compensates for the structural stability. LT- $\text{Na}_{0.44}\text{MnO}_{1.93}\text{F}_{0.07}$ delivers an extraordinary discharge capacity of 149 mAh g^{-1} and 138 mAh g^{-1} at 0.5 C and 1 C, respectively.

Elemental substitution was also employed to generate composite structures to suppress P2–O2 phase transitions and thereby improve the electrochemical properties of layered-tunnel materials. For example, the $\text{Na}_{0.44}\text{Co}_{0.1}\text{Mn}_{0.9}\text{O}_2$ discussed above eliminates the violent phase transition in the P2-type structure and replaces it with a reversible P2–P2' phase transition, which is one of the reasons for the good performance of this cathode.^[97,98,149] The layered-tunnel composite cathode $\text{Na}_{0.6}\text{Fe}_{0.04}\text{Mn}_{0.96}\text{O}_2$ synthesized by the thermal decomposition of metal salts can also transform the violent P2–O2 phase transition into the moderate P2–Z and P2–P2' phase transitions, diminishing the slip and volume changes in the layered structure (Figure 10c and d).^[137,150] As a result, LT- $\text{Na}_{0.6}\text{Fe}_{0.04}\text{Mn}_{0.96}\text{O}_2$ displays a specific capacity of 184.9 mAh g^{-1} at 40 mA g^{-1} and a largely improved capacity retention rate of 83.1% after 300 cycles at 1000 mA g^{-1} . Even the layered structures in some layered-tunnel composite cathodes have no phase transition during charging and discharging, such as $\text{Na}_{0.6}\text{Mn}_{0.98}\text{Zr}_{0.02}\text{O}_2$.^[89,151] The stronger bond energy of Zr–O (760 kJ mol^{-1}) can enhance the structural stability compared to Mn–O (402 kJ mol^{-1}), while the introduction of Zr^{4+} can increase the disorder of the TM layer. Thereby, the cycling and rate performance of $\text{Na}_{0.6}\text{Mn}_{0.98}\text{Zr}_{0.02}\text{O}_2$ can reach 81 mAh g^{-1} at 2 A g^{-1} with 75% retention after 1000 cycles. In addition, a

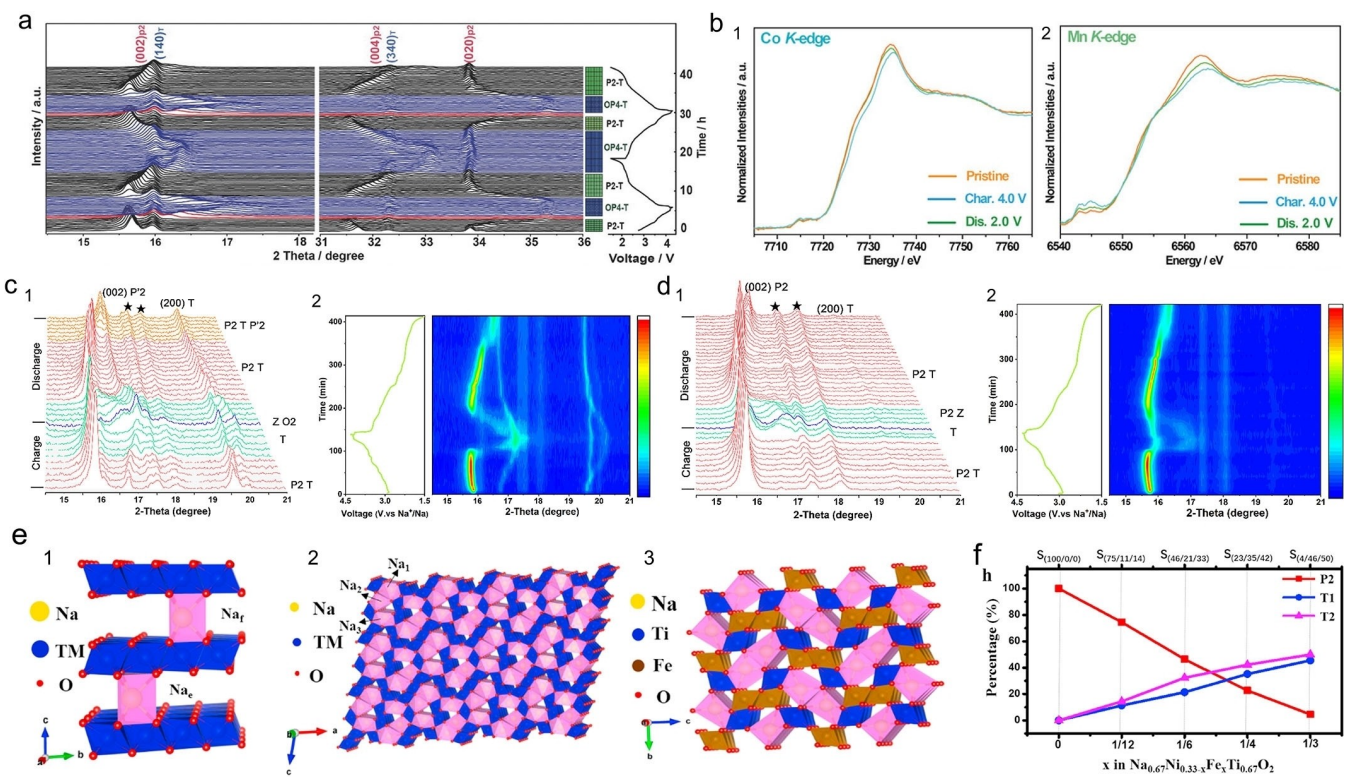


Figure 10. a) *In situ* XRD patterns and phase transitions at different stages of $\text{Na}_{0.6}\text{MnO}_2$ cycling at 0.1 C for two cycles in the voltage range of 1.5 and 4.3 V. Reproduced with permission from Ref. [96]. Copyright (2018) Wiley-VCH. b) *Ex situ* XANES spectra at the Co and Mn K-edge of $\text{Na}_{0.44}\text{Co}_{0.56}\text{Mn}_{0.02}\text{O}_2$ electrode at different charge/discharge states. Reproduced with permission from Ref. [98]. Copyright (2020) Wiley-VCH. c and d) *In situ* XRD patterns of $\text{Na}_{0.6}\text{MnO}_2$ (LT-NM) and $\text{Na}_{0.6}\text{Fe}_{0.04}\text{Mn}_{0.96}\text{O}_2$ (LT-NFM) during the first charge/discharge process between 1.5 and 4.3 V: c₁) XRD patterns of LT-NM and c₂) corresponding contour plots. d₁) XRD patterns of LT-NFM and d₂) corresponding contour plots. The black stars denote the signals related to *in-situ* cell background. Reproduced with permission from Ref. [137]. Copyright (2021) Elsevier. e) Schematic diagrams of e₁) P2 structure, e₂) T1 structure, and e₃) T2 structure in $\text{Na}_{2/3}\text{Ni}_{1/3-x}\text{Fe}_x\text{Ti}_{2/3}\text{O}_2$ ($x=0, 1/12, 1/6, 1/4, 1/3$) samples. f) The fraction of three structures contained in $\text{Na}_{2/3}\text{Ni}_{1/3-x}\text{Fe}_x\text{Ti}_{2/3}\text{O}_2$ as a function of Fe content. Reproduced with permission from Ref. [138]. Copyright (2017) Elsevier.

special layered-tunnel composite cathode $\text{Na}_{2/3}\text{Ni}_{1/6}\text{Fe}_{1/2}\text{Ti}_{2/3}\text{O}_2$ consists of 46% P2- $\text{Na}_{2/3}\text{Ni}_{1/3}\text{Ti}_{2/3}\text{O}_2$, 21% tunnel- $\text{Na}_{2.65}\text{Ti}_{3.35}\text{Fe}_{0.65}\text{O}_9$ (T1) and 33% tunnel- NaFeTiO_4 (T2) (Figure 10e and f).^[138] The P2 phase provides capacity at low voltage, the T1 phase provides capacity at high voltage and the T2 phase without electrochemical activity stabilizes triphasic framework. The novel cathode displays the reversible capacity of 105 mAhg⁻¹ in the voltage range of 0.15–2.5 V and the capacity retention of 86.5% after 1500 cycles at the 1 C rate.

In conclusion, the layered P2 phase acts as a high specific capacity provider in the layered-tunnel composite cathodes, while the tunnel phase provides a stable structure and fast Na^+ diffusion kinetics. Through the biphasic synergistic effect, the layered-tunnel composite cathodes suppress the Jahn-Teller distortion of Mn^{3+} and the intense phase transitions of the layered structure, resulting in composite cathodes for SIBs with improved performance.

3.3. Other composite oxide cathode materials

Coating is an effective method of obtaining composite structure and improving surface properties.^[152,153,157,158] The coating strategy has multiple advantages, such as acting as an

insulation for air and water to meet the requirements of practical applications, as a framework to reduce stress and volume changes to improve cycling performance, and as a fast ion conductor to improve rate performance.^[158] O3- $\text{NaNi}_{0.5}\text{Mn}_{0.5}\text{O}_2$ @ x% P2- $\text{Na}_{2/3}\text{MnO}_2$ (x = 2, 5, 15 and 40) materials were prepared through a wet chemistry process (Figure 11a) and subsequent high-temperature calcination.^[152] The stable P2- $\text{Na}_{2/3}\text{MnO}_2$ coating on the surface inhibits structural degradation. The initial CE and cycling stability have been improved as the content of P2- $\text{Na}_{2/3}\text{MnO}_2$ coating increases. However, excessive P2- $\text{Na}_{2/3}\text{MnO}_2$ coating leads to the reduction of Ni content and low capacity. Therefore, O3- $\text{NaNi}_{0.5}\text{Mn}_{0.5}\text{O}_2$ @ 5% P2- $\text{Na}_{2/3}\text{MnO}_2$ achieves a balance between capacity and cycle stability, exhibiting the best Na storage performance (Figure 11b and c). O3- $\text{NaNi}_{0.5}\text{Mn}_{0.5}\text{O}_2$ @ 5% P2- $\text{Na}_{2/3}\text{MnO}_2$ exhibits a reversible capacity of 119.4 mAhg⁻¹ with a capacity retention of 85.3% after 150 cycles at 1 C compared to 74.8% (104.2 mAh g⁻¹) of O3- $\text{NaNi}_{0.5}\text{Mn}_{0.5}\text{O}_2$. In addition, the P2- $\text{Na}_{2/3}\text{MnO}_2$ coating also exhibits fast Na-ion diffusion channels and improved thermal and air stability. Similarly, 60% O3/O'3- $\text{Na}_{0.8}[\text{Ni}_{0.5}\text{Co}_{0.2}\text{Mn}_{0.3}]\text{O}_2$ @ 40% P2- $\text{Na}_{0.8}[\text{Ni}_{0.33}\text{Mn}_{0.67}]\text{O}_2$ were prepared by a coprecipitation method.^[157] STEM-HAADF images show a coherent P2/O3 intergrown structure between P2 shell and inner O3 core. The results of electron-probe X-ray micro-

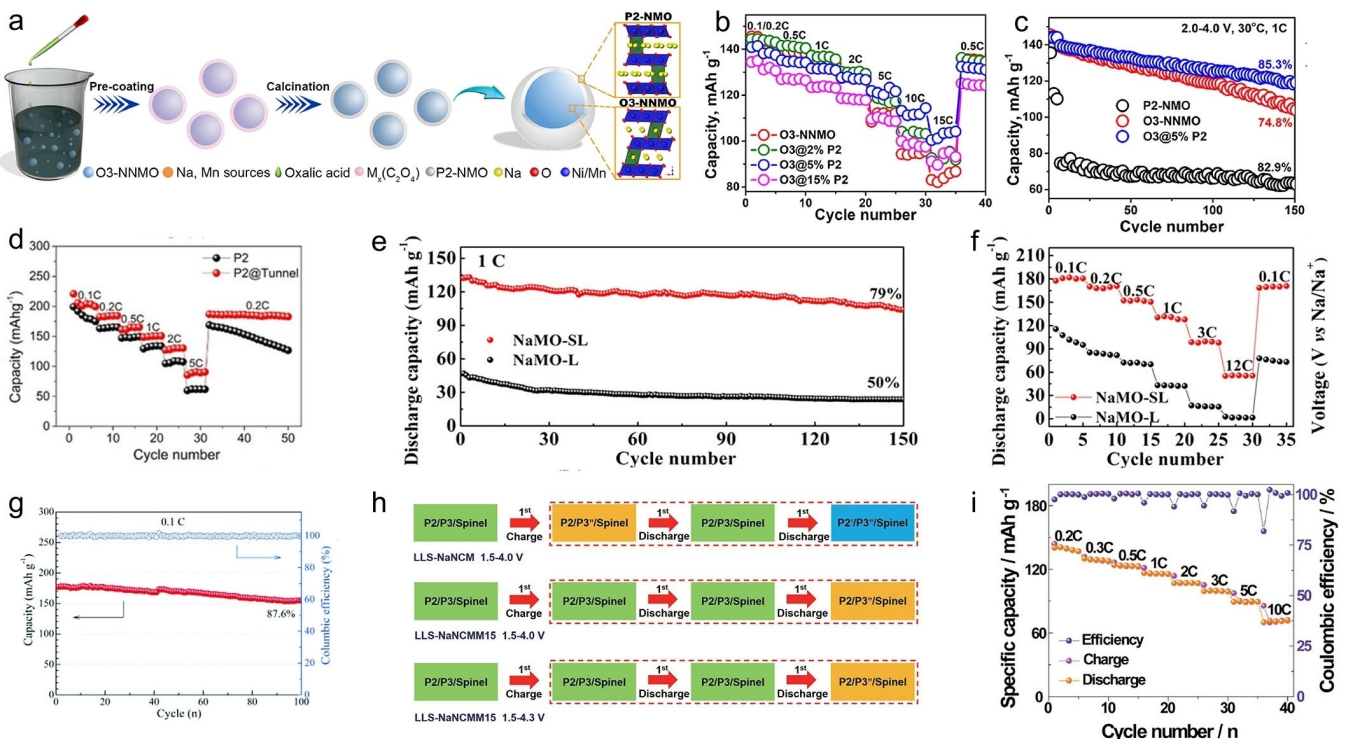


Figure 11. a) Schematic diagram of the synthesis method, b) rate performance and c) cycling performance at 1 C of $O_3\text{-}NaNi_{0.5}Mn_{0.5}O_2@x\%P2\text{-}Na_{2/3}MnO_2$. Reproduced with permission from Ref. [152]. Copyright (2022) Elsevier. d) Rate performance of the P2 with and without surface coating between 1.5 and 4.5 V. Reproduced with permission from Ref. [153]. Copyright (2020) Wiley-VCH. e) Cycling performance at 1 C and f) rate performance of NaMO-SL and NaMO-L. Reproduced with permission from Ref. [154]. Copyright (2020) American Chemical Society. g) Cycling performance at 0.1 C of $Na_{0.5}Ni_{0.2}Co_{0.15}Mn_{0.65}O_2$. Reproduced with permission from Ref. [155]. Copyright (2018) RSC Pub. h) Schematic showing the crystal structural evolution of different cathodes at different conditions. i) Rate performance of $Na_{0.5}Ni_{0.05}Co_{0.15}Mn_{0.65}Mg_{0.15}O_2$ (LLS-NaNCMM15) between 1.5 and 4.3 V. Reproduced with permission from Ref. [156]. Copyright (2022) Wiley-VCH.

analysis (EPMA) show that Mn concentration on the core is lower than shell while the distribution of Ni and Co is the opposite. The results of cross-sectional SEM images for electrodes after 50 cycles show many intergranular cracks between and within primary particles in $O_3/O'\text{-}Na[Ni_{0.5}Co_{0.2}Mn_{0.3}]O_2$ while no apparent cracks in 60% $O_3/O'\text{-}Na_{0.8}[Ni_{0.5}Co_{0.2}Mn_{0.3}]O_2@40\%Na_{0.8}[Ni_{0.33}Mn_{0.67}]O_2$. The tunnel structure materials can also be used as a protecting layer. Wei *et al.* used a tunnel structure $Na_{0.44}Mn_{0.5}Ti_{0.5}O_2$ as a coating and obtain P2@tunnel 0.75 $Na_{0.7}Mn_{0.66}Ni_{0.17}Co_{0.17}O_2\cdot0.25Na_{0.44}Mn_{0.5}Ti_{0.5}O_2$ [153] which is confirmed by TEM. In addition, the results of EELS show that the oxidation state of Mn on the surface is lower than that in the bulk, indicating that a tunnel structure has formed on the surface. The tunnel structure coating provides enough migration channels for Na^+ and better rate performance (Figure 11d).

Unlike the preparation process of coating, Yan and co-workers prepared P2@P3- $Na_{0.78}Cu_{0.27}Zn_{0.06}Mn_{0.67}O_2$ via a sol-gel method.^[82] The result of dynamic secondary ion mass spectroscopy (SIMS) show sodium concentration on the surface is lower than within while Mn concentration on the surface is higher than within, indicating that the distribution of elements in P2 and P3 phases is uneven. The HAADF and ABF images combined with FFT show the intergrowth structure between P2 and P3 phases. EELS signals of P2@P3- $Na_{0.78}Cu_{0.27}Zn_{0.06}Mn_{0.67}O_2$

in different charge states show that Cu undergoes redox reaction in both P2 and P3 phases whereas Mn in the P3 phase is not electrochemically active. Zn-doping not only leads to the formation of P3 phase on the surface, but also enhances the electrochemical properties compared to P2- $Na_{0.78}Cu_{0.33}Mn_{0.67}O_2$.

Taking advantage of the high ionic conductivity and stable structure of spinel structures,^[159-163] layered and spinel oxides have been integrated into a composite material aimed at increasing the specific capacity of Na ion batteries while pursuing higher rate performance and cycling performance. In order to solve the issue of poor structural stability and low rate performance of the material at high operating voltages, a Li-substituted O3/spinel $Na_{0.87}Li_{0.25}Ni_{0.4}Fe_{0.2}Mn_{0.4}O_{2+\delta}$ (LS-NFM) electrode was investigated.^[164] In typical Li-substituted Na ion cathode materials, lithium ions occupy Na and/or TM sites and form single-phase or composite phase layered cathodes. However, by increasing the lithium stoichiometry, a spinel-layered cathode can be prepared, which consists of Extensive O3 structure (94%) and minor spinel structure (6%). The HRTEM results show that there is an intergrowth structure between the layered and spinel structures. In terms of electrochemical performance, the LS-NFM maintains 86% after 100 cycles at a current density of 100 mA g^{-1} in the voltage range of 2–4.2 V, which shows a significant improvement in cycling stability and rate performance compared to the undoped $NaNi_{0.4}Fe_{0.2}Mn_{0.4}O_2$.

(70% capacity retention). The spinel-layered materials can also be obtained by electrochemical Li^+/Na^+ exchange strategies.^[154] The NMO-SL prepared by this method delivers a specific capacity of 180.9 mAh g^{-1} at 0.1 C and maintained 79% after 150 cycles at 1 C. The as-obtained spinel-layered composite NMO-SL delivers a high discharge capacity of 180.9 mAh g^{-1} at 0.1 C and a high capacity retention of 79% after 150 cycles at 1 C (Figure 11e). Benefiting from the high Na^+ diffusion coefficient of the spinel-layered composite, a specific capacity of 55.7 mAh g^{-1} is maintained even at a high rate of 12 C (Figure 11f). By *ex situ* XRD analysis, it was demonstrated that the material undergoes reversible phase transition during charging and discharging, increasing the cyclic stability of the cathode.

The P2/spinel composite cathode $\text{Na}_{1/2}\text{Ni}_{1/6}\text{Co}_{1/6}\text{Mn}_{2/3}\text{O}_2$ was investigated and it was demonstrated that the integrated-spinel phase accelerates electron transfer.^[165] Similarly, the $\text{Na}_{0.5}[\text{Ni}_{0.2}\text{Co}_{0.15}\text{Mn}_{0.65}]\text{O}_2$ cathode has a composite structure of layered P2/P3 and $Fd\bar{3}m$ spinel phases.^[155] This cathode provides a specific capacity of 180 mAh g^{-1} and maintains 87.6% after 100 cycles at 0.1 C (Figure 11g). A reversible capacity of 105 mAh g^{-1} , even at 10 C, indicates great rate performance. The excellent properties of this cathode were due to the structural stability provided by the P2/P3-type composite structure^[134] and the high electronic conductivity provided by the spinel oxides $\text{Ni}_x\text{Co}_y\text{Mn}_{3-x-y}\text{O}_4$. Furthermore, $\text{Na}_{0.5}\text{Ni}_{0.05}\text{Co}_{0.15}\text{Mn}_{0.65}\text{Mg}_{0.15}\text{O}_2$ (LLS-NaNCMM15) was prepared on the basis of $\text{Na}_{0.5}[\text{Ni}_{0.2}\text{Co}_{0.15}\text{Mn}_{0.65}]\text{O}_2$ (LLS-NaNCM) by replacing Ni with Mg, and the triphasic composite heterostructure possessed by this material exhibited excellent electrochemical properties.^[156] By *in situ* XRD, the structure evolution during the cycling of LLS-NaNCM and LLS-NaNCMM15 was analyzed. The XRD analysis shows that the LLS-NaNCM electrode undergoes a violent structural evolution during charging and discharging, while the LLS-NaNCMM15 electrode exhibits a moderate phase transition (Figure 11h). The LLS-NaNCMM15 electrode delivers a specific capacity of 169.4 mAh g^{-1} at 0.2 C within 1.5–4.3 V and Figure 11(i) shows that this cathode even delivers 117.1 mAh g^{-1} at 2 C, indicating great rate performance. In conclusion, the layered material acts as a high specific capacity provider in the layered spinel composite, while the spinel phase provides a stable structure and fast ion diffusion kinetics, and the intergrowth structure existing between the two phases combines the advantages of both phases to form a composite sodium ion cathode material with improved performance.

3.4. Comparison and generalization of electrochemical performance

In this section, we compare the electrochemical performance of composite oxide cathode materials with those of mixing oxide cathode materials and single-phase cathode materials (Table 3). Besides, the electrochemical properties such as specific capacity, rate capacity and cycling performance of the composite oxide cathode materials are summarized in the Table 4.

Some studies have compared the performance of composite oxide cathode materials and mixing oxide cathode materials.^[101,152] As mentioned before, Sun and coworkers prepared the composite cathode $\text{O}3\text{-NaNi}_{0.5}\text{Mn}_{0.5}\text{O}_2@5\% \text{P}2\text{-Na}_{2/3}\text{MnO}_2$. Besides, a $\text{P}2 + \text{O}3$ material was prepared by manual mixing 5 mol% $\text{P}2\text{-Na}_{2/3}\text{MnO}_2$ and 95 mol% $\text{O}3\text{-NaNi}_{0.5}\text{Mn}_{0.5}\text{O}_2$.^[152] Similarly, Guo and coworkers prepared 46.7% $\text{P}2 + 53.3\% \text{P}3\text{-Na}_{0.7}\text{Li}_{0.06}\text{Mg}_{0.06}\text{Ni}_{0.22}\text{Mn}_{0.67}\text{O}_2$ by mixing the individual $\text{P}3$ and $\text{P}2$ cathodes to compare with $\text{P}2/\text{P}3\text{-Na}_{0.7}\text{Li}_{0.06}\text{Mg}_{0.06}\text{Ni}_{0.22}\text{Mn}_{0.67}\text{O}_2$.^[101] As shown in Table 3, the composite oxide cathode materials and mixing oxide cathode materials exhibit similar specific capacity at low rate. However, composite oxide cathode materials show superior rate capability and long-term cycle stability, indicating the effect of intergrowth structure between different phases.

Similarly, some studies have compared the performance of composite oxide cathode materials and single-phase cathode materials.^[49,58,105,108,128,149] For example, the single-phase materials $\text{P}2\text{-Na}_{2/3}\text{Ni}_{1/3}\text{Mn}_{0.57}\text{Ti}_{0.1}\text{O}_2$ and $\text{O}3\text{-NaNi}_{1/3}\text{Fe}_{1/3}\text{Mn}_{1/3}\text{O}_2$ were prepared by Wang *et al.* for comparison with $\text{P}2/\text{O}3\text{-Na}_{0.766}\text{Ni}_{0.33}\text{Mn}_{0.5}\text{Fe}_{0.1}\text{Ti}_{0.07}\text{O}_2$.^[49] Another example is that different crystal structure $\text{Na}_{0.7}\text{Li}_{0.06}\text{Mg}_{0.06}\text{Ni}_{0.22}\text{Mn}_{0.67}\text{O}_2$ can be obtained by controlling the calcination temperature.^[101] Almost all of the composite oxide cathode materials show better cycling performance and rate capability than single-phase materials, which also suggests that the intergrowth structure is beneficial for the electrochemical properties.

4. Reaction Mechanism

As summarized in Chapter 3, composite oxide cathode materials show better electrochemical properties than mixing materials and single-phase materials. Many studies have proposed mechanisms to explain the enhanced electrochemical performance of composite oxide cathode materials.

A biphasic clamping reaction mechanism was proposed based on the HRTEM results (Figure 12a).^[49] With the extraction of sodium ions, the $\text{O}3 - \text{P}3$ phase transition occurs and the TM layers in $\text{O}3$ phase tend to slide. The $\text{P}2$ phase applies a stress in the opposite direction to the sliding, which suppresses the structure strain. The interaction between different phases is similar in subsequent phase transitions. As a result, the shrinkage of interslab distance in $\text{P}2/\text{O}3$ composite structure is largely suppressed (11.3% of $\text{P}2\text{-Na}_{2/3}\text{Ni}_{1/3}\text{Mn}_{0.57}\text{Ti}_{0.1}\text{O}_2$ vs. 7.2% of the $\text{P}2$ phase in $\text{P}2/\text{O}3\text{-Na}_{0.766}\text{Ni}_{0.33}\text{Mn}_{0.5}\text{Fe}_{0.1}\text{Ti}_{0.07}\text{O}_2$ and 4.9% of $\text{O}3\text{-NaNi}_{1/3}\text{Fe}_{1/3}\text{Mn}_{1/3}\text{O}_2$ vs. 2.7% of the $\text{O}3$ phase in $\text{P}2/\text{O}3\text{-Na}_{0.766}\text{Ni}_{0.33}\text{Mn}_{0.5}\text{Fe}_{0.1}\text{Ti}_{0.07}\text{O}_2$). The excellent structure stability in $\text{P}2/\text{O}3\text{-Na}_{0.766}\text{Ni}_{0.33}\text{Mn}_{0.5}\text{Fe}_{0.1}\text{Ti}_{0.07}\text{O}_2$ leads to enhanced cycling and rate performance. Based on the observations of HAADF-STEM, Wei *et al.* proposed an interfacial shear stress modulation mechanism (Figure 12b).^[76] Unlike the phase transition of $\text{P}2 - \text{O}2$ in $\text{P}2\text{-Na}_{0.67}\text{Ni}_{0.33}\text{Mn}_{0.67}\text{O}_2$ leading to large lattice mismatch and structural degradation, the major diffraction peaks of $\text{P}2$ phase in $\text{P}2/\text{O}3\text{-Na}_{0.67}\text{Li}_{0.16}\text{Mn}_{0.67}\text{Ni}_{0.33}\text{O}_{2+\delta}$ are completely maintained. For $\text{P}2/\text{O}3\text{-Na}_{0.67}\text{Li}_{0.16}\text{Mn}_{0.67}\text{Ni}_{0.33}\text{O}_{2+\delta}$, the fact that a -axis of $\text{Li}-\text{O}3$ is larger than that of the $\text{P}2$ phase leads to lattice

Table 3. The Comparison of the electrochemical properties of mixing oxide cathodes, single-phase oxide cathodes and composite oxide cathodes.

Material	Specific capacity [mAh g ⁻¹]	Rate performance [mAh g ⁻¹]	Capacity retention
O3-NaNi _{0.5} Mn _{0.5} O ₂ @ 5% P2-Na _{2/3} MnO ₂ ^[152]	141.4 (0.1 C 2.0–4.0 V)	103.7 (15 C 2.0–4.0 V)	85.3% (2.0–4.0 V at 1 C, 150 cycles)
5% P2-Na _{2/3} MnO ₂ + 95% O3-NaNi _{0.5} Mn _{0.5} O ₂ ^[152]	~140 (0.1 C 2.0–4.0 V)	89.9 (15 C 2.0–4.0 V)	78.4% (2.0–4.0 V at 1 C, 150 cycles)
P2/P3-Na _{0.7} Li _{0.06} Mg _{0.06} Ni _{0.22} Mn _{0.67} O ₂ ^[101]	122.3 (0.2 C 2.0–4.4 V)	~102 (5 C 2.0–4.4 V)	97.2% (2.0–4.4 V at 0.2 C, 50 cycles)
46.7%P2-Na _{0.7} Li _{0.06} Mg _{0.06} Ni _{0.22} Mn _{0.67} O ₂ + 53.3%P3-Na _{0.7} Li _{0.06} Mg _{0.06} Ni _{0.22} Mn _{0.67} O ₂ ^[101]	~120 (0.2 C 2.0–4.4 V)	~15 (5 C 2.0–4.4 V)	~75% (2.0–4.4 V at 0.2 C, 50 cycles)
P2/O3-Na _{0.766} Ni _{0.33} Mn _{0.5} Fe _{0.1} Ti _{0.07} O ₂ ^[49]	144 (0.1 C 2.2–4.3 V)	92 (10 C 2.2–4.3 V)	79.2% (2.2–4.3 V at 1 C, 100 cycles)
P2-Na _{2/3} Ni _{1/3} Mn _{0.57} Ti _{0.1} O ₂ ^[49]	138.3 (0.1 C 2.2–4.3 V)	78.8 (10 C 2.2–4.3 V)	61.8% (2.2–4.3 V at 1 C, 100 cycles)
O3-NaNi _{1/3} Fe _{1/3} Mn _{1/3} O ₂ ^[49]	172 (0.1 C 2.2–4.3 V)	79.8 (10 C 2.2–4.3 V)	69.8% (2.2–4.3 V at 1 C, 100 cycles)
P2/O3-Na _{0.85} Ni _{0.34} Mn _{0.33} Ti _{0.33} O ₂ ^[58]	126.6 (0.1 C 2.2–4.4 V)	82.4 (10 C 2.2–4.4 V)	80.6% (2.2–4.4 V at 1 C, 200 cycles)
P2-Na _{0.85} Ni _{0.34} Mn _{0.66} O ₂ ^[58]	148.1 (0.1 C 2.2–4.4 V)	43.0 (10 C 2.2–4.4 V)	40.4% (2.2–4.4 V at 1 C, 200 cycles)
O3-Na _{0.85} Ni _{0.34} Mn _{0.22} Ti _{0.44} O ₂ ^[58]	121.5 (0.1 C 2.2–4.4 V)	75.4 (10 C 2.2–4.4 V)	77.7% (2.2–4.4 V at 1 C, 200 cycles)
P2/O3-Na _{0.78} Ni _{0.2} Fe _{0.38} Mn _{0.42} O ₂ ^[108]	86 (0.1 C 2.5–4 V)	78.3 (2 C 2.5–4 V)	92.0% (2.5–4 V at 0.1 C, 100 cycles)
mainly P2-Na _{0.7} Ni _{0.2} Fe _{0.3} Mn _{0.5} O ₂ ^[108]	71.7 (0.1 C 2.5–4 V)	~70 (2 C 2.5–4 V)	93.8% (2.5–4 V at 0.1 C, 100 cycles)
O3-NaNi _{0.2} Fe _{0.6} Mn _{0.2} O ₂ ^[108]	116.5 (0.1 C 2.5–4 V)	~35 (2 C 2.5–4 V)	47.8% (2.5–4 V at 0.1 C, 50 cycles)
P2/O3-Na _{0.76} Ni _{0.20} Fe _{0.40} Mn _{0.40} O ₂ ^[105]	118.5 (0.1 C 2.0–4.0 V)	~90 (1 C 2.0–4.0 V)	78% (2.0–4.0 V at 0.1 C, 100 cycles)
P2-Na _{0.60} Ni _{0.20} Fe _{0.40} Mn _{0.40} O ₂ ^[105]	118.4 (0.1 C 2.0–4.0 V)	~90 (1 C 2.0–4.0 V)	51% (2.0–4.0 V at 0.1 C, 100 cycles)
O3-Na _{0.84} Ni _{0.20} Fe _{0.40} Mn _{0.40} O ₂ ^[105]	72.1 (0.1 C 2.0–4.0 V)	~30 (1 C 2.0–4.0 V)	40% (2.0–4.0 V at 0.1 C, 100 cycles)
P3/O3-Na _{2/3} Ni _{1/3} Mn _{1/3} Ti _{1/3} O ₂ ^[128]	~86 (0.1 C 2.5–4.15 V)	~76 (5 C 2.5–4.15 V)	78% (2.5–4.15 V at 1 C, 1000 cycles)
P3-Na _{2/3} Ni _{1/3} Mn _{2/3} O ₂ ^[128]	86 (0.1 C 2.5–4.15 V)	71.2 (5 C 2.5–4.15 V)	36% (2.5–4.15 V at 1 C, 1000 cycles)
O3-Na _{2/3} Ni _{1/3} Ti _{2/3} O ₂ ^[128]	~84 (0.1 C 2.5–4.15 V)	~73 (1 C 2.5–4.15 V)	74% (2.5–4.15 V at 1 C, 200 cycles)
P2/P3-Na _{0.7} Li _{0.06} Mg _{0.06} Ni _{0.22} Mn _{0.67} O ₂ ^[101]	122.3 (0.2 C 2.0–4.4 V)	~102 (5 C 2.0–4.4 V)	~68.7% (2.0–4.4 V at 0.2 C, 100 cycles)
P2-Na _{0.7} Li _{0.06} Mg _{0.06} Ni _{0.22} Mn _{0.67} O ₂ ^[101]	~122 (0.2 C 2.0–4.4 V)	~73.4 (5 C 2.0–4.4 V)	~46.7% (2.0–4.4 V at 0.2 C, 100 cycles)
P3-Na _{0.7} Li _{0.06} Mg _{0.06} Ni _{0.22} Mn _{0.67} O ₂ ^[101]	~122 (0.2 C 2.0–4.4 V)	~83.3 (5 C 2.0–4.4 V)	~56.6% (2.0–4.4 V at 0.2 C, 100 cycles)

parameters mismatch. Moreover, during the charge process, the lattice parameters mismatch between P2 and Li-O3 phase results in interfacial shear stress, suppressing the shrinkage of α -axis and gliding of the TM layers. The phase transitions of P2/O3-Na_{0.67}Li_{0.11}Fe_{0.36}Mn_{0.36}Ti_{0.17}O₂ and P2-Na_{0.67}Fe_{0.5}Mn_{0.5}O₂ were compared in detail (Figure 12c).^[60] The *ex situ* XRD results illustrate the phase transition of P2-OP4 is partly restrained in Li/Ti co-substituted material. In addition, the layer spacing of OP4 phase in Li/Ti co-substituted material is 5.28 Å compared to 5.09 Å for the original material P2-Na_{0.67}Fe_{0.5}Mn_{0.5}O₂. The larger layer spacing of OP4 phase relieves the stress at the boundary between P2 and OP4 phases. Zhang and coworkers proposed a mechanism to explain the interaction of different phases. The difference in layer spacing between P2 and OP4 phases ($\Delta d = 0.28$ Å) is largely suppressed due to the nailing effect of O3 phase in P2/O3 composite structure, whereas the lattice mismatch in P2-Na_{0.67}Fe_{0.5}Mn_{0.5}O₂ is severe ($\Delta d = 0.49$ Å). This interaction between P2 and O3 greatly increases the

structural stability. Therefore, the dissolution of Mn and the formation of micro-cracks are greatly suppressed in P2/O3-Na_{0.67}Li_{0.11}Fe_{0.36}Mn_{0.36}Ti_{0.17}O₂ shown by X-ray fluorescence and HRTEM. An interface interlocking reaction mechanism to explain the excellent cycle stability and rate performance of P2/O3-Na_{0.85}Ni_{0.34}Mn_{0.33}Ti_{0.33}O₂ (Figure 12d).^[58] During the initial charge process, the O3 undergoes O3-P3 phase transformation while the crystal structure of P2 remains stable and plays a pillar role. As the charging process continues, the P2 and P3 structures hinder each other causing the stress in the opposite direction to the gliding, thus, inhibiting the gliding of the TMO₂ slabs. The “interlocking effect” also occurs during the subsequent phase transformations, leading to less lattice mismatch and relieved TMO₂ slabs gliding. The similar mechanism also exists in layered-spinel composite structure.^[156] Chou *et al.* reveals the mechanism of regulating local chemistry to realize strain engineering (Figure 12e). During the charge/discharge process, the spinel structure phase enhances structural stability.

Table 4. A summary of the electrochemical properties of composite oxide cathode materials.

Material	Cut-Off voltage [V]	Specific capacity [mAh g ⁻¹]	Capacity retention
P2/O3-Na _{0.76} Ni _{0.33} Mn _{0.5} Fe _{0.1} Ti _{0.07} O ₂ ^[49]	2.2–4.3	144 (0.1 C)/92 (10 C)	79.2% (1 C,100 cycles)
P2/O3-Na _{0.85} Ni _{0.34} Mn _{0.33} Ti _{0.33} O ₂ ^[58]	2.2–4.4	126.6 (0.1 C)/82.4 (10 C)	80.6% (1 C, 200 cycles)
P2/O3-Na _{0.78} Ni _{0.2} Fe _{0.38} Mn _{0.42} O ₂ ^[108]	2.5–4	86 (0.1 C)/78.3 (2 C)	92.0% (0.1 C,100 cycles)
P2/O3-Na _{0.76} Ni _{0.20} Fe _{0.40} Mn _{0.40} O ₂ ^[105]	2.0–4.0	118.5 (0.1 C)/~90 (1 C)	78% (0.1 C,100 cycles)
P2/O3-Na _{0.8} Mn _{0.55} Ni _{0.25} Fe _{0.1} Ti _{0.1} O ₂ ^[107]	1.5–4.3	153 (0.1 C)/~81 (1 C)	71.9% (0.1 C,100 cycles)
P2/O3-Na _{0.88} Ni _{0.45} Mn _{0.5} O ₂ ^[106]	2.0–4.0	127.7 (0.05 C)/106.7 (1 C)	71.1% (1 C,250 cycles)
P2/O3-Na _{0.67} Fe _{0.425} Mn _{0.425} Mg _{0.15} O ₂ ^[59]	1.5–4.2	146.6 (0.1 C)/98.1 (1 C)	87.7% (1 C,100 cycles)
P2/O3-Na _{0.67} Li _{0.1} Fe _{0.36} Mn _{0.36} Ti _{0.17} O ₂ ^[60]	1.5–4.2	235 (0.1 C)/172 (1 C)	~63.7% (0.1 C,90 cycles)
P2/O3-Na _{0.67} Li _{0.1} Fe _{0.36} Mn _{0.36} Ti _{0.17} O ₂ ^[60]	2.0–4.2	~146 (1 C)	85.4% (1 C,100 cycles)
P2/O3-Na _{0.67} Li _{0.16} Mn _{0.67} Ni _{0.33} O _{2+δ} ^[76]	2.0–4.5	145 (0.1 C)/104 (5 C)	70.2% (0.5 C,200 cycles)
P2/O3-Na _{0.66} Li _{0.18} Mn _{0.71} Ni _{0.21} Co _{0.08} O _{2+δ} ^[71]	1.5–4.5	200 (0.1 C)/134 (1 C)	75% (0.5 C,150 cycles)
P2/O3-Na _{0.66} Li _{0.18} Mn _{0.66} Ni _{0.12} Co _{0.17} O _{2+δ} ^[73]	1.5–4.5	187.1 (0.1 C)/114 (5 C)	107.6% (0.2 C,60 cycles)
P2/O3-Na _{0.8} Li _{0.2} Ni _{0.33} Mn _{0.67} O ₂ ^[75]	2.0–4.3	127.8 (0.1 C)/70.1 (20 C)	61.5% (0.1 C,200 cycles)
P2/O3-Na _{2/3} Li _{1/3} Mn _{0.8} Fe _{0.2} O ₂ ^[72]	1.5–4.2	125 (0.1 C)/105 (1 C)	69.6% (0.1 C,100 cycles)
P2/O3-Na _{0.8} Li _{0.2} Fe _{0.2} Mn _{0.6} O ₂ ^[109]	2.0–4.6	174 (0.1 C)/108 (1 C)	82% (0.1 C,100 cycles)
P2/O3-Na _{0.67} Li _{0.2} Fe _{0.2} Mn _{0.6} O ₂ ^[122]	1.5–4.5	227 (10 mA g ⁻¹)/73 (600 mA g ⁻¹)	69.9% (10 mA g ⁻¹ ,60 cycles)
P3/O3-Na _{2/3} Ni _{1/3} Mn _{1/3} Ti _{1/3} O ₂ ^[128]	2.5–4.15	86 (0.1 C)/76 (5 C)	78% (1 C,1000 cycles)
P3/O3-Na _{0.57} Li _{0.17} Mn _{0.67} Ni _{0.16} Co _{0.17} O ₂ ^[78]	1.5–4.5	204.8 (0.1 C)/126 (5 C)	73.2% (0.1 C,50 cycles)
P3/P2/O3-Na _{0.76} Mn _{0.5} Ni _{0.3} Fe _{0.1} Mg _{0.1} O ₂ ^[129]	2.0–4.3	154.2 (0.1 C)/134 (1 C)	91.3% (1 C,50 cycles)
P3/P2/O3-Na _{0.76} Mn _{0.5} Ni _{0.3} Fe _{0.1} Mg _{0.1} O ₂ ^[129]	2.5–4.3	128.2 (0.1 C)/~113 (1 C)	90.2% (1 C,600 cycles)
P2/P3/O3-Na _{0.70} Li _{0.18} Mn _{0.66} Ni _{0.17} Co _{0.17} O ₂ ^[130]	1.5–4.5	189 (0.2 C)/~105 (5 C)	~92.1% (0.2 C,50 cycles)
P2/P3/O3-Na _{0.7} Ni _{0.3} Mn _{0.3} Co _{0.2} O ₂ ^[131]	1.5–4.2	~130 (0.1 C)/~93 (5 C)	68.4% (0.5 C,100 cycles)
P2@P3-Na _{0.76} Cu _{0.27} Zn _{0.06} Mn _{0.67} O ₂ ^[82]	2.5–4.1	88 (0.1 C)/73 (5 C)	85% (1 C,200 cycles)
O3-NaNi _{0.5} Mn _{0.5} O ₂ @ 5% P2-Na _{2/3} MnO ₂ ^[152]	2.0–4.0	141.4 (0.1 C)/103.7 (15 C)	85.3% (1 C,150 cycles)
P2/P3-Na _{0.6} Ni _{0.22} Fe _{0.11} Mn _{0.66} O ₂ ^[104]	1.5–4.6	216 (15 mA g ⁻¹)	60% (15 mA g ⁻¹ ,60 cycles)
P2/P3-Na _{0.66} Co _{0.5} Mn _{0.5} O ₂ ^[134]	1.5–4.3	156.1 (1 C)/86.5 (10 C)	91% (10 C,100 cycles)
P2/P3-Na _{0.67} Ni _{0.33} Mn _{0.66} Sn _{0.01} O ₂ ^[62]	1.5–4.5	245 (0.1 C)/~175 (1 C)	73% (1 C,50 cycles)
P2/P3-Na _{0.67} Ni _{0.33} Mn _{0.66} Sn _{0.01} O ₂ ^[62]	2.0–4.2	~93 (0.1 C)/~89 (1 C)	100% (1 C,50 cycles)
P2/P3-Na _{0.67} Mn _{0.64} Co _{0.30} Al _{0.06} O ₂ ^[83]	1.5–4.0	160 (20 mA g ⁻¹)/83 (10 C)	81% (1000mA g ⁻¹ ,200 cycles)
P2/P3-Na _{0.75} Co _{0.125} Cu _{0.125} Fe _{0.125} Ni _{0.125} Mn _{0.5} O ₂ ^[84]	2.0–4.0	~90 (0.1 C)/~55 (5 C)	84.2% (1 C, 1000 cycles)
P2/P3-Na _{0.6} Mn _{0.75} Ni _{0.25} O ₂ ^[61]	2.0–4.1	140.64 (0.1 C)/57.35 (8 C)	68% (1 C, 500 cycles)
P2/P3-Na _{0.7} Li _{0.06} Mg _{0.06} Ni _{0.22} Mn _{0.67} O ₂ ^[101]	2.0–4.4	122.3 (0.2 C)/~102 (5 C)	~68.7% (0.2 C,100 cycles)
P2/T-Na _{0.6} MnO ₂ ^[144]	1.5–4.3	193.6 (1 C)/~118(10 C)	~70.6% (10 C,700 cycles)
P2/T-Na _{0.6} MnO ₂ ^[96]	1.5–4.2	207.7 (0.1 C)/140.2 (1 C)	~85.1 (1 C,100 cycles)
P2/T-Na _{0.44} Co _{0.1} Mn _{0.9} O ₂ ^[98]	2.0–4.0	173.2 (0.1 C)/108.3 (5 C)	81.97% (5 C,100 cycles)
P2/T-Na _{0.6} Fe _{0.04} Mn _{0.96} O ₂ ^[137]	1.5–4.3	184.9 (0.2 C)/137.6 (5 C)	83.1% (5 C,300 cycles)
P2/T-Na _{0.6} Mn _{0.9} Cu _{0.1} O ₂ ^[88]	2.0–4.1	132.8 (1 C)/85 (8 C)	80% (4 C, 250 cycles)
P2/T-Na _{0.6} Mn _{0.95} Ni _{0.05} O ₂ ^[87]	2.0–4.0	146 (1 C)/82.66 (8 C)	~79.5% (1 C,50 cycles)
P2/T-Na _{0.58} Mg _{0.01} MnO ₂ ^[89]	2.0–4.0	115 (1 C)/~88 (8 C)	90.6% (1 C,100 cycles)
P2/T-Na _{0.6} Mn _{0.99} Mg _{0.01} O ₂ ^[89]	2.0–4.0	151 (1 C)/88 (8 C)	82.1% (1 C,100 cycles)
P2/T-Na _{0.6} Mn _{0.98} Zr _{0.02} O ₂ ^[151]	2.0–4.0	165.43 (0.2 C)/88 (8 C)	85.7% (1 C,100 cycles)
P2/T-Na _{0.60} Mn _{0.95} Fe _{0.05} O ₂ ^[63]	2.0–4.1	171.5 (0.1 C)/77.4 (8 C)	~71.4% (1 C,100 cycles)
P2/T-Na _{0.60} Mn _{0.95} Ti _{0.10} O ₂ ^[63]	2.0–4.1	106.6 (0.1 C)/77.4 (8 C)	87.9% (5 C,500 cycles)
P2/T-Na _{0.60} Mn _{0.80} Fe _{0.10} Ti _{0.10} O ₂ ^[63]	2.0–4.1	~105 (0.1 C)/~80 (8 C)	94.5% (1 C,100 cycles)
P2/T1/T2-Na _{2/3} Ni _{1/6} Fe _{1/6} Ti _{2/3} O ₂ ^[138]	0.15–2.5	105 (1 C)	86.5% (1 C,1500 cycles)
O3-S-Na _{0.87} Li _{0.25} Ni _{0.4} Fe _{0.2} Mn _{0.4} O _{2+δ} ^[164]	2.0–4.2	129 (12 mA g ⁻¹)/101 (120 mA g ⁻¹)	86% (100 mA g ⁻¹ ,100 cycles)
P2/S-Na _{0.5} Ni _{1/6} Co _{1/6} Mn _{2/3} O ₂ ^[165]	2.0–4.5	144 (0.5 C)/85 (10 C)	60% (0.5 C,100 cycles)
P2/P3/S-Na _{0.5} [Ni _{0.2} Co _{0.15} Mn _{0.65}]O ₂ ^[155]	1.5–4.0	180 (0.1 C)/105 (10 C)	87.6% (0.1 C,100 cycles)
P2/P3/S-Na _{0.5} Ni _{0.05} Co _{0.15} Mn _{0.65} Mg _{0.15} O ₂ ^[156]	1.5–4.3	169.4 (0.2 C)/117.1 (2 C)	65.6% (5 C,100 cycles)

Through Mg-substitution, the complicated phase transformations are suppressed in P2/P3/spinel-Na_{0.5}Ni_{0.05}Co_{0.15}Mn_{0.65}Mg_{0.15}O₂, which leads to a small volume change and lattice strain. In conclusion, the interaction between different phases, especially during the phase transformation process, is a key factor in improving electrochemical properties of composite structure materials. In single-phase materials, severe phase transitions usually occur at high-voltages, such as P2–O2 phase transition in P2-Na_{2/3}Ni_{1/3}Mn_{2/3}O₂^[166] and O3–O'3–P3–P'3–O3' phase transition in O3-NaNi_{1/2}Mn_{1/2}O₂^[167]. Phase transition leads to severe structural degradation and poor cycling performance. However, in composite oxide cathode materials, the voltage at which the phase transition occurs is different in each phase. Therefore, the phase remaining stationary can act as a pillar when another phase

undergoes phase transition, leading to reduced lattice mismatch and increased structural reversibility.

5. Summary and Prospects

In summary, we have provided a comprehensive review of the recent progress and key issues of composite oxide cathode materials for SIBs. The three issues of phase regulation, electrochemical performance and reaction mechanism have been discussed and summarized in detail. For the design and regulation of composite oxide cathode materials, elemental substitution, adjustment of the sodium content and control of the calcination temperature are effective strategies. In particular, based on the concept of cationic potential, we conclude

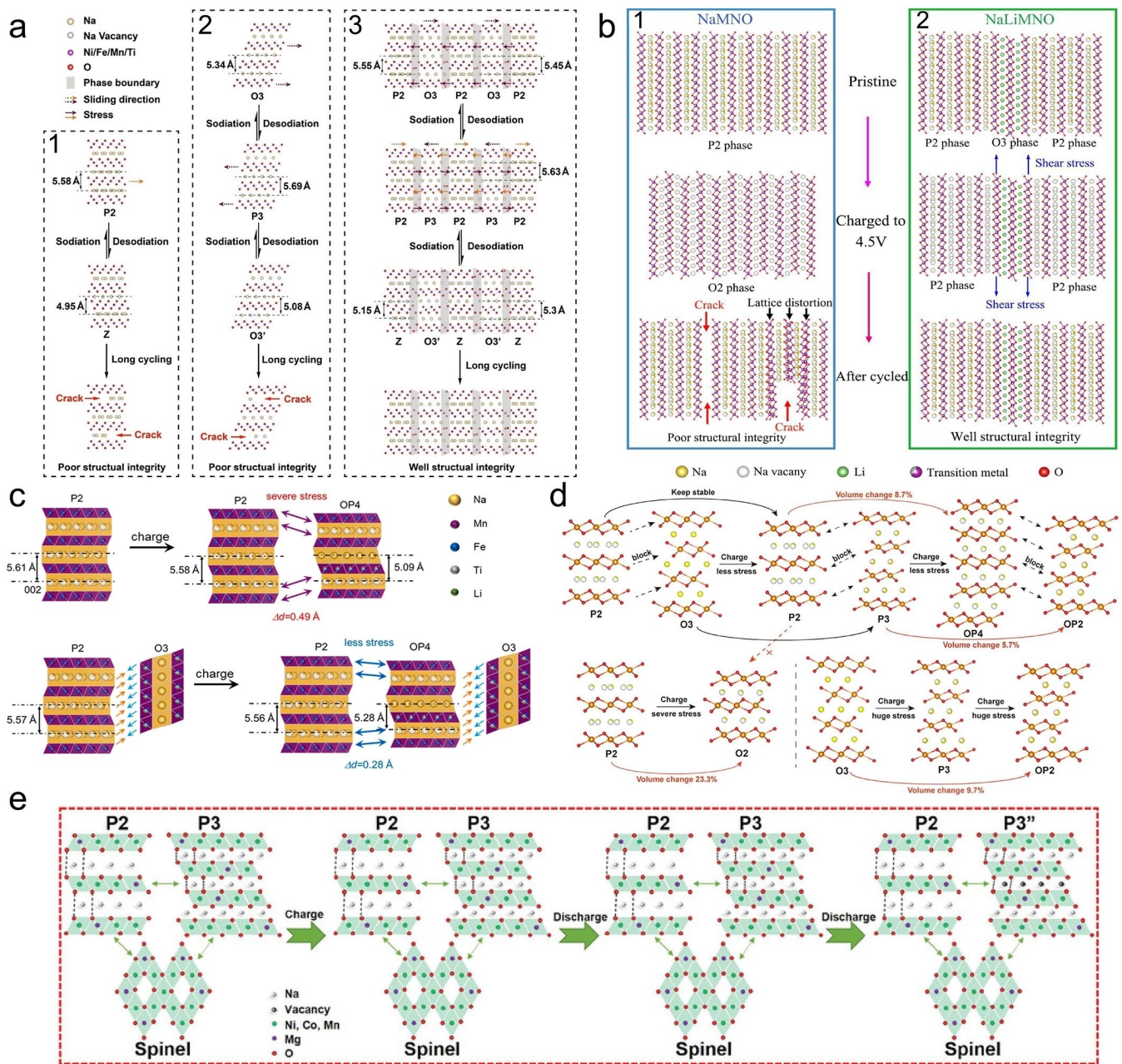


Figure 12. Schematic view of structural changes for a₁) $\text{P}_2\text{-Na}_{2/3}\text{Ni}_{1/3}\text{Mn}_{0.57}\text{Ti}_{0.1}\text{O}_2$, a₂) $\text{O}_3\text{-NaNi}_{1/3}\text{Fe}_{1/3}\text{Mn}_{1/3}\text{O}_2$ and a₃) $\text{P}_2/\text{O}_3\text{-Na}_{0.766}\text{Ni}_{0.33}\text{Mn}_{0.5}\text{Fe}_{0.1}\text{Ti}_{0.07}\text{O}_2$ during Na (de)sodiation. Reproduced with permission from Ref. [49]. Copyright (2022) Wiley-VCH. b) Schematic diagram of interfacial shear stress: Structure evolution of b₁) $\text{P}_2\text{-Na}_{0.67}\text{Mn}_{0.67}\text{Ni}_{0.33}\text{O}_2$, b₂) $\text{P}_2/\text{O}_3\text{-Na}_{0.67}\text{Li}_{0.16}\text{Mn}_{0.67}\text{Ni}_{0.33}\text{O}_{2+\delta}$. Reproduced with permission from Ref. [76]. Copyright (2021) Elsevier. c) Schematic diagram of the phase transition during charging of $\text{P}_2\text{-Na}_{0.67}\text{Fe}_{0.5}\text{Mn}_{0.5}\text{O}_2$ and $\text{P}_2/\text{O}_3\text{-Na}_{0.67}\text{Li}_{0.11}\text{Fe}_{0.36}\text{Mn}_{0.36}\text{Ti}_{0.17}\text{O}_2$. Reproduced with permission from Ref. [60]. Copyright (2021) Elsevier. d) Schematic of the structure changes of $\text{P}_2\text{-Na}_{0.85}\text{Ni}_{0.34}\text{Mn}_{0.66}\text{O}_2$, $\text{P}_2/\text{O}_3\text{-Na}_{0.85}\text{Ni}_{0.34}\text{Mn}_{0.33}\text{Ti}_{0.33}\text{O}_2$ and $\text{O}_3\text{-Na}_{0.85}\text{Ni}_{0.34}\text{Mn}_{0.22}\text{Ti}_{0.44}\text{O}_2$ during the charging. Reproduced with permission from Ref. [58]. Copyright (2022) Elsevier. e) Schematic diagram showing the evolution of crystal structure of $\text{P}_2/\text{P}_3/\text{spinel-Na}_{0.5}\text{Ni}_{0.05}\text{Co}_{0.15}\text{Mn}_{0.65}\text{Mg}_{0.15}\text{O}_2$ during the cycling. Reproduced with permission from Ref. [156]. Copyright (2022) Wiley-VCH.

that materials with small d (cation potential close to the dividing line) tend to form P2/O3 composite structure. The comparison and generalization of electrochemical performance reveals that the composite oxide cathode materials tend to show better electrochemical properties than mixing materials and single-phase materials, especially in cycling performance and rate performance. Furthermore, by summarizing the interaction mechanisms, we believe that the interaction between different phases in composite oxide cathode materials

is a key factor in improving electrochemical properties. This interaction is particularly evident in the phase transitions process, which suppresses lattice mismatch and improves structural stability.

Due to the good electrochemical properties, the research of composite oxide cathode materials is of great importance. However, during the synthesis of the material, current research has not yet fully clarified the effect of factors such as the synthesis method (solid-state reaction, sol-gel and co-precip-

itation), calcination temperature and cooling method on the crystal structure. Besides, in terms of reaction mechanism, the relationship between the interaction between different phases and the enhanced electrochemical properties needs to be further investigated. We believe that an in-depth study of these scientific issues could contribute to the design and performance enhancement of composite oxide cathode materials.

The commercialization of sodium ion batteries has accelerated in recent years. Due to the excellent electrochemical properties, we believe composite oxide cathode materials can be used for practical applications of sodium ion batteries. For cathode materials, the leap from half-cell to full cell is a key step towards commercialization. Some composite oxide cathode materials also show excellent performance in full batteries.^[49,58,68] Moreover, the anode (e.g., hard carbon) of SIBs full cells in practical application often irreversibly consume part of sodium ions from the cathode materials. One characteristic of P₂O₃ composite structure materials is its relatively high sodium content (0.75–0.85),^[49,58,64,105–109] making them more suitable for full cells, which provides an effective solution to this problem. However, as previously stated, the synthesis method can have an important impact on the crystal structure. In addition, the synthesis conditions in the laboratory are very different from those of large-scale production, resulting in the synthesis of composite oxide cathode materials for industrialization still facing significant challenges. Although there are still many difficulties to overcome, we believe the composite oxide cathode materials will be one of the most competitive and attractive cathodes for commercial sodium ion batteries.

Acknowledgements

This work was supported by the National Natural Science Foundation of China (Grant No. 52102302), the Young Talent Support Plan of Xi'an Jiaotong University (Grant No. DQ6J011), and State Key Laboratory of Electrical Insulation and Power Equipment (EPE23313). P.-F.W. also thanks the support from the "High-Level Talent Introduction Plan" of Shaanxi Province and the Siyuan Scholar of Xi'an Jiaotong University.

Conflict of Interest

The authors declare no conflict of interest.

Data Availability Statement

Data sharing is not applicable to this article as no new data were created or analyzed in this study.

Keywords: composite phase · oxide cathodes · reaction mechanism · sodium-ion batteries · structure regulation

- [1] J. Y. Hwang, S. T. Myung, Y. K. Sun, *Chem. Soc. Rev.* **2017**, *46*, 3529–3614.
- [2] R. Berthelot, D. Carlier, C. Delmas, *Nat. Mater.* **2011**, *10*, 74–80.
- [3] B. Dunn, H. Kamath, J.-M. Tarascon, *Science* **2011**, *334*, 6058.
- [4] H. Su, S. Jaffer, H. Yu, *Energy Storage Mater.* **2016**, *5*, 116–131.
- [5] M. Armand, J.-M. Tarascon, *Nature* **2008**, *451*, 652–657.
- [6] Y. K. Sun, Z. Chen, H. J. Noh, D. J. Lee, H. G. Jung, Y. Ren, S. Wang, C. S. Yoon, S. T. Myung, K. Amine, *Nat. Mater.* **2012**, *11*, 942–947.
- [7] Y. X. Yin, S. Xin, Y. G. Guo, L. J. Wan, *Angew. Chem. Int. Ed.* **2013**, *52*, 13186–13200; *Angew. Chem.* **2013**, *125*, 13426–13441.
- [8] R. Usiskin, Y. Lu, J. Popovic, M. Law, P. Balaya, Y.-S. Hu, J. Maier, *Nat. Rev. Mater.* **2021**, *6*, 1020–1035.
- [9] E. de la Llave, V. Borgel, K. J. Park, J. Y. Hwang, Y. K. Sun, P. Hartmann, F. F. Chesneau, D. Aurbach, *ACS Appl. Mater. Interfaces* **2016**, *8*, 1867–1875.
- [10] M. D. Slater, D. Kim, E. Lee, C. S. Johnson, *Adv. Funct. Mater.* **2013**, *23*, 947–958.
- [11] J. M. Tarascon, *Nat. Chem.* **2010**, *2*, 510.
- [12] N. Yabuuchi, K. Kubota, M. Dahbi, S. Komaba, *Chem. Rev.* **2014**, *114*, 11636–11682.
- [13] T. Wang, X. Yu, M. Fan, Q. Meng, Y. Xiao, Y. X. Yin, H. Li, Y. G. Guo, *Chem. Commun.* **2019**, *56*, 245–248.
- [14] S.-W. Kim, D.-H. Seo, X. Ma, G. Ceder, K. Kang, *Adv. Energy Mater.* **2012**, *2*, 710–721.
- [15] N. Ortiz-Vitoriano, N. E. Drewett, E. Gonzalo, T. Rojo, *Energy Environ. Sci.* **2017**, *10*, 1051–1074.
- [16] Y. Kim, K. H. Ha, S. M. Oh, K. T. Lee, *Chem. Eur. J.* **2014**, *20*, 11980–11992.
- [17] M. Chen, W. Hua, J. Xiao, D. Cortie, W. Chen, E. Wang, Z. Hu, Q. Gu, X. Wang, S. Idris, S. L. Chou, S. X. Dou, *Nat. Commun.* **2019**, *10*, 1480.
- [18] C. Zhu, C. Wu, C.-C. Chen, P. Kopold, P. A. van Aken, J. Maier, Y. Yu, *Chem. Mater.* **2017**, *29*, 5207–5215.
- [19] W. Zhou, L. Xue, X. Lu, H. Gao, Y. Li, S. Xin, G. Fu, Z. Cui, Y. Zhu, J. B. Goodenough, *Nano Lett.* **2016**, *16*, 7836–7841.
- [20] J. Kim, G. Yoon, H. Kim, Y.-U. Park, K. Kang, *Chem. Mater.* **2018**, *30*, 3683–3689.
- [21] Y. You, X.-L. Wu, Y.-X. Yin, Y.-G. Guo, *Energy Environ. Sci.* **2014**, *7*, 1643–1647.
- [22] L. Wang, J. Song, R. Qiao, L. A. Wray, M. A. Hossain, Y.-D. Chuang, W. Yang, Y. Lu, D. Evans, J.-J. Lee, S. Vail, X. Zhao, M. Nishijima, S. Kakimoto, J. B. Goodenough, *J. Am. Chem. Soc.* **2015**, *137*, 2548–2554.
- [23] H.-W. Lee, R. Y. Wang, M. Pasta, S. Woo Lee, N. Liu, Y. Cui, *Nat. Commun.* **2014**, *5*, 5280.
- [24] H. Zhang, Y. Gao, X. H. Liu, Z. Yang, X. X. He, L. Li, Y. Qiao, W. H. Chen, R. H. Zeng, Y. Wang, S. L. Chou, *Adv. Funct. Mater.* **2021**, *32*, 2107718.
- [25] Y. Wang, Y. Ding, L. Pan, Y. Shi, Z. Yue, Y. Shi, G. Yu, *Nano Lett.* **2016**, *16*, 3329–3334.
- [26] M. Lee, J. Hong, J. Lopez, Y. Sun, D. Feng, K. Lim, W. C. Chueh, M. F. Toney, Y. Cui, Z. Bao, *Nat. Energy* **2017**, *2*, 861–868.
- [27] R.-M. Gao, Z.-J. Zheng, P.-F. Wang, C.-Y. Wang, H. Ye, F.-F. Cao, *Energy Storage Mater.* **2020**, *30*, 9–26.
- [28] F. Agusse, J.-M. Lopez del Amo, L. Otaegui, E. Goikolea, T. Rojo, G. Singh, *J. Power Sources* **2016**, *336*, 186–195.
- [29] C. Wang, G. M. Zhang, W. L. Qu, H. F. Wang, S. Zhang, C. Deng, *J. Mater. Chem. A* **2018**, *7*, 1797–1809.
- [30] M. H. Han, E. Gonzalo, G. Singh, T. Rojo, *Energy Environ. Sci.* **2015**, *8*, 81–102.
- [31] S. Guo, J. Yi, Y. Sun, H. Zhou, *Energy Environ. Sci.* **2016**, *9*, 2978–3006.
- [32] L. Zheng, J. Li, M. N. Obrovac, *Chem. Mater.* **2017**, *29*, 1623–1631.
- [33] Z. Yang, W. Xiang, Z. Wu, F. He, J. Zhang, Y. Xiao, B. Zhong, X. Guo, *Ceram. Int.* **2017**, *43*, 3866–3872.
- [34] S. Komaba, C. Takei, T. Nakayama, A. Ogata, N. Yabuuchi, *Electrochim. Commun.* **2010**, *12*, 355–358.
- [35] C.-L. Xu, W. Xiang, Z.-G. Wu, Y.-D. Xu, Y.-C. Li, H.-T. Li, Y. Xiao, B.-C. Tan, X.-D. Guo, B.-H. Zhong, *J. Alloys Compd.* **2019**, *777*, 434–442.
- [36] C.-Y. Yu, J.-S. Park, H.-G. Jung, K.-Y. Chung, D. Aurbach, Y.-K. Sun, S.-T. Myung, *Energy Environ. Sci.* **2015**, *8*, 2019–2026.
- [37] M. Guignard, C. Didier, J. Darriet, P. Bordet, E. Elkaim, C. Delmas, *Nat. Mater.* **2013**, *12*, 74–80.
- [38] C. F. C. Delmas, P. Hagenmuller, *Physica B + C* **1980**, *99*, 81–85.
- [39] P.-F. Wang, Y. You, Y.-X. Yin, Y.-G. Guo, *Adv. Energy Mater.* **2018**, *8*, 1701912.
- [40] P. Vassilaras, X. Ma, X. Li, G. Ceder, *J. Electrochem. Soc.* **2012**, *160*, A207–A211.

- [41] M. Ren, H. Fang, C. Wang, H. Li, F. Li, *Energy Fuels* **2020**, *34*, 13412–13426.
- [42] M. M. Doeff, M. Y. Peng, Y. Ma, L. C. D. Jonghe, *J. Electrochem. Soc.* **1994**, *141*, L145.
- [43] Y. Liu, C. Wang, S. Zhao, L. Zhang, K. Zhang, F. Li, J. Chen, *Chem. Sci.* **2021**, *12*, 1062–1067.
- [44] C. Wang, L. Liu, S. Zhao, Y. Liu, Y. Yang, H. Yu, S. Lee, G.-H. Lee, Y.-M. Kang, R. Liu, F. Li, J. Chen, *Nat. Commun.* **2021**, *12*, 2256.
- [45] Q. Liu, Z. Hu, M. Chen, C. Zou, H. Jin, S. Wang, S. L. Chou, Y. Liu, S. X. Dou, *Adv. Funct. Mater.* **2020**, *30*, 1909530.
- [46] Y. X. Chang, L. Yu, X. Xing, Y. J. Guo, Z. Y. Xie, S. Xu, *Chem. Rec.* **2022**, *22*, e202200122.
- [47] Q. Liu, Z. Hu, M. Chen, C. Zou, H. Jin, S. Wang, S. L. Chou, S. X. Dou, *Small* **2019**, *15*, e1805381.
- [48] K. Kubota, S. Kumakura, Y. Yoda, K. Kuroki, S. Komaba, *Adv. Energy Mater.* **2018**, *8*, 1703415.
- [49] Z. Cheng, X.-Y. Fan, L. Yu, W. Hua, Y.-J. Guo, Y.-H. Feng, F.-D. Ji, M. Liu, Y.-X. Yin, X. Han, Y.-G. Guo, P.-F. Wang, *Angew. Chem. Int. Ed.* **2022**, *61*, e202117728.
- [50] J. Kim, J. Kwon, M. Kim, J. Do, D. Lee, H. Han, *Polym. J.* **2016**, *48*, 829–834.
- [51] L. Yu, H. Dong, Y.-X. Chang, Z. Cheng, K. Xu, Y.-H. Feng, D. Si, X. Zhu, M. Liu, B. Xiao, P.-F. Wang, S. Xu, *Sci. China Chem.* **2022**, *65*, 2005–2014.
- [52] H. Kim, D. J. Kim, D.-H. Seo, M. S. Yeom, K. Kang, D. K. Kim, Y. Jung, *Chem. Mater.* **2012**, *24*, 1205–1211.
- [53] Y. Cao, L. Xiao, W. Wang, D. Choi, Z. Nie, J. Yu, L. V. Saraf, Z. Yang, J. Liu, *Adv. Mater.* **2011**, *23*, 3155–3160.
- [54] J. F. Whitacre, A. Tevar, S. Sharma, *Electrochem. Commun.* **2010**, *12*, 463–466.
- [55] E. Hosono, T. Saito, J. Hoshino, M. Okubo, Y. Saito, D. Nishio-Hamane, T. Kudo, H. Zhou, *J. Power Sources* **2012**, *217*, 43–46.
- [56] R. Li, Y. Liu, Z. Wang, J. Li, *Electrochim. Acta* **2019**, *318*, 14–22.
- [57] X. Rong, F. Gao, F. Ding, Y. Lu, K. Yang, H. Li, X. Huang, L. Chen, Y.-S. Hu, *J. Mater. Sci. Technol.* **2019**, *35*, 1250–1254.
- [58] L. Yu, Z. Cheng, K. Xu, Y.-X. Chang, Y.-H. Feng, D. Si, M. Liu, P.-F. Wang, S. Xu, *Energy Storage Mater.* **2022**, *50*, 730–739.
- [59] D. Zhou, W. Huang, X. Lv, F. Zhao, *J. Power Sources* **2019**, *421*, 147–155.
- [60] C. Chen, W. Huang, Y. Li, M. Zhang, K. Nie, J. Wang, W. Zhao, R. Qi, C. Zuo, Z. Li, H. Yi, F. Pan, *Nano Energy* **2021**, *90*, 106504.
- [61] D. Wang, H. Chen, X. Zheng, L. Qiu, J. Qu, Z. Wu, Y. Zhong, W. Xiang, B. Zhong, X. Guo, *ChemElectroChem* **2019**, *6*, 5155–5161.
- [62] J. Li, T. Risthaus, J. Wang, D. Zhou, X. He, N. Ehteshami, V. Murzin, A. Friesen, H. Liu, X. Hou, M. Diehl, E. Paillard, M. Winter, J. Li, *J. Power Sources* **2019**, *449*, 227554.
- [63] D. Wang, C. Shi, Y.-P. Deng, Z. Wu, Z. Yang, Y. Zhong, Y. Jiang, B. Zhong, L. Huang, X. Guo, Z. Chen, *Nano Energy* **2020**, *70*, 104539.
- [64] B. Xiao, X. Liu, M. Song, X. Yang, F. Omenya, S. Feng, V. Sprenkle, K. Amine, G. Xu, X. Li, D. Reed, *Nano Energy* **2021**, *89*, 106371.
- [65] Y. Liu, X. Fang, A. Zhang, C. Shen, Q. Liu, H. A. Enaya, C. Zhou, *Nano Energy* **2016**, *27*, 27–34.
- [66] Y. Huang, Z. Yan, W. Luo, Z. Hu, G. Liu, L. Zhang, X. Yang, M. Ou, W. Liu, L. Huang, H. Lin, C.-T. Chen, J. Luo, S. Li, J. Han, S. Chou, Y. Huang, *Energy Storage Mater.* **2020**, *29*, 182–189.
- [67] P.-F. Wang, H. Xin, T.-T. Zuo, Q. Li, X. Yang, Y.-X. Yin, X. Gao, X. Yu, Y.-G. Guo, *Angew. Chem. Int. Ed.* **2018**, *57*, 8178–8183; *Angew. Chem.* **2018**, *130*, 8310–8315.
- [68] Y. Xiao, H.-R. Wang, H.-Y. Hu, Y.-F. Zhu, S. Li, J.-Y. Li, X.-W. Wu, S.-L. Chou, *Adv. Mater.* **2022**, *34*, 2202695.
- [69] Y. Liang, H. Xu, K. Jiang, J. Bian, S. Guo, H. Zhou, *Chem. Commun.* **2021**, *57*, 2891–2894.
- [70] E. Lee, J. Lu, Y. Ren, X. Luo, X. Zhang, J. Wen, D. Miller, A. DeWahl, S. Hackney, B. Key, D. Kim, M. D. Slater, C. S. Johnson, *Adv. Energy Mater.* **2014**, *4*, 1400458.
- [71] S. Guo, P. Liu, H. Yu, Y. Zhu, M. Chen, M. Ishida, H. Zhou, *Angew. Chem. Int. Ed.* **2015**, *54*, 5894–5899; *Angew. Chem.* **2015**, *127*, 5992–5997.
- [72] M. Bianchini, E. Gonzalo, N. E. Drewett, N. Ortiz-Vitoriano, J. M. L. d. Amo, F. J. Bonilla, B. Acebedo, T. Rojo, *J. Mater. Chem. A* **2018**, *6*, 3552–3559.
- [73] Q. Huang, P. He, L. Xiao, Y. Feng, J. Liu, Y. Yang, B. Huang, X. Cui, P. Wang, W. Wei, *ACS Appl. Mater. Interfaces* **2020**, *12*, 2191–2198.
- [74] J. H. Stansby, M. Avdeev, H. E. A. Brand, E. Gonzalo, N. E. Drewett, N. Ortiz-Vitoriano, N. Sharma, T. Rojo, *Dalton Trans.* **2021**, *50*, 1357–1365.
- [75] J. Feng, S.-h. Luo, J. Cong, K. Li, S. Yan, Q. Wang, Y. Zhang, X. Liu, X. Lei, P.-q. Hou, *J. Electroanal. Chem.* **2022**, *916*, 116378.
- [76] Q. Huang, M. Wang, L. Zhang, S. Qi, Y. Feng, P. He, X. Ji, P. Wang, L. Zhou, S. Chen, W. Wei, *Energy Storage Mater.* **2022**, *45*, 389–398.
- [77] B. Hu, F. Geng, C. Zhao, B. Doumerc, J. Trebosc, O. Lafon, C. Li, M. Shen, B. Hu, *ACS Appl. Mater. Interfaces* **2020**, *12*, 41485–41494.
- [78] Q. Huang, J. Liu, L. Zhang, S. Xu, L. Chen, P. Wang, D. G. Ivey, W. Wei, *Nano Energy* **2018**, *44*, 336–344.
- [79] D. Buchholz, L. G. Chagas, C. Vaalma, L. Wu, S. Passerini, *J. Mater. Chem. A* **2014**, *2*, 13415–13421.
- [80] J. Cabana, N. A. Chernova, J. Xiao, M. Roppolo, K. A. Aldi, M. S. Whittingham, C. P. Grey, *Inorg. Chem.* **2013**, *52*, 8540–8550.
- [81] L. G. Chagas, D. Buchholz, C. Vaalma, L. Wu, S. Passerini, *J. Mater. Chem. A* **2014**, *2*, 20263–20270.
- [82] Z. Yan, L. Tang, Y. Huang, W. Hua, Y. Wang, R. Liu, Q. Gu, S. Indris, S. L. Chou, Y. Huang, M. Wu, S. X. Dou, *Angew. Chem. Int. Ed.* **2019**, *58*, 1412–1416; *Angew. Chem.* **2019**, *131*, 1426–1430.
- [83] N. Jiang, Q. Liu, J. Wang, W. Yang, W. Ma, L. Zhang, Z. Peng, Z. Zhang, *Small* **2021**, *17*, e2007103.
- [84] M. M. Rahman, J. Mao, W. H. Kan, C.-J. Sun, L. Li, Y. Zhang, M. Avdeev, X.-W. Du, F. Lin, *ACS Materials Lett.* **2019**, *1*, 573–581.
- [85] S. Bao, S.-h. Luo, Z.-y. Wang, S.-x. Yan, Q. Wang, J.-y. Li, *J. Power Sources* **2018**, *396*, 404–411.
- [86] W. Ma, K. Yin, H. Gao, J. Niu, Z. Peng, Z. Zhang, *Nano Energy* **2018**, *54*, 349–359.
- [87] H. Chen, Z. Wu, Z. Zheng, T. Chen, X. Guo, J. Li, B. Zhong, *Electrochim. Acta* **2018**, *273*, 63–70.
- [88] T. R. Chen, T. Sheng, Z. G. Wu, J. T. Li, E. H. Wang, C. J. Wu, H. T. Li, X. D. Guo, B. H. Zhong, L. Huang, S. G. Sun, *ACS Appl. Mater. Interfaces* **2018**, *10*, 10147–10156.
- [89] J. Qu, D. Wang, Z. G. Yang, Z. G. Wu, L. Qiu, X. D. Guo, J. T. Li, B. H. Zhong, X. C. Chen, S. X. Dou, *ACS Appl. Mater. Interfaces* **2019**, *11*, 26938–26945.
- [90] M. S. Chae, H. J. Kim, J. Lyoo, R. Attias, Y. Gofer, S.-T. Hong, D. Aurbach, *Adv. Energy Mater.* **2020**, *10*, 2002205.
- [91] G. Gao, D. Tie, H. Ma, H. Yu, S. Shi, B. Wang, S. Xu, L. Wang, Y. Zha, *J. Mater. Chem. A* **2018**, *6*, 6675–6684.
- [92] T. Jin, P.-F. Wang, Q.-C. Wang, K. Zhu, T. Deng, J. Zhang, W. Zhang, X.-Q. Yang, L. Jiao, C. Wang, *Angew. Chem. Int. Ed.* **2020**, *59*, 14511–14516; *Angew. Chem.* **2020**, *132*, 14619–14624.
- [93] Y.-K. Sun, *ACS Energy Lett.* **2020**, *5*, 1278–1280.
- [94] C. Delmas, D. Carlier, M. Guignard, *Adv. Energy Mater.* **2021**, *11*, 2001201.
- [95] T.-R. Chen, Z.-G. Wu, W. Xiang, E.-H. Wang, C.-J. Wu, M.-Z. Chen, X.-D. Guo, B.-H. Zhong, *Ceram. Int.* **2017**, *43*, 6303–6311.
- [96] Y. Xiao, P.-F. Wang, Y.-X. Yin, Y.-F. Zhu, X. Yang, X.-D. Zhang, Y. Wang, X.-D. Guo, B.-H. Zhong, Y.-G. Guo, *Adv. Energy Mater.* **2018**, *8*, 1800492.
- [97] Y.-T. Zhou, X. Sun, B.-K. Zou, J.-Y. Liao, Z.-Y. Wen, C.-H. Chen, *Electrochim. Acta* **2016**, *213*, 496–503.
- [98] Y. Xiao, Y.-F. Zhu, W. Xiang, Z.-G. Wu, Y.-C. Li, J. Lai, S. Li, E.-H. Wang, Z.-G. Yang, C.-L. Xu, B.-H. Zhong, X. Guo, *Angew. Chem. Int. Ed.* **2019**, *59*, 1491–1495.
- [99] W.-J. Shi, Y.-W. Yan, C. Chi, X.-T. Ma, D. Zhang, S.-D. Xu, L. Chen, X.-M. Wang, S.-B. Liu, *J. Power Sources* **2019**, *427*, 129–137.
- [100] M. Bianchini, J. Wang, R. J. Clement, B. Ouyang, P. Xiao, D. Kitchev, T. Shi, Y. Zhang, Y. Wang, H. Kim, M. Zhang, J. Bai, F. Wang, W. Sun, G. Ceder, *Nat. Mater.* **2020**, *19*, 1088–1095.
- [101] Y.-N. Zhou, P.-F. Wang, Y.-B. Niu, Q. Li, X. Yu, Y.-X. Yin, S. Xu, Y.-G. Guo, *Nano Energy* **2019**, *55*, 143–150.
- [102] C. Zhao, Q. Wang, Z. Yao, J. Wang, B. Sánchez-Lengeling, F. Ding, X. Qi, Y. Lu, X. Bai, B. Li, H. Li, A. Aspuru-Guzik, X. Huang, C. Delmas, M. Wagemaker, L. Chen, Y.-S. Hu, *Science* **2020**, *370*, 708–711.
- [103] X. Gao, H. Liu, H. Chen, Y. Mei, B. Wang, L. Fang, M. Chen, J. Chen, J. Gao, L. Ni, L. Yang, Y. Tian, W. Deng, R. Momen, W. Wei, L. Chen, G. Zou, H. Hou, Y.-M. Kang, X. Ji, *Sci. Bull.* **2022**, *67*, 1589–1602.
- [104] I. Hasa, D. Buchholz, S. Passerini, J. Hassoun, *ACS Appl. Mater. Interfaces* **2015**, *7*, 5206–5212.
- [105] A. K. Paidi, W. B. Park, P. Ramakrishnan, S.-H. Lee, J.-W. Lee, K.-S. Lee, H. Ahn, T. Liu, J. Gim, M. Avdeev, M. Pyo, J. I. Sohn, K. Amine, K.-S. Sohn, T. J. Shin, D. Ahn, J. Lu, *Adv. Mater.* **2022**, *34*, 2202137.
- [106] J. Chen, L. Li, L. Wu, Q. Yao, H. Yang, Z. Liu, L. Xia, Z. Chen, J. Duan, S. Zhong, *J. Power Sources* **2018**, *406*, 110–117.
- [107] K. Wang, Z.-G. Wu, G. Melinte, Z.-G. Yang, A. Sarkar, W. Hua, X. Mu, Z.-W. Yin, J.-T. Li, X.-D. Guo, B.-H. Zhong, C. Kübel, *J. Mater. Chem. A* **2021**, *9*, 13151–13160.

- [108] X. Qi, L. Liu, N. Song, F. Gao, K. Yang, Y. Lu, H. Yang, Y. S. Hu, Z. H. Cheng, L. Chen, *ACS Appl. Mater. Interfaces* **2017**, *9*, 40215–40223.
- [109] L. Yang, J. M. L. Amo, Z. Shadike, S. M. Bak, F. Bonilla, M. Galceran, P. K. Nayak, J. R. Buchheim, X. Q. Yang, T. Rojo, P. Adelhelm, *Adv. Funct. Mater.* **2020**, *30*, 2003364.
- [110] D. H. Lee, J. Xu, Y. S. Meng, *Phys. Chem. Chem. Phys.* **2013**, *15*, 3304.
- [111] P.-F. Wang, H.-R. Yao, X.-Y. Liu, Y.-X. Yin, J.-N. Zhang, Y. Wen, X. Yu, L. Gu, Y.-G. Guo, *Sci. Adv.* **2018**, *4*, eaar6018.
- [112] L. Yang, C. Chen, S. Xiong, C. Zheng, P. Liu, Y. Ma, W. Xu, Y. Tang, S. P. Ong, H. Chen, *JACS Au* **2020**, *1*, 98–107.
- [113] X. Rong, E. Hu, Y. Lu, F. Meng, C. Zhao, X. Wang, Q. Zhang, X. Yu, L. Gu, Y.-S. Hu, H. Li, X. Huang, X.-Q. Yang, C. Delmas, L. Chen, *Joule* **2019**, *3*, 503–517.
- [114] N. Yabuuchi, R. Hara, K. Kubota, J. Paulsen, S. Kumakura, S. Komaba, *J. Mater. Chem. A* **2014**, *2*, 16851–16855.
- [115] Z. Cheng, B. Zhao, Y.-J. Guo, L. Yu, B. Yuan, W. Hua, Y.-X. Yin, S. Xu, B. Xiao, X. Han, P.-F. Wang, Y.-G. Guo, *Adv. Energy Mater.* **2022**, *12*, 2103461.
- [116] D. Kim, E. Lee, M. Slater, W. Lu, S. Rood, C. S. Johnson, *Electrochem. Commun.* **2012**, *18*, 66–69.
- [117] L. Mu, S. Xu, Y. Li, Y.-S. Hu, H. Li, L. Chen, X. Huang, *Adv. Mater.* **2015**, *27*, 6928–6933.
- [118] A. Varela, M. Parras, J. M. González-Calbet, *Eur. J. Inorg. Chem.* **2005**, *2005*, 4410–4416.
- [119] S. Komaba, N. Yabuuchi, T. Nakayama, A. Ogata, T. Ishikawa, I. Nakai, *Inorg. Chem.* **2012**, *51*, 6211–6220.
- [120] C.-C. Lin, H.-Y. Liu, J.-W. Kang, C.-C. Yang, C.-H. Li, H.-Y. T. Chen, S.-C. Huang, C.-S. Ni, Y.-C. Chuang, B.-H. Chen, C.-K. Chang, H.-Y. Chen, *Energy Storage Mater.* **2022**, *51*, 159–171.
- [121] R. Li, J. Gao, J. Li, H. Huang, X. Li, W. Wang, L.-R. Zheng, S.-M. Hao, J. Qiu, W. Zhou, *Adv. Funct. Mater.* **2022**, *32*, 2205661.
- [122] J. E. Wang, H. Kim, Y. H. Jung, D. K. Kim, D. J. Kim, *Small* **2021**, *17*, 2100146.
- [123] G. K. Veerasubramani, Y. Subramanian, M.-S. Park, B. Senthilkumar, A. Eftekhari, S. J. Kim, D.-W. Kim, *Electrochim. Acta* **2019**, *296*, 1027–1034.
- [124] Y.-F. Zhu, Y. Xiao, S.-X. Dou, S.-L. Chou, *Cell Rep. Phys. Sci.* **2021**, *2*, 100631.
- [125] M. H. Han, B. Acebedo, E. Gonzalo, P. S. Fontecoba, S. Clarke, D. Saurel, T. Rojo, *Electrochim. Acta* **2015**, *182*, 1029–1036.
- [126] N. Yabuuchi, M. Kajiyama, J. Iwatate, H. Nishikawa, S. Hitomi, R. Okuyama, R. Usui, Y. Yamada, S. Komaba, *Nat. Mater.* **2012**, *11*, 512–517.
- [127] S. Kalluri, K. H. Seng, W. K. Pang, Z. Guo, Z. Chen, H.-K. Liu, S. X. Dou, *ACS Appl. Mater. Interfaces* **2014**, *6*, 8953–8958.
- [128] S.-Y. Zhang, Y.-J. Guo, Y.-N. Zhou, X.-D. Zhang, Y.-B. Niu, E.-H. Wang, L.-B. Huang, P.-F. An, J. Zhang, X.-A. Yang, Y.-X. Yin, S. Xu, Y.-G. Guo, *Small* **2021**, *17*, 2007236.
- [129] M. Keller, D. Buchholz, S. Passerini, *Adv. Energy Mater.* **2016**, *6*, 1501555.
- [130] Q. Huang, J. Liu, S. Xu, P. Wang, D. G. Ivey, B. Huang, W. Wei, *Chem. Mater.* **2018**, *30*, 4728–4737.
- [131] C. Chen, B. Han, G. Lin, Q. Huang, S. Zhao, D. Zhang, C. Ma, D. G. Ivey, W. Wei, *ACS Appl. Mater. Interfaces* **2018**, *10*, 28719–28725.
- [132] Y. Lei, X. Li, L. Liu, G. Ceder, *Chem. Mater.* **2014**, *26*, 5288–5296.
- [133] L. G. Chagas, D. Buchholz, L. Wu, B. Vortmann, S. Passerini, *J. Power Sources* **2014**, *247*, 377–383.
- [134] X. Chen, X. Zhou, M. Hu, J. Liang, D. Wu, J. Wei, Z. Zhou, *J. Mater. Chem. A* **2015**, *3*, 20708–20714.
- [135] A. van Bommel, J. R. Dahn, *Electrochim. Solid-State Lett.* **2010**, *13*, A62.
- [136] N. Yabuuchi, K. Kubota, Y. Aoki, S. Komaba, *J. Phys. Chem. C* **2016**, *120*, 875–885.
- [137] Z. Sun, B. Peng, L. Zhao, J. Li, L. Shi, G. Zhang, *Energy Storage Mater.* **2021**, *40*, 320–328.
- [138] H. Ma, H. Su, K. Amine, X. Liu, H. Yu, *Nano Energy* **2018**, *43*, 1–10.
- [139] M. M. Rahman, Y. Xu, H. Cheng, Q. Shi, R. Kou, L. Mu, Q. Liu, S. Xia, X. Xiao, C.-J. Sun, D. Sokaras, D. Nordlund, J.-C. Zheng, F. L. Y. Liu *Energy Environ. Sci.* **2018**, *11*, 2496–2508.
- [140] M. Keller, T. Eisenmann, D. Meira, G. Aquilanti, D. Buchholz, D. Bresser, S. Passerini, *Small Methods* **2019**, *3*, 1900239.
- [141] S. Birgisson, T. L. Christiansen, B. B. Iversen, *Chem. Mater.* **2018**, *30*, 6636–6645.
- [142] N. Sabi, A. Sarapulova, S. Idris, S. Dsoke, V. Trouillet, L. Mereacre, H. Ehrenberg, I. Saadoun, *J. Power Sources* **2021**, *481*, 229120.
- [143] F. Sauvage, L. Laffont, J.-M. Tarascon, E. Baudrin, *Inorg. Chem.* **2007**, *46*, 3289.
- [144] Z. G. Wu, J. T. Li, Y. J. Zhong, X. D. Guo, L. Huang, B. H. Zhong, D. A. Agyeman, J. M. Lim, D. H. Kim, M. H. Cho, Y. M. Kang, *ACS Appl. Mater. Interfaces* **2017**, *9*, 21267–21275.
- [145] S. Kumakura, Y. Tahara, S. Sato, K. Kubota, S. Komaba, *Chem. Mater.* **2017**, *29*, 8958–8962.
- [146] G. Singh, N. Tapia-Ruiz, J. M. Lopez del Amo, U. Maitra, J. W. Somerville, A. R. Armstrong, J. Martinez de Ildurya, T. Rojo, P. G. Bruce, *Chem. Mater.* **2016**, *28*, 5087–5094.
- [147] K. Zhang, D. Kim, Z. Hu, M. Park, G. Noh, Y. Yang, J. Zhang, V. W. Lau, S. L. Chou, M. Cho, S. Y. Choi, Y. M. Kang, *Nat. Commun.* **2019**, *10*, 5203.
- [148] J. Billaud, G. Singh, A. R. Armstrong, E. Gonzalo, V. Roddatis, M. Armand, T. Rojo, P. G. Bruce, *Energy Environ. Sci.* **2014**, *7*, 1387–1391.
- [149] Q. C. Wang, J. K. Meng, X. Y. Yue, Q. Q. Qiu, Y. Song, X. J. Wu, Z. W. Fu, Y. Y. Xia, Z. Shadike, J. Wu, X. Q. Yang, Y. N. Zhou, *J. Am. Chem. Soc.* **2019**, *141*, 840–848.
- [150] J. W. Somerville, A. Sobkowiak, N. Tapia-Ruiz, J. Billaud, J. G. Lozano, R. A. House, L. C. Gallington, T. Ericsson, L. Häggström, M. R. Roberts, U. Maitra, P. G. Bruce, *Energy Environ. Sci.* **2019**, *12*, 2223–2232.
- [151] J. Qu, T. Sheng, Z.-g. Wu, T.-r. Chen, H. Chen, Z.-g. Yang, X.-d. Guo, J.-t. Li, B.-h. Zhong, X.-s. Dou, *J. Mater. Chem. A* **2018**, *6*, 13934–13942.
- [152] X. Liang, T.-Y. Yu, H.-H. Ryu, Y.-K. Sun, *Energy Storage Mater.* **2022**, *47*, 515–525.
- [153] Q. Huang, Y. Feng, S. Xu, L. Xiao, P. He, X. Ji, P. Wang, L. Zhou, W. Wei, *ChemElectroChem* **2020**, *7*, 4383–4389.
- [154] M. Tang, J. Yang, H. Liu, X. Chen, L. Kong, Z. Xu, J. Huang, Y. Xia, *ACS Appl. Mater. Interfaces* **2020**, *12*(41), 45997–46004.
- [155] P. Hou, J. Yin, X. Lu, J. Li, Y. Zhao, X. Xu, *Nanoscale* **2018**, *10*, 6671–6677.
- [156] H.-Y. Hu, Y.-F. Zhu, Y. Xiao, S. Li, J.-Y. Li, Z.-Q. Hao, J.-H. Zhao, S.-L. Chou, *Adv. Energy Mater.* **2022**, *12*, 2201511.
- [157] C. Chen, Z. Han, S. Chen, S. Qi, X. Lan, C. Zhang, L. Chen, P. Wang, W. Wei, *ACS Appl. Mater. Interfaces* **2020**, *12*, 7144–7152.
- [158] J. Li, H. Hu, J. Wang, Y. Xiao, *Carbon Neutralization* **2022**, *1*, 96–116.
- [159] S. Kim, X. Ma, S. P. Ong, G. Ceder, *Phys. Chem. Chem. Phys.* **2012**, *14*, 15571–15578.
- [160] O. K. Park, Y. Cho, S. Lee, H.-C. Yoo, H.-K. Song, J. Cho, *Energy Environ. Sci.* **2011**, *4*, 1621.
- [161] X. D. Zhang, J. L. Shi, J. Y. Liang, Y. X. Yin, J. N. Zhang, X. Q. Yu, Y. G. Guo, *Adv. Mater.* **2018**, *30*, e1801751.
- [162] B. Put, P. M. Vereecken, N. Labyedh, A. Sepulveda, C. Huyghebaert, I. P. Radu, A. Stesmans, *ACS Appl. Mater. Interfaces* **2015**, *7*, 22413–22420.
- [163] Y.-F. Zhu, Y. Xiao, S.-X. Dou, Y.-M. Kang, S.-L. Chou, *eScience* **2021**, *1*, 13–27.
- [164] C. Deng, P. Skinner, Y. Liu, M. Sun, W. Tong, C. Ma, M. L. Lau, R. Hunt, P. Barnes, J. Xu, H. Xiong, *Chem. Mater.* **2018**, *30*, 8145–8154.
- [165] J. Zheng, P. Yan, W. H. Kan, C. Wang, A. Manthiram, *J. Electrochem. Soc.* **2016**, *163*, A584–A591.
- [166] Z. Lu, J. R. Dahn, *J. Electrochem. Soc.* **2001**, *148*, A1225.
- [167] P.-F. Wang, H.-R. Yao, X.-Y. Liu, J.-N. Zhang, L. Gu, X.-Q. Yu, Y.-X. Yin, Y.-G. Guo, *Adv. Mater.* **2017**, *29*, 1700210.

Manuscript received: October 31, 2022

Revised manuscript received: December 7, 2022

Accepted manuscript online: December 8, 2022

Version of record online: December 20, 2022